Doklady Physics, Vol. 50, No. 7, 2005, pp. 333–336. Translated from Doklady Akademii Nauk, Vol. 403, No. 1, 2005, pp. 33–36.

PHYSICS

Theory of Motion in an Optical Radiation Field for Sublimating Spherical Aerosol Solid Particles with Inhomogeneous Thermal Conductivity

Yu. I. Yalamov and A. S. Khasanov

Presented by Academician R.F. Ganiev January 27, 2005

Received January 27, 2005

In this study, we consider a radically new problem on the photophoretic motion of large spherical aerosol solid particles suspended in a one-component gas with allowance for effects of both evaporating the substance from a particle and its inhomogeneous thermal conductivity. In the mechanics of aerodisperse systems, a particle is assumed to be large provided that its radius far exceeds the mean free path of molecules in an ambient gaseous medium. As a model describing the inhomogeneous thermal conductivity, we consider its dependence at each point of a particle on the radius vector of this point.

We suggest the following mechanism of interaction between a particle and an ambient medium. The particle is exposed to a uniform flux of electromagnetic radiation whose energy is absorbed by the particle, which leads to the appearance of thermal sources in it. On the surface of the nonuniformly heated particle, a phase transition occurs in the form of sublimation (evaporation) of the particle's substance, which is accompanied by the formation of a viscous binary mixture around the particle. The interaction between the binary system and the nonuniformly heated particle's surface results in the thermal slipping of the mixture over the surface, whereas the concentration inhomogeneity provides the diffusion slipping. Under these conditions, a momentum appears acting on the particle. By this action, the particle is driven into accelerated motion. In addition, there is the viscous-resistance force acting on the particle from the binary system. When the total force acting on the particle vanishes, it begins to move uniformly and rectilinearly with a certain constant velocity called the photophoresis rate. The goal of the present study is to find this rate and to estimate the contribution that is made to it by the evaporation effect and the inhomogeneity effect.

In a coordinate system whose origin coincides with the particle center, we consider the problem of flow around a sphere that has a constant (in the absolute value and direction) velocity $\mathbf{v}_\infty$ at infinity. As the positive direction of the z axis, we choose that of the propagation of the uniform radiation flux. Since the electromagnetic-radiation flux is uniform, it is sufficient to analyze the dependence on the two coordinates θ and r. Let $\mathbf{U}^{(is)}$ be the velocity of motion of a particle with respect to the center of gravity of the outer medium (the photophoresis rate of an inhomogeneous sublimating particle). Then, $\mathbf{v}_\infty = -\mathbf{U}^{(is)} = U\mathbf{k}$, where U is an unknown quantity. Considering the stationary motion of the binary system with respect to the particle, we arrive at the following equations of motion and the boundary conditions at infinity [1]:

$$\eta\nabla^2\mathbf{v} = \nabla p, \quad \mathrm{div}\mathbf{v} = 0, \tag{1}$$

$$v_r = U\cos\theta, \quad v_\theta = -U\sin\theta, \quad p = p_\infty \quad \text{for } r \longrightarrow \infty, \tag{2}$$

where η is the dynamic viscosity of the binary mixture, whereas $\mathbf{v}$ and p describe the velocity and pressure distributions in the mixture, respectively; and p_∞ is a constant.

We suppose that n_1 is the number of molecules of the first component (evaporating substance of the particle) and n_2 is the number of molecules of the second component (one-component gas) per unit volume of the binary mixture; c_1 and c_2 are the relative concentration of the components, respectively; and $n = n_1 + n_2$. Since $c_1 + c_2 = 1$, it is sufficient to find c_1. The function c_1 satisfies the following equation and the condition at infinity [1]:

$$\nabla^2 c_1 = 0, \quad c_1 = c_\infty \quad \text{at} \quad r \longrightarrow \infty, \tag{3}$$

where c_∞ is a constant. The quantities n_1, n_2, n, ρ, T_e, and T_i (where ρ and T_e are the density and temperature of

Moscow State Regional University, Moscow, 105005 Russia

1028-3358/05/5007-0333$26.00

the binary mixture, respectively, and T_i is the particle's temperature) can be represented in the form

$$n_1 = n_{01} + n_1', \quad n_2 = n_{02} + n_2', \quad n = n_0 + n',$$
$$\rho = \rho_0 + \rho', \quad T_e = T_{0e} + T_e', \text{ and } T_i = T_{0i} + T_i',$$

where the first terms located on the right-hand sides of these relationships are equal to the average values of the corresponding quantities, and the second terms are the deviations from them. In the boundary conditions, we will use the quantities n_{01}, n_{02}, n_0, ρ_0, T_{0e}, and T_{0i} [1].

The particle's surface is impermeable for the second component of the binary mixture [1], i.e.,

$$n_{02} v_r - D\beta_1 \frac{\partial c_2}{\partial r} = 0 \quad \text{at} \quad r = a. \tag{4}$$

Here, $\beta_1 = n_0^2 \frac{m_1}{\rho_0}$, a is the particle's radius, m_1 is the molecular mass of the evaporating particle's substance, and D is the interdiffusion coefficient for the components of the binary mixture.

The thermal and diffusion slips of the binary mixture over the particle's surface lead to the following condition for the velocity v_θ [1]:

$$v_\theta = \frac{K_{Tsl}^{(e)}}{aT_{0e}} \frac{\partial T_e}{\partial \theta} + \frac{K_{sl} D}{a} \frac{\partial c_1}{\partial \theta} \quad \text{at} \quad r = a, \tag{5}$$

where $K_{Tsl}^{(e)}$ and K_{sl} are the coefficients of the thermal and diffusion slips of the medium.

Let $q_i(r, \theta)$ be the thermal-source density inside the particle and $\kappa_i(r)$ be its variable thermal conductivity. Then, for temperature inside the inhomogeneous particle, we have the equation [2]:

$$\nabla^2 T_i = -\frac{\kappa_i'}{\kappa_i} \frac{\partial T_i}{\partial r} - \frac{q_i}{\kappa_i}. \tag{6}$$

For the temperature T_e of the medium, we have the following conditions [3]:

$$\nabla^2 T_e = 0, \quad T_e = T_{0e} \quad \text{as} \quad r \longrightarrow \infty, \quad \text{and} \quad T_e = T_i \quad \text{at} \quad r = a. \tag{7}$$

On the particle's surface, a phase transition occurs for which the following boundary conditions are valid [4]:

$$n_{01} v_r - D\beta_2 \frac{\partial c_1}{\partial r} = n_0 \alpha \nu (s_1 - c_1) \quad \text{at} \quad r = a, \tag{8}$$

$$-\kappa_e \frac{\partial T_e}{\partial r} + \kappa_i \frac{\partial T_i}{\partial r} = -Lm_1 n_0 \alpha \nu (s_1 - c_1) \text{ at } r = a, \tag{9}$$

where $\beta_2 = n_0^2 \frac{m_2}{\rho_0}$, m_2 is the mass of a molecule for the second component of the binary mixture, and α, ν, s_1, and L are the evaporation coefficient, one-fourth of the absolute thermal velocity of evaporating molecules, the saturating relative concentration for the first component of the binary mixture, and the specific heat of the phase transition for the same component, respectively ($\alpha \in [0, 1]$, $\nu = \sqrt{\frac{kT_{0e}}{2\pi m_1}}$, where k is the Boltzmann constant). For the quantity s_1 on the particle surface, we use the following linearized formula [1]:

$$s_1(T_i) = s + \delta(T_i - T_{0i}) \quad \text{at} \quad r = a, \tag{10}$$

where s and δ are the values of s_1 and $\frac{\partial s_1}{\partial T_i}$ on the particle's surface at a temperature $T_i = T_{0i}$.

We seek the functions c_1, T_e, and T_i in the form [1, 3]

$$c_1(r, \theta) = c_\infty + \sum_{n=0}^{\infty} \frac{C_n}{r^{n+1}} P_n(\cos\theta),$$

$$T_e(r, \theta) = T_{0e} + \sum_{n=0}^{\infty} \frac{A_{en}}{r^{n+1}} P_n(\cos\theta),$$

and

$$T_i(r, \theta) = \sum_{n=0}^{\infty} g_{in}(r) P_n(\cos\theta),$$

where C_n and A_{en} are the indeterminate coefficients, $g_{in}(r)$ are unknown functions, and P_n are the Legendre polynomials. We assume that the function $q_i(r, \theta)$ can be expanded into a series [3]

$$q_i(r, \theta) = \sum_{n=0}^{\infty} q_{in}(r) P_n(\cos\theta),$$

$$q_{in}(r) = \frac{2n+1}{2} \int_0^\pi q_i(r, \theta) P_n(\cos\theta) \sin\theta d\theta.$$

The function $\kappa_i(r)$ is also assumed to be represented as a series $\kappa_i(r) = \sum_{s=0}^{\infty} \kappa_{i,s} r^s$, where $\kappa_{i,s}$ are the expansion coefficients. Then, the functions $g_{in}(r)$ can also be written in terms of indeterminate coefficients [5]:

$$g_{in}(r) = B_{in} M_{1n} + A_{in} M_{2n} + M_{1n} \int_a^r M_{2n} q_{in} r^2 dr$$
$$= M_{2n} \int_a^r M_{1n} q_{in} r^2 dr,$$

where

$$A_{in} = -\int_0^a M_{1n} q_{in} r^2 dr,$$

$$M_{2n}(r) = M_{1n}(r)\int_a^r \frac{dr}{r^2 \kappa_i(r) M_{1n}^2(r)},$$

and B_{in} are the indeterminate coefficients. In the general case, the functions $M_{1n}(r)$ appearing in these formulas are constructed according to recurrence formulas. Let the coefficients b_j be determined by the formulas

$$b_0 = 2, \quad b_1 = \frac{\kappa_{i,1}}{\kappa_{i,0}}, \text{ and } b_s = \frac{s\kappa_{i,s} - \sum_{j=1}^{s-1} \kappa_{i,j} b_{s-j}}{\kappa_{i,0}} \quad \text{for} \quad s \geq 2.$$

Then, we have [5]

$$M_{1n}(r) = r^n \sum_{s=0}^{\infty} \alpha_s^{(n)} r^s,$$

where

$$\alpha_0^{(n)} = 1, \text{ and } \alpha_s^{(n)} = -\frac{\sum_{j=1}^{s} (n+s-j)\alpha_{s-j}^{(n)} b_j}{s(s+2n+1)} \quad \text{for} \quad s \geq 1.$$

In the particular cases, it is possible to derive explicit formulas for $M_{1n}(r)$. If $\kappa_i \equiv \text{const}$, then

$$M_{1n}(r) \equiv r^n \quad \text{for any} \quad n. \tag{11}$$

It is of interest to consider the case in which the thermal conductivity radically varies:

$$\kappa_i(r) = \kappa_i(0)\exp(kr), \tag{12}$$

where k is a constant.

In this case, in what follows, we need only $M_{1n}(r)$ at $n = 1$:

$$M_{11}(r) = -\frac{6}{k^3 r^2}\left(\exp(-kr) - 1 + kr - \frac{k^2 r^2}{2}\right). \tag{13}$$

The coefficients A_{en}, B_{in}, and C_n can be found from expressions (7)–(9) with allowance for condition (4).

The solution to the Stokes equation is sought in the form [3, 6]:

$$v_r(r, \theta) = \sum_{i=1}^{\infty} v_{rn}(r) P_n(\cos\theta),$$

$$v_\theta(r, \theta) = \sum_{i=1}^{\infty} v_{\theta n}(r) \frac{J_{n+1}(\cos\theta)}{\sin\theta},$$

$$p = p_\infty + \sum_{i=1}^{\infty} f_{pn}(r) P_n(\cos\theta),$$

where $J_{n+1}(\cos\theta)$ are the Gegenbauer functions, v_{nr}, $v_{\theta n}$, and f_{pn} are unknown functions written in terms of the indeterminate coefficients that can be found from the boundary conditions (see [6]). Since the forces acting on the particle are determined only by the first terms in these sums [3, 6], we restrict our consideration to the search for these terms alone. As is well known from [1], they have the form

$$v_r^{(1)}(r, \theta) = \left(\frac{A_e a^3}{r^3} + \frac{B_e a}{r} + 1\right) U\cos\theta,$$

$$v_\theta^{(1)}(r, \theta) = \left(\frac{A_e a^3}{2r^3} - \frac{B_e a}{2r} - 1\right) U\sin\theta,$$

$$p^{(1)} = B_e \frac{Ua\eta}{r^2}\cos\theta,$$

where A_e and B_e are the indeterminate coefficients that can be found from the boundary conditions (4) and (5). Since $F = -4\pi\eta U a B_e \mathbf{k}$ (see [3]), from the condition $B_e = 0$, we arrive at the formula

$$U^{(\text{is})} = -\frac{2}{3T_{0e}} \frac{2K_{Tsl}^{(e)} D n_0 + \alpha\nu a[(K_{Tsl}^{(e)} + K_{sl} D\delta T_{0e}) n_{02} + \delta T_{0e} D\beta_1]}{2(2\kappa_e + \gamma\kappa_i) D n_0 + \alpha\nu a[(2\kappa_e + \gamma\kappa_i) n_{02} + 2\delta L m_1 D n_0^2]} \times \left(\frac{1}{V}\int_V (q_i^{(\text{iv})}(r, \theta)\mathbf{r}, \mathbf{k}) dV\right)\mathbf{k}, \tag{14}$$

where V is the volume of the particle and

$$q_i^{(\mathrm{iv})}(r,\theta) = q_i(r,\theta)\frac{M_{11}(r)/r}{M_{11}(a)/a}, \quad \gamma = \frac{M'_{11}(a)a}{M_{11}(a)}. \quad (15)$$

If the phase transition on the particle's surface is absent, then $\alpha = 0$ and $K_{Tsl}^{(e)} = \frac{K_{Tsl}\eta}{\rho}$ [1]. Hence, we obtain the formula for the velocity $\mathbf{U}^{(\mathrm{iv})}$ of an inhomogeneous nonvolatile particle (assuming $M_{11}(r) \equiv r$, we can find the velocity $\mathbf{U}^{(\mathrm{hn})}$ of a homogeneous nonvolatile particle on the basis of this formula). Similarly, assuming $M_{11}(r) \equiv r$, it is possible to obtain from formula (14) the velocity $\mathbf{U}^{(\mathrm{hs})}$ of a homogeneous sublimating particle. Considering sublimating particles, we deal with small concentrations. Therefore, we can suggest that $K_{Tsl}^{(e)} = \frac{K_{Tsl}\eta}{\rho}$, $n_{02} = n_0$, and $\rho_0 = \rho$. Then,

$$\mathbf{U}^{(\mathrm{is})} = \mathbf{U}^{(\mathrm{iv})}\frac{1 + 0.5\alpha\left[1 + \frac{\rho K_{sl} D\delta T_{0e}}{K_{Tsl}\eta} + \frac{D\delta T_{0e} n_0 m_1}{K_{Tsl}\eta}\right]\frac{\nu a}{D}}{1 + 0.5\alpha\left[1 + \frac{2D\delta L m_1 n_0}{2\kappa_e + \gamma\kappa_i}\right]\frac{\nu a}{D}}. \quad (16)$$

In the case in which ice on the particle surface melts and evaporates into air, this formula takes the form [7]

$$\mathbf{U}^{(\mathrm{is})} = \mathbf{U}^{(\mathrm{iv})}\frac{1 + 45.41\alpha}{1 + 37.77\alpha\left(0.75 + \frac{0.25}{\gamma}\right)}. \quad (17)$$

In order to analyze this formula, we consider exponential dependence (12) as a model problem. At a distance of one particle's radius, let the drop in $\kappa_i(r)$ obey the following condition: $0.1 \le \frac{\kappa_i(a)}{\kappa_i(0)} \le 10$. As was mentioned above, the quantity $M_{11}(r)$ is determined by formula (13), provided that $\kappa_i(r)$ is determined by formula (12). From (13) and (15), it follows that the quantity γ ranges from 0.59 to 1.81. When α varies between 0 and 1, the correction factor in formula (17) varies in the following limits: from 1 to 1.024 at $\gamma = 0.59$; from 1 to 1.197 at $\gamma = 1$; and from 1 to 1.343 at $\gamma = 1.81$. Thus, taking account of the evaporation effect can significantly contribute to the photophoresis rate of a homogeneous particle, whereas allowance for the effect of inhomogeneous thermal conductivity can increase and decrease this contribution.

REFERENCES

1. Yu. I. Yalamov and V. S. Galoyan, *Dynamics of Drops in Heterogeneous Viscous Mediums* (Luĭs, Erevan, 1985) [in Russian].
2. L. D. Landau and E. M. Lifshitz, *Course of Theoretical Physics*, Vol. 6: *Fluid Mechanics* (Nauka, Moscow, 1986; Pergamon, New York, 1987).
3. E. R. Shchukin, Yu. I. Yalamov, and Z. L. Shulimanova, *Special Problems of Aerosols Physics* (Moscow Pedagogical Univ., Moscow, 1992) [in Russian].
4. Yu. I. Yalamov and A. S. Khasanov, Zh. Tekh. Fiz. **74** (7), 13 (2004) [Tech. Phys. **49**, 818 (2004)].
5. V. I. Smirnov, *Course of Higher Mathematics* (Addison-Wesley, Reading, Mass., 1964; Nauka, Moscow, 1965), Vol. 2.
6. J. Happel and H. Brenner, *Hydrodynamics at Low Reynolds Numbers* (Prentice-Hall, Englewood Cliffs, New Jersey, 1965; Mir, Moscow, 1976).
7. N. B. Vargaftik, *Tables of the Thermophysical Properties of Liquids and Gases*, 2nd ed. (Halsted Press, New York, 1975; Nauka, Moscow, 1972).

Translated by Yu. Vishnyakov

Doklady Physics, Vol. 50, No. 7, 2005, pp. 337–342. Translated from Doklady Akademii Nauk, Vol. 403, No. 3, 2005, pp. 319–324.

PHYSICS

Study of the *Q* Factor of the Impurity Resonance Mode in the Microstrip Model of a 1D Photonic Crystal

B. A. Belyaev, A. S. Voloshin, and Academician V. F. Shabanov

Received March 24, 2005

Artificial structures with periodic inhomogeneities whose sizes are comparable with the electromagnetic wavelengths in a certain (e.g., optical) range are called photonic crystals. Such structures are present as systems of coupled resonators and, hence, have transparent windows and stopbands [1]. The physical properties of the periodic structures are determined both by the materials and the construction features of inhomogeneities, whose parameters can be varied over wide ranges by changing the technological conditions of their production. Investigations of photonic crystals are of great applied interest in view of the possibility of using them to create various optical devices, such as filters and mirrors with high characteristics. Moreover, these investigations are of great fundamental interest, because they make it possible to study the features of the propagation and localization of electromagnetic waves in the space of interacting resonators.

Photonic crystals can be one-dimensional, as well as complex two- and three-dimensional. However, even the production of 1D photonic crystals is an expensive process that requires special equipment. For this reason, it is appropriate to perform preliminary experimental and theoretical investigations of the properties of photonic crystals with bulk (nonfilm) analogs operating, e.g., in the UHF band. The most successful analog of 1D dielectric photonic crystals—alternating layers with different refractive indices—is a microstrip structure for which the quasistatic calculation is in quite good agreement with experiment [2, 3].

The principle of designing microstrip models of photonic crystals is based on the strong dependence of the effective dielectric constant ε_{eff} of a microstrip transmission line on the strip-conductor width and substrate thickness. The propagation velocity and, correspondingly, the electromagnetic wavelength in the line are determined by ε_{eff}, which can be expressed in terms of the relative dielectric constant ε of the substrate and the basic construction parameters of the line [4]. In this case, the microstrip model of a photonic crystal consists of sequentially connected alternating sections: those with a large width of the strip conductor imitating layers with high refractive indices, and those with a small width of the conductor imitating layers with low refractive indices. The input and output in such a structure are usually formed by coaxial-strip junctions with a characteristic impedance of 50 Ω, which are conductively connected to the outer strip-conductor sections [3].

Figure 1a shows the frequency responses of (solid line) insertion and (dashed line) return losses, as well as the topology of the conductors of the microstrip model of the 1D photonic crystal, which consists of seven resonator layers and whose lattice constant is a_1 [3]. The structure is adjusted as a bandpass filter with the central frequency f_0 = 3 GHz of the passband and the relative width $\frac{\Delta f}{f_0}$ = 40% of this band as measured at a level of –3 dB from the minimum-loss level. Such photonic crystals have numerous equidistant transparent windows, where the electrical (optical) lengths of each layer at the central frequency are odd multiples of π, and stopbands at the center of which the electrical lengths of the layers are multiples of $\frac{\pi}{2}$ [5]. It is important that the dielectric constants and characteristic impedances of microstrip transmission lines are characterized by a frequency dispersion whose character is determined by the geometric parameters of the lines and by the dielectric constant of the substrate [6]. Owing to this dispersion, the irregularity of the frequency response in passbands higher than the first band increases, a situation that is due to the appearance of considerable UHF-power reflections associated both with the breakdown of the balance of couplings between resonators and the difference between their resonance frequencies.

Figure 1b shows the frequency responses and topology of the conductors of the microstrip model of the 1D two-sublattice photonic crystal whose lattice constant is a_2 [7]. For appropriate comparison, this structure is also adjusted as a bandpass filter with f_0 = 3 GHz and a

Kirenskiĭ Institute of Physics, Siberian Division, Russian Academy of Sciences, Akademgorodok, Krasnoyarsk, 660036 Russia
e-mail: belyaev@iph.krasn.ru

1028-3358/05/5007-0337$26.00

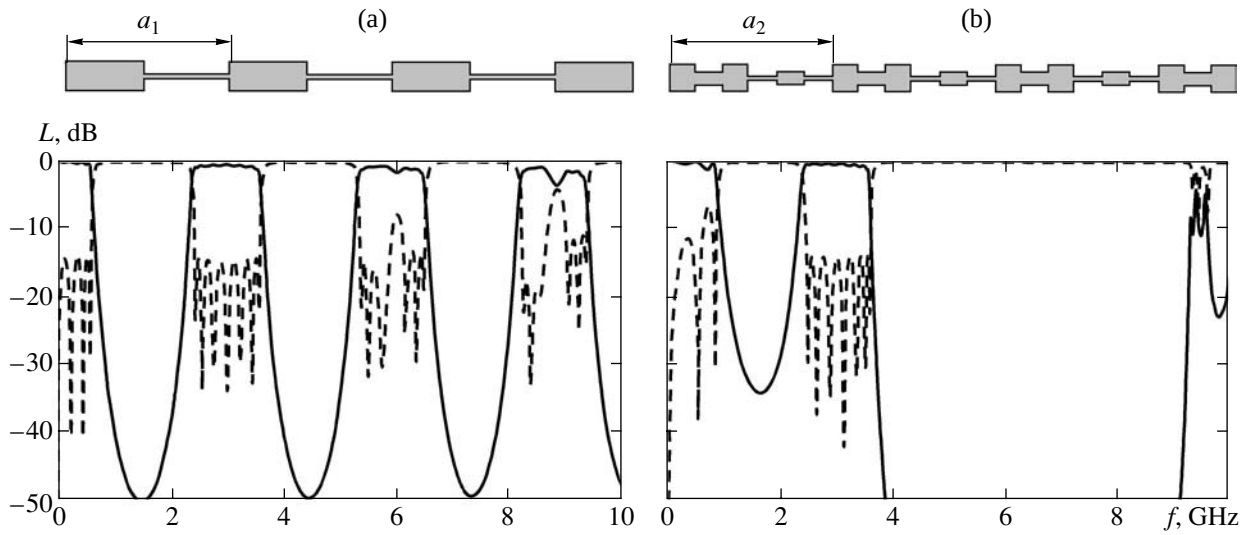

Fig. 1. Frequency responses for microstrip models of a 1D photonic crystal with (a) a standard lattice and (b) a lattice consisting of two sublattices. The solid and dashed lines are insertion and return losses, respectively.

relative width of $\frac{\Delta f}{f_0}$ = 40%. In contrast to one-sublattice photonic crystals, a several-fold increase in the width and depth of the stopband under consideration can be achieved in this photonic crystal. This property allows the production of high-quality dielectric multilayer mirrors that operate in a frequency band much larger than the octave, and the almost complete reflection of electromagnetic waves is observed in this band without any parasitic passbands.

The study of UHF models of devices based on photonic crystals makes it possible not only to reduce the cost and time investments in the development stage but also to obtain important recommendations for achieving the extreme characteristics of the construction under investigation. In particular, the simulation of 1D photonic crystals [3, 7] shows that a number of conditions are necessary for manufacturing high-quality bandpass filters and mirrors. First, the necessary jump, which is determined by a given passband of a device or a given width of a stopband, must be ensured between the characteristic impedances of the outer layers of a photonic crystal and the characteristic impedances of the input and output. Second, it is necessary to select the dielectric constants of the layers of the superlattice such that the couplings between them are in balance, which must also correspond to the given passband of the filter. Third, the electrical lengths of resonator layers should be selected such that their natural frequencies coincide with the central frequency of the passband. In other words, for a given passband of the optical filter, it is necessary to ensure (i) the necessary jumps between the refractive indices of the materials of the outer layers of the structure and the refractive indices of the input and output media, (ii) the required jumps between the refractive indices of the materials of all layers of the structure, and (iii) the coincidence of the resonance frequencies of the layers with the central frequency of the passband, which can be achieved by selecting the optical lengths of the layers.

We note that the frequency ranges where the reflectivity for light incident on the photonic crystal is close to unity are called photonic band gaps. The introduction of a defect (such as a layer whose thickness or dielectric constant differs from the respective value of the basic periodic structure) into the photonic crystal evidently leads to the distortion of the frequency response due to the appearance of resonances in this defect layer. Such defects are called impurities, and their frequency spectrum is called impurity oscillation modes. It is known that the impurity mode resonance has the high loaded Q factor Q_{imp} when it coincides with the center of the photonic band gap [8, 9]. It is convenient to use irregular microstrip structures in order to analyze the possibility of increasing the Q factor of the impurity mode resonance by optimizing the construction parameters of the photonic crystal and defect [2, 10]. This work is devoted to such an analysis.

Figure 2 shows the topologies of conductors and frequency responses of microstrip constructions that are models of 1D photonic crystals with possible basic defects shown by closed boxes on the topologies of the conductors. For simplicity, each photonic crystal contains only two unit cells and one defect, and the frequency dispersion of both the effective dielectric constant and the characteristic impedance of the microstrip lines is disregarded in the calculation. Transverse electromagnetic waves propagate in transmission lines called T lines. For the appropriate comparison of the loaded Q factor Q_{imp} of the impurity mode resonance, the proper Q factor of all sections of the models of photonic crystals, including defects, is assumed to be $Q_0 = \infty$. In addition, the parameters of the structure in

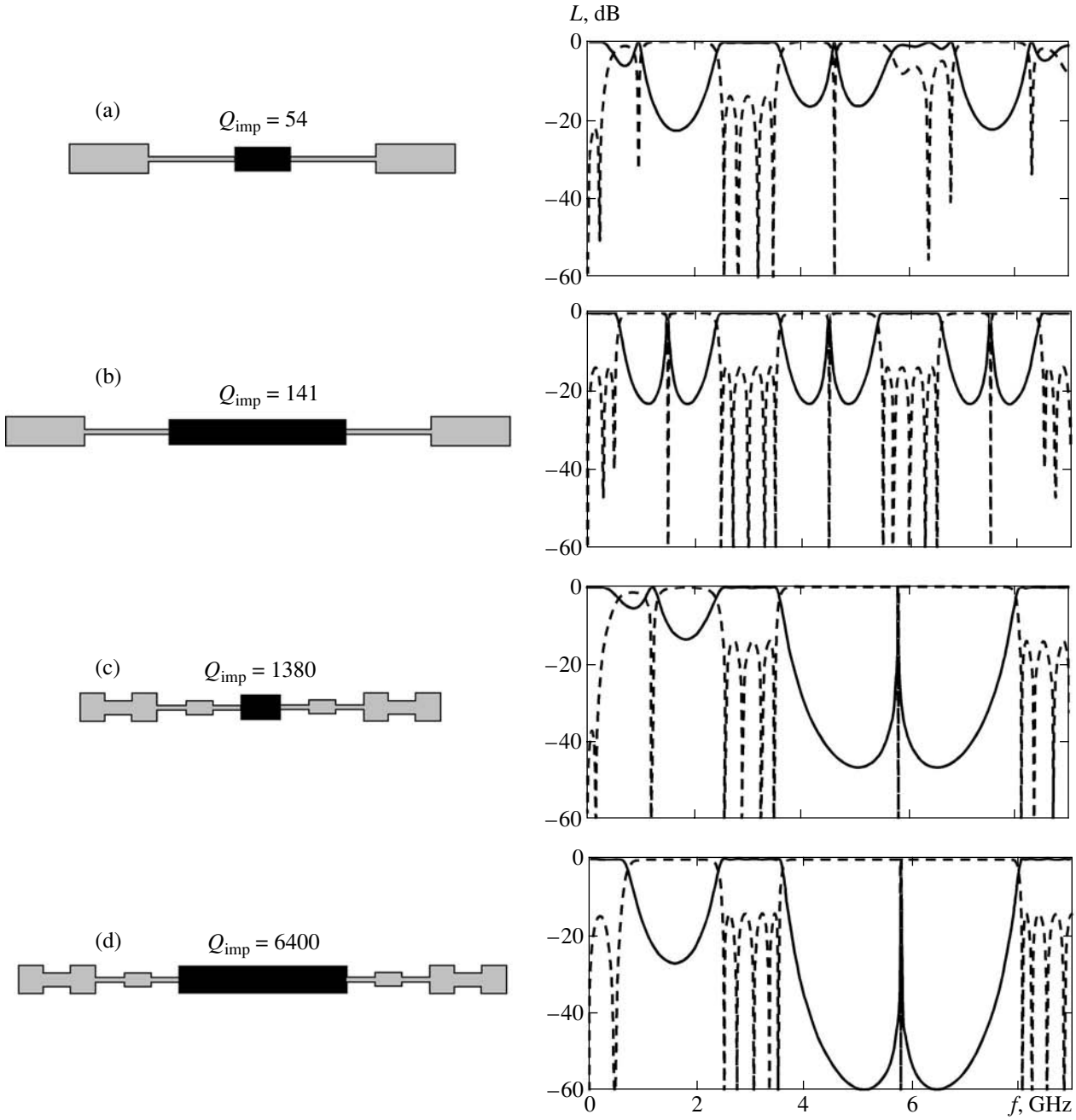

Fig. 2. Microstrip constructions of the 1D photonic crystals under investigation with various lattice defects and their frequency responses. The solid and dashed lines are insertion and return losses, respectively.

each construction under consideration are chosen so that the central frequency of the first passband is equal to f_0 = 3 GHz, the relative width of this band as measured at a level of –3 dB is equal to $\frac{\Delta f}{f_0}$ = 40%, and the maxima of return losses in this passband are equal to –14 dB. The loaded *Q* factor of the impurity resonance mode Q_{imp} is determined as the ratio of the resonance frequency f_{imp} to the resonance linewidth Δf_{imp} as measured at a level of –3 dB.

In the first variant (see Fig. 2a), the photonic crystal consists of one sublattice and the electrical length of the defect in it is approximately two-thirds of the electrical length of the remaining four regular sections of the structure whose half-wavelength resonances form the first passband. In this case, the lowest resonance of the defect coincides with the center of the second stopband or the second photonic band gap.

In the second variant (see Fig. 2b), the electrical length of the defect is approximately twice as large as the electrical lengths of the other sections of the struc-

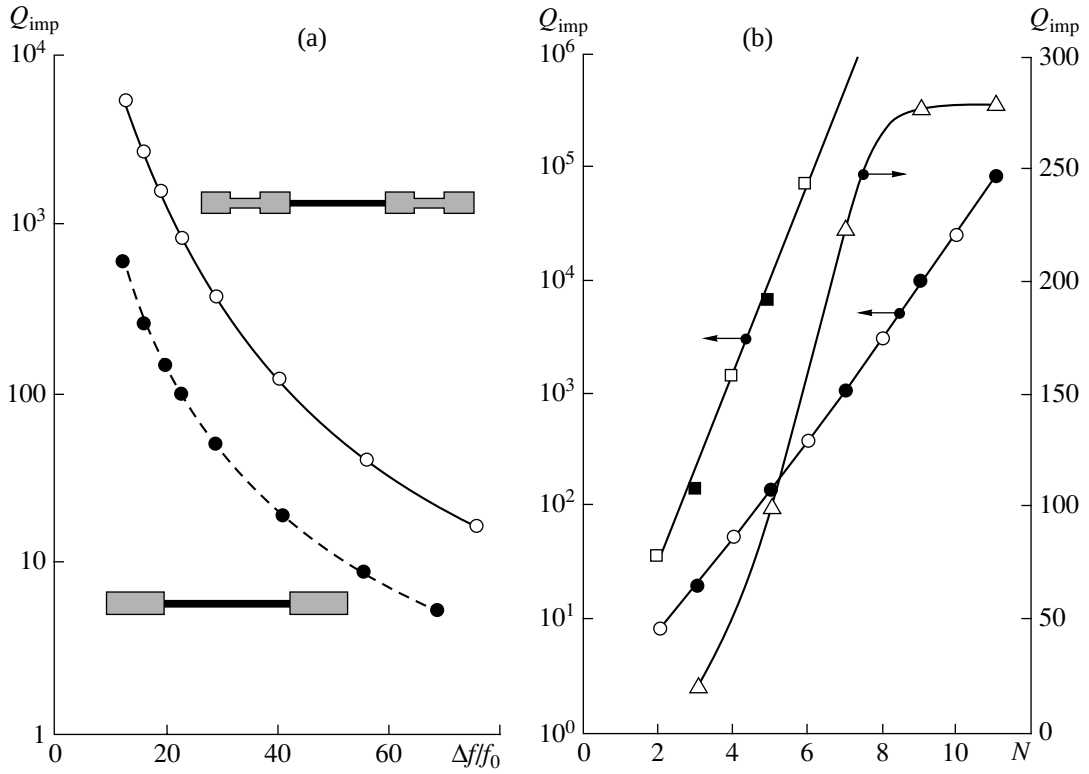

Fig. 3. Q factor of the impurity resonance mode vs. (a) the relative width of the passband of three-link constructions and (b) the number of links in the structure.

ture. Therefore, its first resonance lies in the first band gap, and the second resonance, along with the resonances of the four basic sections of the structure, is involved in the formation of the first passband. This fact is manifested in the frequency dependence of return losses, where five minima corresponding to five resonances are well pronounced in the first passband. The resonance of the third oscillation mode of the defect lies in the second band gap, and its loaded Q factor is shown in Fig. 2b for comparison. The resonance of the fourth oscillation mode of the defect is involved in the formation of the second passband, which is also seen in the frequency dependence of return losses, etc.

In the third variant (see Fig. 2c), the photonic crystal consists of two sublattices and the electrical length of the defect is such that the resonance of its first oscillation mode coincides with the center of the second band gap. Finally, in the fourth variant (see Fig. 2d), the photonic crystal also has two sublattices and the electrical length of the defect is such that its first resonance is involved in the formation of the first passband, the second resonance coincides with the center of the second band gap, and the third resonance is involved in the formation of the third passband.

As is known, the loaded Q factor of the resonator that has an infinite proper Q factor and is connected "in line" is determined only by its coupling with the input and output transmission lines. In the microstrip structures under consideration (see Fig. 2), the extent of coupling of the resonator defect with the transmission lines, as well as its loaded Q factor, is presented by the value of damping for electromagnetic waves in the photonic band gap in which its resonance lies. For this reason, a change in the electrical length of the defect, leading to a corresponding shift in the resonance from the center of the photonic band gap to a certain edge, reduces the loaded Q factor of the impurity mode. Investigations show that the loaded Q factor of the impurity mode increases strongly when the first and second resonances of the defect are involved in the formation of the first and second passbands of the two-sublattice photonic crystal, respectively. In this case, Q_{imp} of the impurity is much higher for two-sublattice constructions.

The coupling of the resonator defect with the transmission lines can evidently be controlled by varying the construction parameters and the number of unit cells in the photonic crystal model. In particular, it is known that an increase in the difference between the reflective indices of the layers in the dielectric photonic crystal reduces the width of passbands in it and correspondingly increases the width and depth of band gaps, which, in turn, necessarily affects the loaded Q factor of the impurity. Figure 3a shows the Q factor of the defect on the relative width of the first passband of the structure for (dashed line) one-sublattice and (solid line) two-sublattice photonic crystals. In this investigation,

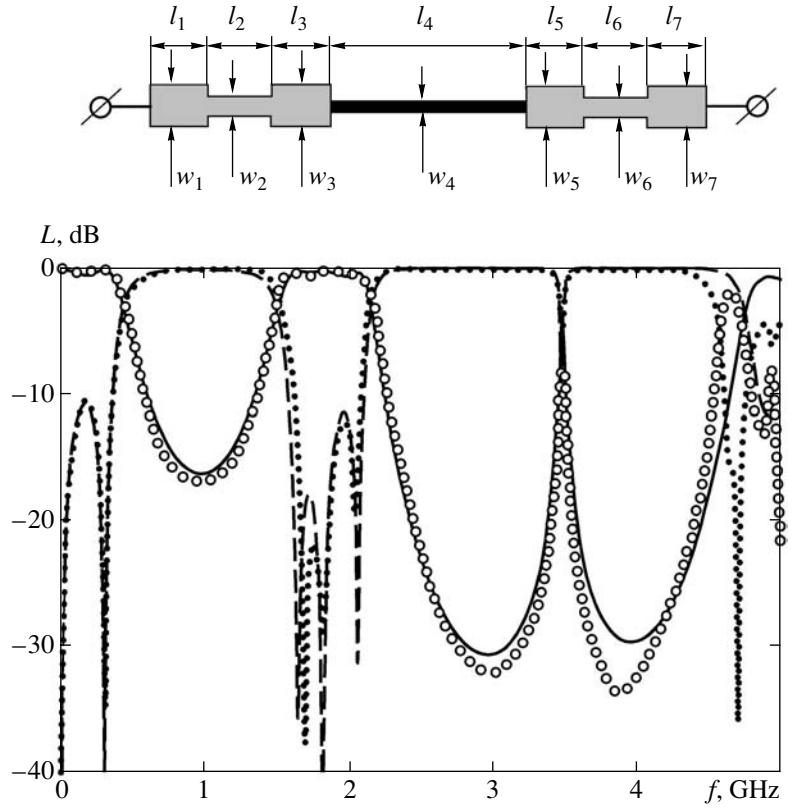

Fig. 4. (Upper panel) Topology of the conductors and (lower panel) frequency responses of the insertion and return losses (line) calculated and (points) measured for the microstrip model of the 1D two-sublattice photonic crystal with a defect.

simple microstrip models are used, and the topologies of their conductors are also shown in this figure. In these models, the first passband is formed by only three resonances, including the defect resonance: it is the first or second resonance for the two- or one-sublattice crystal, respectively. It is seen that, as the relative width $\frac{\Delta f}{f_0}$ of the passband decreases, Q_{imp} increases sharply. In this case, the Q factor of the defect in the two-sublattice crystal is an order of magnitude higher for any fixed width of the passband.

Investigations of the loaded Q factor Q_{imp} as a function of the number of unit cells forming the photonic crystal are of great interest. Figure 3b shows the loaded Q factor Q_{imp} as a function of the number N of resonances forming the first passband for (open and closed circles for constructions (a) and (b) in Fig. 2, respectively) the one-sublattice photonic crystal and (open and closed squares for constructions (c) and (d) in Fig. 2, respectively) the two-sublattice photonic crystal. These plots are drawn for the relative width of the first passband $\frac{\Delta f}{f_0} = 40\%$ and $f_0 = 3$ GHz. The gray triangles in Fig. 3b are $Q_{\text{imp}}(N)$ for a microstrip analog of the two-sublattice photonic crystal, where the real proper Q factor $Q_0 = 280$ of microstrip lines is used. As is seen, this curve is saturated at $N = 9$, approaching the proper Q factor of microstrip lines, whereas the remaining presented curves increase exponentially. It is important that the Q factor of the impurity resonance mode in the two-sublattice photonic crystal increases with N much faster than that for the one-sublattice photonic crystal.

An experimental test of several microstrip constructions manufactured by engraving a lacquer [11] showed good agreement with the numerical calculations in quasistatic approximations for 1D models of irregular structures. As an example, Fig. 4 shows (points) measurements of insertion and return losses for the microstrip model of the two-sublattice photonic crystal with a defect in comparison with (lines) the corresponding calculations. The $60 \times 16 \times 2$-mm substrate was made of B20 ceramic ($\varepsilon = 20$). The topological pattern for the conductors of this device was previously obtained by parametrically synthesizing the bandpass filter with a central frequency of $f_0 = 1.8$ GHz and a relative passband width of $\frac{\Delta f}{f_0} = 35\%$. However, the experiment was compared with theoretical calculations using the actual construction parameters of the microstrip structure that were measured after its manufacture.

The topological parameters of the conductors of the microstrip model of the two-sublattice photonic crystal with a defect (see Fig. 4) on a 2-mm substrate with the dielectric constant $\varepsilon = 20$ are as follows:

i	1	2	3	4	5	6	7
l_i, mm	4.62	5.45	4.72	25.08	4.68	5.46	4.71
w_i, mm	8.06	3.49	11.67	0.14	11.66	3.47	8.06

The loaded Q factor of the impurity resonance mode $Q_{\text{imp}} \approx 96$ that was measured for the microstrip structure under investigation is in fairly good agreement with the $Q_{\text{imp}} \approx 105$ obtained from numerical quasistatic analysis.

Thus, the loaded Q factor of the impurity resonance mode has been analyzed for the microstrip model of a 1D photonic crystal with a defect. It has been shown that, when the impurity resonance frequency coincides with the center of a photonic band gap, Q_{imp} increases with the damping of electromagnetic waves in this gap. For this reason, the loaded Q factor of the impurity depends not only on the number of dielectric layers (unit cells) forming the photonic crystal [2] but also on the relative width of the passband and on the construction features of the photonic crystal. In particular, the impurity-mode Q factor in the two-sublattice photonic crystal can be much higher than that in the one-sublattice photonic crystal. Moreover, Q_{imp} increases when low-lying resonances of the impurity are involved in the formation of the first passband. The quasistatic numerical analysis of microstrip models of photonic crystals with impurities is in good agreement with experiment. Hence, the construction parameters of a model of a 1D photonic crystal with a defect can be obtained such that a given loaded Q factor of the impurity mode is ensured.

REFERENCES

1. E. Yablonovitch, Phys. Rev. Lett. **58**, 2059 (1987).
2. H. Kitahara, T. Kawaguchi, J. Miyashita, and M. Wada Takeda, J. Phys. Soc. Jpn. **72** (4), 951 (2003).
3. B. A. Belyaev, A. S. Voloshin, and V. F. Shabanov, Dokl. Akad. Nauk **395** (6), 756 (2004) [Dokl. Phys. **49**, 213 (2004)].
4. V. I. Gvozdev and E. I. Nefedov, *Three-Dimensional Microwave Integrated Circuits* (Nauka, Moscow, 1985) [in Russian].
5. H. A. Macleod, *Thin-Film Optical Filters* (Adam Hilger, London, 1969).
6. M. Kirschning and R. H. Jansen, Electron. Lett. **18** (6), 272 (1982).
7. B. A. Belyaev, A. S. Voloshin, and V. F. Shabanov, Dokl. Akad. Nauk **400** (2), 181 (2005) [Dokl. Phys. **50**, 7 (2005)].
8. S. Ya. Vetrov and A. V. Shabanov, Zh. Éksp. Teor. Fiz. **120**, 1126 (2001) [JETP **93**, 977 (2001)].
9. P. Kramper, A. Birner, *et al.*, Phys. Rev. B **64**, 233102 (2001).
10. D. Nesic, Microwave Opt. Technol. Lett. **37** (3), 201 (2003).
11. B. A. Belyaev, A. V. Kazakov, A. A. Leksikov, and I. Ya. Makievskiĭ, Prib. Tekh. Éksp., No. 1, 167 (1998).

Translated by R. Tyapaev

Doklady Physics, Vol. 50, No. 7, 2005, pp. 343–345. Translated from Doklady Akademii Nauk, Vol. 403, No. 3, 2005, pp. 325–327.

PHYSICS

Trigonal Distortion of Ferropericlase $(Mg_{0.8}Fe_{0.2})O$ at High Pressures

I. Yu. Kantor[1,2], L. S. Dubrovinsky[2], A. P. Kantor[1,2], Academician V. S. Urusov[1], C. McCammon[2], and W. Crichton[3]

Received January 12, 2005

Transition-metal monoxides (MnO, FeO, CoO, NiO) are of great interest for solid-state physics in virtue of their magnetic, electron, and structural characteristics, which underlie the wide technological applications of this group of materials. These oxides are typical antiferromagnets with a cubic crystal structure of the NaCl type (structural type B1) above the Néel temperature (T_N). Below T_N, these oxides undergo a structural transition of the distortion type (corresponding to the lowering of symmetry to a trigonal or tetragonal one). The structural phase transition occurs within approximately the same temperature range in which the magnetic ordering arises. Therefore, until recently, it was commonly believed that the loss of symmetry in these oxides stems from the ordering of magnetic moments in the crystal structure [1]. The growth of pressure at room temperature leads to similar distortion-type phase transformations in MnO, FeO, CoO, and NiO. Since the Néel temperature has a positive baric coefficient (increases with pressure), it has been suggested [2] that the structural transitions in these materials under high pressures have the same nature as those occurring at low temperatures. Recent studies of the magnetic and elastic characteristics of wustite (FeO) at high pressures [3, 4] have demonstrated that the onset of magnetic ordering in wustite takes place at about 5 GPa. This pressure is significantly lower than that corresponding to the structural phase transition (about 17 GPa). In light of these results, it becomes clear that the relation between magnetic ordering and structural distortion needs a revision—for FeO at the very least.

To make the magnetic interactions weaker or to get rid of them completely, it is possible to "dilute" wustite by means of an isostructural diamagnetic compound that forms a continuous series of solid solutions with FeO. A suitable component is periclase MgO, which forms a continuous series of solid solutions $(Mg_{1-x}Fe_x)O$ with wustite (referred to as magnesiowustite at $x \geq 0.5$ and ferropericlase at $x < 0.5$). MgO periclase does not undergo any phase transformations and remains cubic up to at least 227 GPa [5]. The properties of ferropericlase with an FeO content of about 15–20 mol % are of great interest for the Earth sciences, as it is common knowledge that it represents one of the main rock-forming minerals in the lower mantle of the Earth [6].

We have performed experimental studies on the Mössbauer effect and on the x-ray diffraction patterns of ferropericlase $(Mg_{0.8}Fe_{0.2})O$. The latter composition is close to that expected for the Earth's mantle. The experiments at room temperature and high pressures (up to 60 GPa) were performed using the diamond anvil cell [7]. The diameter of the diamond working surface (culet) was 0.25 mm. In the experiments, we used a rhenium spacer with an initial thickness of 0.26 mm, which was pressed between the diamonds down to a thickness of about 60 μm. The high-pressure chamber was 0.125 mm in diameter. In addition to the powder sample, several small ruby spheres (about 1–2 μm in diameter) were put into the chamber in order to measure pressure in the anvil cell by the shift of the fluorescence lines of chromium ions.

The Mössbauer spectroscopy of the ^{57}Fe isotope is in fact the only reliable method for determining the *in situ* magnetic, valence, and spin states of iron atoms in the diamond anvil cell. Since the sample volume was very small, we used a synthesized sample with the nominal composition $(Mg_{0.8}Fe_{0.2})O$ artificially enriched (up to 50%) by the ^{57}Fe isotope. The measurements were performed using a spectrometer of the constant-acceleration type with a highly active point (about 200 μm in size) ^{57}Co radioactive source in the rhodium matrix. The iron foil was used as a reference sample for determining the Doppler velocity. According to the model [8], the obtained spectra were decomposed into two doublets corresponding to the bivalent and trivalent

[1] *Moscow State University, Vorob'evy gory, Moscow, 119899 Russia*

[2] *Bayerisches Geoinstitut, Universität Bayreuth, D-95440 Bayreuth, Germany*

[3] *European Synchrotron Radiation Facility (ESRF), 6 rue Jules Horowitz, BP 220, 38043 Grenoble CEDEX 9, France*

1028-3358/05/5007-0343$26.00

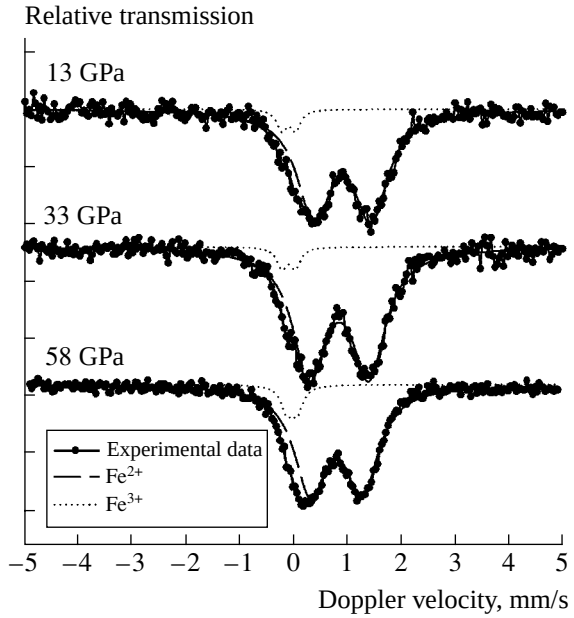

Fig. 1. Mössbauer spectra of ferropericlase $(Mg_{0.8}Fe_{0.2})O$ at pressures of 13.33 GPa and 58 GPa. The dashed and dotted lines correspond to Fe^{2+} and Fe^{3+}, respectively. Here and below, zero in the velocity axis corresponds to metallic iron.

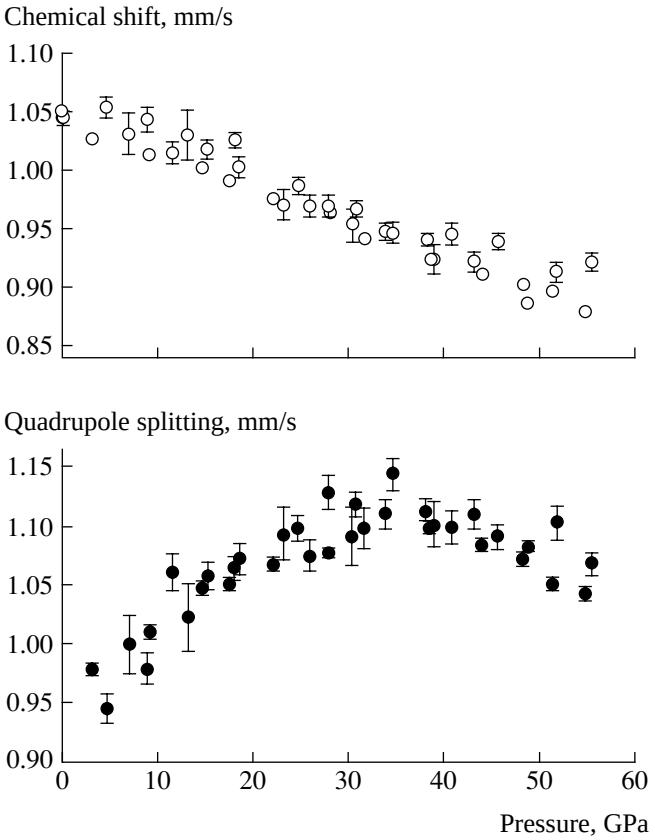

Fig. 2. Pressure dependence of the isomer shift and quadrupole splitting for the main doublet of Fe^{2+} in the Mössbauer spectra of $(Mg_{0.8}Fe_{0.2})O$.

states of iron (Fig. 1). The Fe^{3+} content in the sample related to a certain number of structural defects remained constant and was equal to about 4% of the overall iron content. The paramagnetic doublet has two parameters characterizing the hyperfine interaction: the isomer shift and the quadrupole splitting. The isomer shift characterizes valence, spin, and (to a smaller extent) coordination states of the absorbing atom. The measured shift of the main doublet exactly corresponds to the high-spin state of Fe^{2+} ions and linearly decreases with the pressure growth (Fig. 2). The latter decrease can be explained by the growth of electron density in the region of nuclei of iron ions due to the compression of the material. The variation of quadrupole splitting is nonmonotonic (Fig. 2): the splitting increases up to 35 GPa and decreases at higher pressures. We observe no baric hysteresis with an increase or decrease in pressure. The quadrupole splitting is a sensitive probe, indicating the degree of distortion for the coordination polyhedron. The decrease in quadrupole splitting observed at pressures exceeding 35 GPa can stem from the distortion of FeO_6 octahedron, which is similar to that occurring in clinoferrosilite $(Mg,Fe)SiO_3$ [9]. We wanted to find out whether this distortion is local or is induced by a structural transition, i.e., related to the symmetry changes in the structure of the material. To this end, we performed the powder x-ray diffraction study at high pressures. The x-ray diffraction patterns were recorded *in situ* using an ID30 high-pressure setup at the European Synchrotron Radiation Facility (ESRF) in Grenoble, France. The patterns were recorded at a constant x-ray wavelength of 0.3738 Å. Until pressures of the order of 35 GPa, the x-ray diffraction patterns exactly correspond to the NaCl-type cubic structure. With further growth of pressure, some reflections exhibited a substantial broadening. The trigonal distortion of the cubic lattices (induced by contraction or stretching along one of the triple axes) manifests itself in the splitting of some x-ray reflections. In particular, (111), (220), (311), and (220) reflections become split, whereas (200) and (400) reflections undergo no splitting. Near the transition point, the deviations from cubic symmetry are very small, and the splitting of reflections manifests itself in the broadening of diffraction peaks. Therefore, to determine the phase transition point, we used the ratio of FWHM (full width at half maximum) values for (200) and (220) reflections [10]. For our sample, this ratio remains constant up to 35 GPa and starts to steeply increase at higher pressures (Fig. 3). The analysis of x-ray diffraction patterns at 42 GPa demonstrates that the splitting of all reflections except (200) and (400) ones agrees with the trigonal symmetry of the lattice, and the ratio $(\frac{c}{a})$ of lattice parameters is smaller than that for the rhombohedral unit cell of the ideal cubic structure. This corresponds to the contraction of the cubic lattice along one of the triple axes.

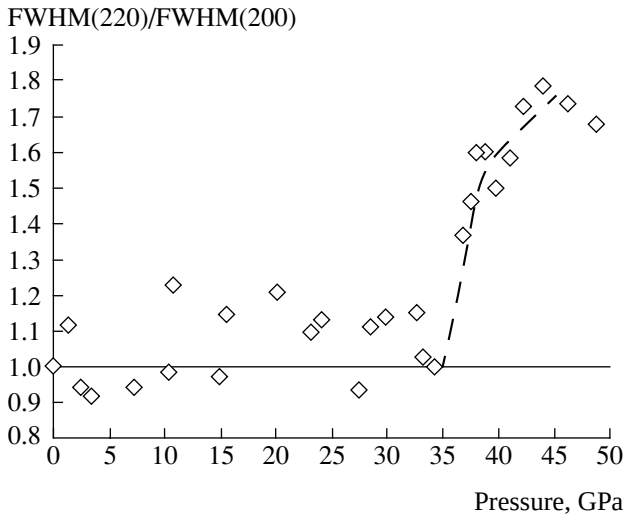

Fig. 3. Ratio of widths (FWHM) for (200) and (220) reflections as a function of pressure. The steep broadening of the (220) line starts at 35 GPa.

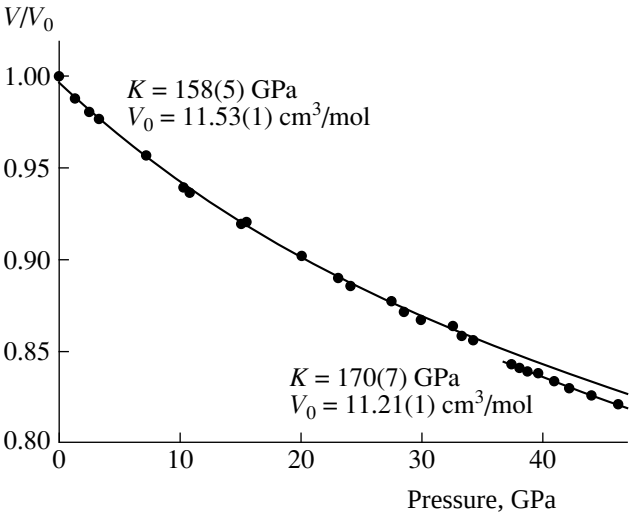

Fig. 4. Compressibility $(\frac{V}{V_0})$ of ferropericlase $(Mg_{0.8}Fe_{0.2})O$ as a function of pressure. Solid lines correspond to the Birch–Murnagham isothermal equation of state for the cubic and trigonal phases.

Based on the measured pressure dependence for the sample volume, we have determined the parameters involved in the Birch–Murnagham isothermal equation of state, which can be written in the form

$$P = \frac{3}{2}K\left[\left(\frac{V_0}{V}\right)^{2/3} - 1\right]\left(\frac{V_0}{V}\right)^{7/5},$$

where K is the isothermal bulk modulus, V_0 is the volume at zero pressure, and V is the volume at a pressure P. For the cubic phase, we have K = 158(5) GPa and V_0 = 11.53(1) cm^3/mol; for the trigonal phase, K = 170(7) GPa and V_0 = 11.21(1) cm^3/mol (Fig. 4).

Based on the x-ray diffraction data and the results of Mössbauer spectroscopy, we have arrived at a conclusion concerning the existence of trigonal distortion in ferropericlase $(Mg_{0.8}Fe_{0.2})O$ at 35 GPa and room temperature. The Mössbauer spectroscopy suggests that this transition is not related to magnetic ordering, and, hence, the existing concepts concerning the relation between antiferromagnetism and structural distortions in transition-metal oxides should be revised. The obtained results are in good agreement with computer simulations that make use of semi-empirical atomic potentials [11]. These simulations show that the rhombohedral distortion of FeO wustite at high pressures is a consequence of multiparticle metal–oxygen interactions.

Structural transitions similar to the type discussed in this paper are usually related to a steep decrease in the cubic elastic modulus C_{44} [12], and, hence, to a decrease in the velocity of transverse seismic waves. The latter conclusion may be especially important for the description of seismic inhomogeneity in the lower mantle of the Earth.

ACKNOWLEDGMENTS

This work was supported by the Council of the President of the Russian Federation for Support of Young Russian Scientists and Leading Scientific Schools, project no. NSh-1955.2003.5, and Deutsche Forschungsgemeinschaft, grant no. MC 3/13-1.

REFERENCES

1. J. S. Smart and S. Greenwald, Phys. Rev. **82**, 113 (1951).
2. V. V. Struzhkin, H. K. Mao, J. Hu, *et al.*, Phys. Rev. Lett. **87**, 255501 (2001).
3. I. Yu. Kantor, C. A. McCammon, and L. S. Dubrovinsky, J. Alloys Compd. **376**, 5 (2004).
4. A. P. Kantor, S. D. Jacobsen, I. Yu. Kantor, *et al.*, Phys. Rev. Lett. **93**, 215502 (2004).
5. T. S. Duffy, R. J. Hemley, and H. K. Mao, Phys. Rev. Lett. **74**, 1371 (1995).
6. A. E. Ringwood, *Composition and Petrology of the Earth's Mantle* (McGraw-Hill, New York, 1975; Nedra, Moscow, 1981).
7. N. Dubrovinskaia and L. Dubrovinsky, Rev. Sci. Instrum. **74**, 3433 (2003).
8. D. P. Dobson, N. S. Cohen, Q. A. Pankhurst, *et al.*, Am. Mineral. **83**, 794 (1998).
9. C. A. McCammon and C. Tennant, in *Mineral Spectroscopy: A Tribute to Roger G. Burns*, Special Publication (Geochem. Soc., Houston, 1996), No. 5.
10. W. Mao, J. Shu, J. Hu, *et al.*, J. Phys.: Condens. Matter **14**, 11349 (2002).
11. I. Yu. Kantor and V. S. Urusov, Dokl. Akad. Nauk **391**, 467 (2003) [Dokl. Phys. **48**, 394 (2003)].
12. Y. Sumino, M. Kumazawa, O. Nishizawa, *et al.*, J. Phys. Earth **28**, 475 (1980).

Translated by K. Kugel

Doklady Physics, Vol. 50, No. 7, 2005, pp. 346–348. Translated from Doklady Akademii Nauk, Vol. 403, No. 2, 2005, pp. 183–186.

TECHNICAL PHYSICS

Effect of Hydrogenation on Magnetic Phase Transitions in the $Er_2Fe_{14}B$ Single Crystal

Corresponding Member of the RAS G. S. Burkhanov[1], I. S. Tereshina[1,*], O. D. Chistyakov[1], E. A. Tereshina[2], and H. Drulis[3]

Received February 17, 2005

Over the last two decades, the development of permanent magnets based on $Nd_2Fe_{14}B$ [1] and the rapid implementation of their industrial production have stimulated investigations into the magnetic properties of compounds of $R_2Fe_{14}B$ with other rare earth metals (REMs), such as Ho, Er, Tm, and Yb. Complex borides containing these REMs are characterized not only by quite high Curie temperatures T_C but also by various spin-reorientation phase transitions. Among these borides, $Er_2Fe_{14}B$ (T_C = 554 K) is of particular interest, because it undergoes a spin-reorientation phase transition at a temperature T_{SR} = 327 K that is close to room temperature. This transition is associated with a step change in the easy magnetization axis from the basal plane to the tetragonal axis *c* [2]. This property makes it possible to use materials based on this compound as thermomagnetic sensors.

As is known, borides similar to $R_2Fe_{14}B$ easily absorb gaseous hydrogen at room temperature and atmospheric pressure [3]. The introduction of hydrogen into the crystal lattice of $Er_2Fe_{14}B$ considerably changes both the Curie temperature and the temperature T_{SR} of the spin-reorientation phase transition. An observation of the nonmonotonic hydrogen-content dependence of T_{SR} in polycrystalline $Er_2Fe_{14}BH_x$ samples has been reported [4]. However, our investigations [5] carried out with both single crystalline and polycrystalline $Nd_2Fe_{14}BH_x$ samples show that the data for the latter samples should be significantly corrected in order to reveal the "true" effect of hydrogenation on the magnetocrystalline anisotropy and spin-reorientation phase transition. Thus, the use of high-purity single crystal samples in investigations is of fundamental importance for determining the temperatures of the spin-reorientation phase transition and analyzing anomalies in the magnetic properties near T_{SR}.

The aim of this work is to study the effect of the absorbed hydrogen content on the temperatures of magnetic phase transitions in $Er_2Fe_{14}BH_x$ single crystals. The dependences found in this study can be used to develop new magnetic materials with preset properties.

The $Er_2Fe_{14}B$ compound was synthesized by melting in an arc furnace with a non-consumable tungsten electrode on a water-cooled copper bottom in an atmosphere of purified helium. High-purity erbium (99.96 wt %) obtained by double vacuum sublimation [6], Armco iron, and foundry Fe–B alloy were used as initial components. The uniformity of the composition of the compound was ensured by multiple melting and subsequent homogenization annealing in evacuated quartz ampoules at a temperature of 700°C for 200 h. Crystal blocks in which the disorientation of crystal axes did not exceed 10° were prepared from the resulting ingots. The $Er_2Fe_{14}B$ compound was hydrogenized by hydrogen that had escaped in the decomposition of titanium dihydride TiH_2. We obtained $Er_2Fe_{14}BH_x$ hydrides with x = 0.4, 1.2, 1.5, 2, and 2.5. After hydrogenation, the block crystal structure did not break. The temperature dependence of magnetization was analyzed on a pendulum magnetometer in a magnetic field of H = 500 Oe in the temperature interval 150–700 K.

It has been found that the strongest change resulting from the introduction of hydrogen into the crystal lattice of $Er_2Fe_{14}B$ is that of the magnetic ordering temperature, which was determined as the temperature of the sharpest drop in the magnetization $\sigma(T)$ in the transition from the ferromagnetic state to the paramagnetic one. Figure 1 shows the Curie temperature as a function of the absorbed hydrogen content for $Er_2Fe_{14}BH_x$ compounds. These compounds can be treated as two-lattice (REM and iron sublattices) ferrimagnets. For comparison, $T_C(x)$ for the isostructural compound with lutetium, which is a nonmagnetic REM, is also shown in Fig. 1. As is seen in the figure, the introduction of

[1] *Baĭkov Institute of Metallurgy and Material Science, Russian Academy of Sciences, Leninskiĭ pr. 49, Moscow, 119991 Russia*

* *e-mail: teresh@ultrs.imet.ac.ru*

[2] *Moscow State University, Vorob'evy gory, Moscow, 119992 Russia*

[3] *Institute of Low Temperatures and Structural Research, Polish Academy of Sciences, ul. Okolna 2, Wroclaw, 50-950 Poland*

1028-3358/05/5007-0346$26.00

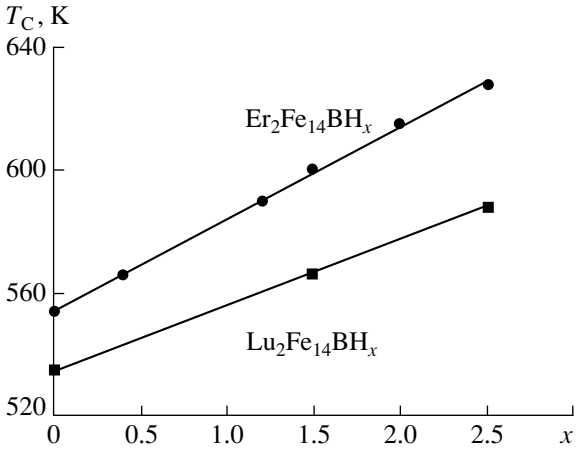

Fig. 1. Curie temperature vs. the absorbed hydrogen content for the $Er_2Fe_{14}BH_x$ and $Lu_2Fe_{14}BH_x$ compounds.

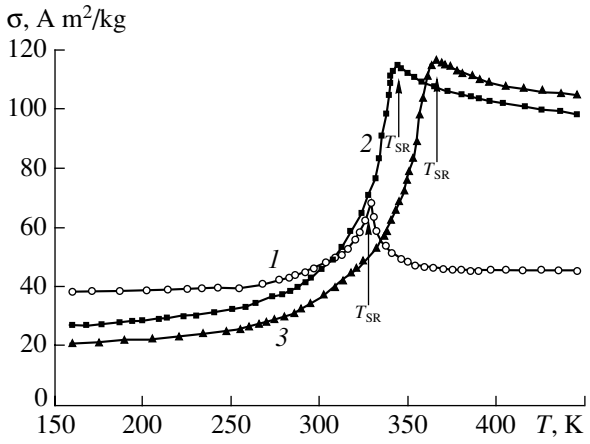

Fig. 2. Temperature dependence of magnetization $\sigma(T)$ measured in the external magnetic field H = 500 Oe for the $Er_2Fe_{14}BH_x$ compounds with x = (*1*) 0, (*2*) 1.5, and (*3*) 2.5.

hydrogen into the crystal lattice of the $Er_2Fe_{14}B$ and $Lu_2Fe_{14}BH_x$ compounds leads to a monotonic increase in the Curie temperature T_C by an average of 25 K per hydrogen atom.

Figure 2 shows the temperature dependences of magnetization $\sigma(T)$ measured for $Er_2Fe_{14}BH_x$ compounds in the temperature interval 150–450 K and in the magnetic field applied along the texture axis. As is seen in Fig. 2, a pronounced peak is observed on the $\sigma(T)$ curve for the initial $Er_2Fe_{14}B$ compound at T = 327 K, which corresponds to the spin-reorientation temperature. Hydrogenation slightly changes the character of the $\sigma(T)$ dependences: the sharp peak becomes a step (which probably indicates a change in the transition character), and the temperature of the spin-reorientation phase transition, which is determined as the temperature at which $\sigma(T)$ is maximal, is shifted towards higher temperatures.

Figure 3 shows (*1*) the temperature of the spin-reorientation phase transition as a function of absorbed hydrogen content as compared to (*2*) the available reference data [4]. As is seen in Fig. 3, the $T_{SR}(x)$ dependence is nonlinear in both cases. However, our investigations show that the introduction of hydrogen atoms into the crystal lattice of the $Er_2Fe_{14}B$ compound increases the temperature of the spin-reorientation phase transition (except for the case x = 0.4 the spin-reorientation phase transition in which, as well as in the initial sample, is observed near $T_{SR} \approx 327$ K); whereas, according to data from [4], the spin-reorientation temperature T_{SR} decreases in the content range $0 \le x \le 1.7$ and increases only for $x > 1.7$. As was mentioned above, such a difference in the behaviors appears because the spin-reorientation temperature T_{SR} was measured in [4] for polycrystal samples. The crystal axes of grains in polycrystal samples have different orientations with respect to the applied magnetic field. In the magnetic field applied along the easy magnetization axis, the spin-reorientation phase transition (its character and transition temperature) differs from that observed when the magnetic field is applied along the hard magnetization axis. For this reason, spin-reorientation phase transitions that occur in different grains of a polycrystal sample are superimposed, which leads to a nonmonotonic $T_{SR}(x)$ dependence.

Both the REM and iron sublattices contribute to the magnetic anisotropy of the $R_2Fe_{14}B$ compounds. The contribution from the iron sublattice to the magnetocrystalline anisotropy is determined by empirically analyzing the anisotropy of compounds with Lu or Y. The

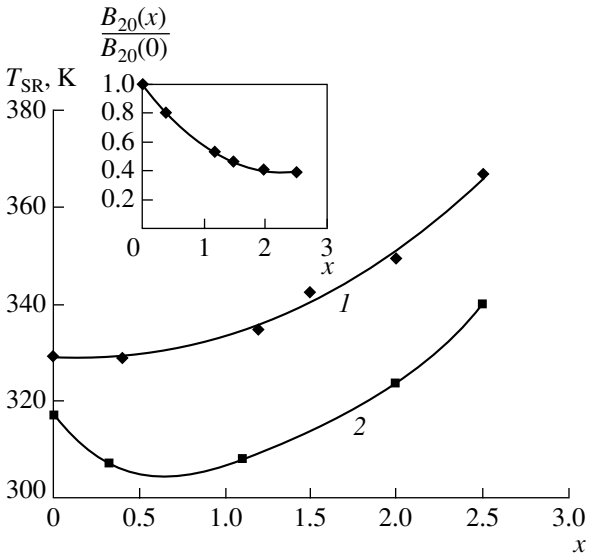

Fig. 3. Hydrogen-content dependence of the spin-reorientation temperature for the $Er_2Fe_{14}BH_x$ compounds according to (*1*) our measurements and (*2*) data taken from [4]. Inset: the hydrogen-content dependence of the crystal field parameter $B_{20}(x)$ (divided by B_{20} at x = 0) for the $Er_2Fe_{14}BH_x$ compounds.

REM and iron sublattices make the main contribution to the magnetocrystalline anisotropy for low and high temperatures, respectively. The competition between the contributions from the REM and 3*d* sublattices to the magnetocrystalline anisotropy of the $Er_2Fe_{14}B$ compound leads to their compensation at the temperature T_{SR} at which the spin-reorientation phase transition occurs. It is a first order phase transition that is accompanied by the step reorientation of the easy magnetization axis from the basal plane in the direction of the *c* axis for $T > T_{SR}$.

In order to separate the contributions from the Fe and REM sublattices to the magnetocrystalline anisotropy, we previously analyzed the effect of hydrogenation on the magnetocrystalline anisotropy of the $Lu_2Fe_{14}B$ compound [7]. It has been found that the hydrogenation of this compound reduces the magnetic anisotropy constant K_{1Fe} (by 10%, on average, after the introduction of one hydrogen atom per formula unit at $T = 4.2$ K). Using the known values of the temperature T_{SR} for the $Er_2Fe_{14}BH_x$ compounds and the magnetic anisotropy constant K_{1Fe}, one can determine the change in the crystalline field B_{20} after the introduction of hydrogen atoms into the crystal lattice by the formula [4]

$$B_{20} = \frac{20K_{1Fe}}{J(J+1)(2J-1)(2J+3)}\left(\frac{k_B T_{SR}}{\Delta_{ex}}\right)^2. \quad (1)$$

Here, Δ_{ex} is the exchange splitting between the two nearest energy levels in the exchange field B_{ex}, k_B is the Boltzmann constant, and $J = \frac{15}{2}$ is the total angular momentum of the Er^{3+} ions. We calculated the exchange field B_{ex} and exchange splitting Δ_{ex} using data on the Curie temperatures of the $Lu_2Fe_{14}BH_x$ and $Er_2Fe_{14}BH_x$ compounds within the framework of the molecular field theory [8]. It has been found that hydrogenation enhances both the exchange field acting inside the iron sublattice and the exchange field of the iron sublattice acting on the REM sublattice.

The inset in Fig. 3 shows the concentration dependence of the critical field parameter B_{20} calculated by Eq. (1) and divided by B_{20} at $x = 0$ for the $Er_2Fe_{14}BH_x$ compound. It is seen that the parameter B_{20} decreases as the hydrogen content increases. Since the basic contribution to the magnetocrystalline anisotropy constant K_{1R} of the REM sublattice for this class of compounds comes from the crystal field parameter B_{20}, hydrogenation significantly reduces K_{1R} (e.g., the introduction of 2.5 hydrogen atoms per formula unit into the crystal lattice of the compound reduces K_{1R} by 60% at $T = 4.2$ K). Therefore, a decrease in T_{SR} would be expected due to the weakening of the magnetocrystalline anisotropy of the erbium sublattice. Nevertheless, T_{SR} increases due to the enhancement of the Fe–Fe and R–Fe exchange interactions, which leads to a considerable change in the temperature dependence of the magnetic anisotropy constants $K_{1R}(T)$ and $K_{1Fe}(T)$ in the hydrogenized $Er_2Fe_{14}BH_x$ compounds.

Thus, investigations performed with single crystal $Er_2Fe_{14}B$ samples prepared from high-purity initial components provided more accurate data on the basic magnetic characteristics of this material (Curie temperature and temperature of the spin-reorientation phase transition). The subsequent controlled introduction of hydrogen enabled us to reveal the laws of change in these magnetic characteristics; namely, their monotonic increase with the hydrogen content was found. Knowledge of the true dependences $T_C(x)$ and $T_{SR}(x)$ for $Er_2Fe_{14}BH_x$ single crystals that are undistorted by impurities and defects makes it possible to achieve both purposeful changes in these characteristics and the production of materials with preset properties.

ACKNOWLEDGMENTS

We are grateful to Prof. S.A. Nikitin for detailed discussions of the results. This work was supported by the Russian Foundation for Basic Research (project no. 04-03-32194) and the Department of Chemistry and Materials Science, Russian Academy of Sciences (program no. 8).

REFERENCES

1. J. F. Herbst, Rev. Mod. Phys. **63**, 819 (1991).
2. P. Wolfers, M. Bacmann, and D. Fruchart, J. Alloys Compd. **317–318**, 39 (2001).
3. A. V. Andreev, A. V. Deryagin, N. V. Kudrevatykh, *et al.*, Zh. Éksp. Teor. Fiz. **90**, 1024 (1986).
4. M. D. Kuz'min, L. M. Garcia, I. Plaza, *et al.*, J. Magn. Magn. Mater. **146**, 77 (1995).
5. S. A. Nikitin, I. S. Tereshina, N. Yu. Pankratov, *et al.*, Phys. Status Solidi A **196** (1), 317 (2003).
6. O. D. Chistyakov, G. S. Burkhanov, N. B. Kol'chugina, and N. N. Panov, Vysokochist. Veshchestva, No. 3, 57 (1994).
7. I. S. Terechina, A. V. Andreev, H. Drulis, and E. A. Tereshina, in *Proceedings of International Symposium on Metal-Hydrogen Systems: Fundamentals and Applications, Krakow, Poland, 2004* (Krakow, 2004), p. 156.
8. S. A. Nikitin and I. S. Tereshina, Fiz. Tverd. Tela (St. Petersburg) **45**, 1850 (2003) [Phys. Solid State **45**, 1944 (2003)].

Translated by R. Tyapaev

Doklady Physics, Vol. 50, No. 7, 2005, pp. 349–350. Translated from Doklady Akademii Nauk, Vol. 403, No. 2, 2005, pp. 187–188.

TECHNICAL PHYSICS

Microwave Fracturing and Grinding of Solid Rocks by Example of Kimberlite

Corresponding Member of the RAS A. N. Didenko, B. V. Zverev, and A. V. Prokopenko

Received February 7, 2005

The problem of achieving fracture in rocks has always been and remains of crucial importance. Recently, along with conventional methods of fracture, novel approaches based on various physical phenomena have been used. We refer here to electric (electric-discharge, electrostriction, and piezoelectric) methods, magnetic (magnetostriction) methods, electromagnetic (laser) methods, sonic (shock-plastic) methods, beam (electron, proton, and plasma) methods, and thermal-shock methods of fracture. The common feature of all these methods is that, as a result of the action on a substance, stresses exceeding the rupture stress arise in the material. For the majority of rocks, such stresses attain several units or even tens of MPa. However, many of the above-listed methods either can only be employed for fracturing materials of a certain class, or else display low efficiency. From this standpoint, thermal-shock fracture methods are apparently rather attractive. At the same time, their potentialities are limited by the difficulties involved in rapidly heating rocks over a large depth, which is associated with their low heat conductivity.

The method of thermal-shock fracture, which is based on heating samples by powerful microwave radiation, seems to be the most promising. We now consider this problem in more detail.

Fracture caused by the action of thermal shock can occur for two reasons.

The first is the rapid evaporation of water contained in rock pores when the saturated-vapor pressure in hollows filled with water comes to exceed the rupture stress P [1].

The second reason is the linear expansion of solids in the process of heating, so that arising stresses attain the rupture stress, i.e., $\alpha\Delta T = \frac{P}{E}$. Here, α is the linear-expansion coefficient, ΔT is the temperature variation under heating, and E is the Young's modulus [2]. It is evident that this effect is manifested especially clearly for rocks having a high linear-expansion coefficient and low Young's modulus.

At Moscow State Mining University, a vast number of investigations into the loss of strength by rocks based on the employment of the microwave energy were carried out [3]. Unfortunately, the microwave-power density was low in these studies. Therefore, the heating of samples was slow, so that the most interesting features of the process escaped observation. All these studies were performed with iron ores and ferrous quartzites that exhibited noticeable inhomogeneities and possessed a large number of cracks along interfaces. In addition, the authors of [3], strictly speaking, investigated not the fracture of rocks under the action of microwave energy, but the effect of a preliminary microwave irradiation on the results of subsequent grinding and mesh analysis. From this standpoint, it is of interest to study the possibility of the fracture (but not the loss of strength) of hard homogeneous rocks under their rapid heating. Kimberlite was chosen as an example of such a rock because it possesses a high hardness and has great practical importance insofar as it is a unique root rock that contains diamonds.

As is well known from [4], kimberlite is an ultrabasic brecciated rock of magmatic origin and corresponds to the carbonate–serpentine rock type. Unaltered nonserpentinous kimberlite rocks consist of 50% or more olivine. As the basic rock-forming mineral for deep xenolites, olivine is not only the basic fraction of kimberlite but is also found as one of the most propagated inclusions in such protomaterials as granite, picroilmenite, etc., that are contained in kimberlites. However, unaltered kimberlites are rather rare, due to the fact that their intense transformations occur under the action of hydrothermal processes. Usually, kimberlite is a rock of kimberlite–serpentine composition with negligible amounts of olivine, pyroxenes, granite, ilmenite, phlogopite, apatite, magnetite, perovskite, chromspinelite, and other minerals. In other words, kimberlite is a combination of a number of various dielectrics: calcium carbonates, calcium silicates, and oxides of iron, aluminum, magnesium, chromium, titanium, and of other metals. Bound water is contained only in phlogopite in which its fraction attains 10%.

Moscow Engineering Physics Institute (State University), Kashirskoe sh. 31, Moscow, 115409 Russia
e-mail: didenko@dimus.mephi.ru; prok@dimus.mephi.ru

1028-3358/05/5007-0349$26.00

Thus, water does not affect the fracture of kimberlite because the content of phlogopite in it is not high.

Our experiments were carried out with kimberlite samples taken from different diamond deposits, namely, two in Yakutia and one near Arkhangelsk. Continuous frequency-range magnetrons with a power of 0.6 and 5 kW and operating at a frequency $f = 2.45$ GHz were used as a microwave-radiation source. In order to elevate the microwave-energy density, we used the resonator-type rather than waveguide-type microwave systems. This has allowed us to considerably reduce the time of heating samples. As a heating chamber for kimberlite, we used a cylindrical resonator with H_{111}-type oscillations and a capacity-terminated cylindrical E_{010}-type resonator. The copper-made resonators had high intrinsic Q factors. They were supplied with ceramic channels for introducing and removing the substance under study. For the stable operation of the magnetron generator with the resonator termination, we applied the same resonator load as in the magnetron-frequency stabilization system.

As a preliminary, we determined the dielectric characteristics of a sample. The measurements were performed by the comparative resonance method in the reference E_{010} resonator. It was determined that the permittivity $\varepsilon = 6$ and $\tan\delta = 0.026$, where δ is the loss angle. For different samples, the measurement accuracy was about 20%. These results testify to the fact that kimberlite belongs to a class of imperfect dielectrics, and its skin-layer depth attains $\delta = \dfrac{\lambda}{\pi\sqrt{\varepsilon_1}\tan\delta} \approx 60$ cm. Thus, we can expect that the bulk heating of a sample will occur, and, therefore, we can introduce a sample of a size 3–4 cm^3 into the cylindrical H_{111} resonator. The coefficient of the microwave-power transfer to a kimberlite sample in the case of positioning it in the electric-field maximum attains approximately 95%. This makes it possible to heat a kimberlite sample for several seconds at a microwave power of 0.6 kW up to temperatures of several hundreds of degrees Celsius.

The heating process had been accompanied by a series of explosions, as a result of which the samples were dispersed. It was found that Arkhangelsk kimberlites were grinded sufficiently well. At the same time, Yakutian kimberlites were split into 2–4 pieces. This can be explained by the fact that the latter samples had a higher hardness than the former (the hardness was 7–8 in the Moos scale) and, probably, possessed a large viscosity [5], which resulted in damping mechanical shifts caused by heating and prohibited stresses exceeding the rupture stress. Insofar as in ambient air diamonds begin to burn at a temperature of 850°C, it does not seem reasonable to heat kimberlite up to temperatures exceeding (300–400)°C. The experiments performed have shown that stresses arising as a result of heating are lesser than the rupture stress. Thus, we can fracture and grind a kimberlite sample only by the evaporation of water contained in pores. Unfortunately, it is difficult to realize this process because the fraction of water in solid rocks is usually low, decreasing even further with time. Therefore, for fracturing kimberlite, we have used the vapor-bath method. Holding kimberlite samples for 1.5 h in a vapor bath significantly improved the situation. After the microwave irradiation, an Arkhangelsk kimberlite sample held in water vapor was easily dispersed into small pieces. After self-grinding in a centrifuge, these pieces could be transformed into rough sand. It was more difficult to fracture Yakutian kimberlites. However, it was possible to obtain 2–4-mm pieces from them after the microwave irradiation in the resonator, which is sufficient for extracting diamonds from kimberlite. The situation can be simplified provided that the newly-extracted kimberlite contains about 5% water.

Thus, the studies carried out have shown that rapid microwave heating combined with the preliminary holding of kimberlite in a vapor bath makes it possible to fracture and grind an arbitrary solid rock. However, from an economic point of view, the developed fracture method yields its undoubted advantages only in the case that a diamond-containing rock such as kimberlite is being treated. The method is especially promising in combination with the preliminary enrichment of kimberlite or in the case of the development of small-scale setups for performing rapid analysis. The fact that the linear-expansion coefficient of diamond is lower than that for kimberlite by approximately one order of magnitude allows us to avoid unfavorable scenarios at the initial heating stage. The use of methods that eliminate the mechanical fracturing and grinding of kimberlite makes it possible to extract diamonds without any changes in their original shape, which significantly increases their value.

REFERENCES

1. A. N. Didenko, *Microwave Energetics: Theory and Practice* (Nauka, Moscow, 2003) [in Russian].
2. A. N. Didenko, Dokl. Akad. Nauk **331**, 571 (1993) [Phys. Dokl. **38**, 344 (1993)].
3. V. M. Petrov, Radioélectron. Telekommun., No. 4 (2002).
4. S. I. Kostrovskiĭ, *Geochemical Features of Kimberlite Minerals* (Nauka, Novosibirsk, 1986) [in Russian].
5. L. D. Landau and E. M. Lifshitz, *Theory of Elasticity* (Nauka, Moscow, 1986; Pergamon, Oxford, 1986).

Translated by G. Merzon

Doklady Physics, Vol. 50, No. 7, 2005, pp. 351–354. Translated from Doklady Akademii Nauk, Vol. 403, No. 2, 2005, pp. 189–192.

TECHNICAL PHYSICS

Behavior of the System of Diamond Particles with Nanometer Nickel Coating at High Pressures and Temperatures in the Sintering Process

E. A. Ekimov[1], A. S. Ivanov[2], A. F. Pal'[3], A. N. Ryabinkin[3,*], A. O. Serov[3], A. N. Starostin[2], Academician V. E. Fortov[4], R. A. Sadykov[5], N. N. Mel'nik[5], and A. Presh[6]

Received January 21, 2005

Diamond powders are usually sintered at temperatures of 1500–2200°C and pressures of 6–8 GPa. Such additions as Co and Ni, which are catalysts for the transformation of graphite into diamond at high pressures, promote the recrystallization of carbon through the liquid phase, resulting in the formation of diamond–diamond contacts, under conditions in which the sintering temperature is not optimal for diffusion processes or for plastic deformation in the diamond itself [1, 2]. It is known that the physical properties of sintered diamond depend substantially on the activator concentration, because the area of diamond–diamond contacts in the diamond matrix decreases as this concentration increases. The production of sufficiently hard and strong diamond compact materials at a pressure of 7.7 GPa and a temperature of 2000°C without the introduction of additions or with its concentration, i.e., cobalt, lower than the critical concentration of 5 vol %, appeared to be impossible even in the absence of nondiamond carbon in the final sintered product [1]. Experimental data on the sintering of diamond with low contents of activators and binders are scarce due primarily to the problem of the homogeneous introduction of additives to the diamond powder. The application of new procedures, which ensure the deposition of nanometer layers of an additive on particles of the diamond powder and solve the problem of the inhomogeneity of the initial mixture, may allow for the production of diamond ceramic with a diamond content of 95 vol % with high mechanical and chemical properties. The problem of the sintering of diamond with small amounts of an activator deposited on diamond as nanometer layers is nontrivial and requires that preliminary investigations of the behavior of the diamond–additive system be conducted at high pressures and temperatures.

In this work, we analyze the physicochemical processes that occur at high pressures in the system of diamond particles with sizes 3–5 μm and activator concentrations of about 1–2 vol %, which is deposited in the form of nanometer layers on diamond particles in a plasma [3]. Nickel is used as the activator, because the resulting compact materials are expected to be applied to produce a high-pressure diamond chamber for neutron diffraction studies under pressure (the neutron absorption in Ni is one-eighth of that in Co [4]).

Using a special disposition of the electrodes of a radio frequency discharge, we create a region in which it is possible to confine a cloud of suspended micron particles, i.e., a plasma–dust trap. The trap is filled with the dust component by means of the inertial dispersion device. Metallic nickel is deposited on suspended diamond particles by means of an ion–plasma spraying system of the magnetron type. According to spectral analysis, the diamond powder with coating contains, in addition to carbon, 2.5 wt % Ni, 0.3 wt % Fe, 0.018 wt % Cr, 0.05 wt % Si, 0.07 wt % Cu, 0.05 wt % Mn, 0.03 wt % Al, and 0.03 wt % B. Scanning electron microscopy of the nickel-coating surface shows that an increase in the thickness of the coating from 10 to 100 nm can be accompanied by the formation of a "fibrous" structure. Grains or fibers with a diameter of about 10–20 nm are observed in electron-microscopy

[1] *Vereshchagin Institute of High-Pressure Physics, Russian Academy of Sciences, Troitsk, Moscow oblast, 142190 Russia*

[2] *Russian Research Center Kurchatov Institute, pl. Akademika Kurchatova 1, Moscow, 123182 Russia*

[3] *Skobel'tsyn Institute of Nuclear Physics, Moscow State University, Vorob'evy gory, Moscow, 119899 Russia*

* *e-mail: aserov@mics.msu.su*

[4] *Institute of Problems of Chemical Physics, Russian Academy of Sciences, Chernogolovka, Moscow oblast, 142432 Russia*

[5] *Lebedev Physical Institute, Russian Academy of Sciences, Leninskiĭ pr. 53, Moscow, 117924 Russia*

[6] *High Pressure Research Center, Polish Academy of Sciences, Warsaw, Poland*

1028-3358/05/5007-0351$26.00

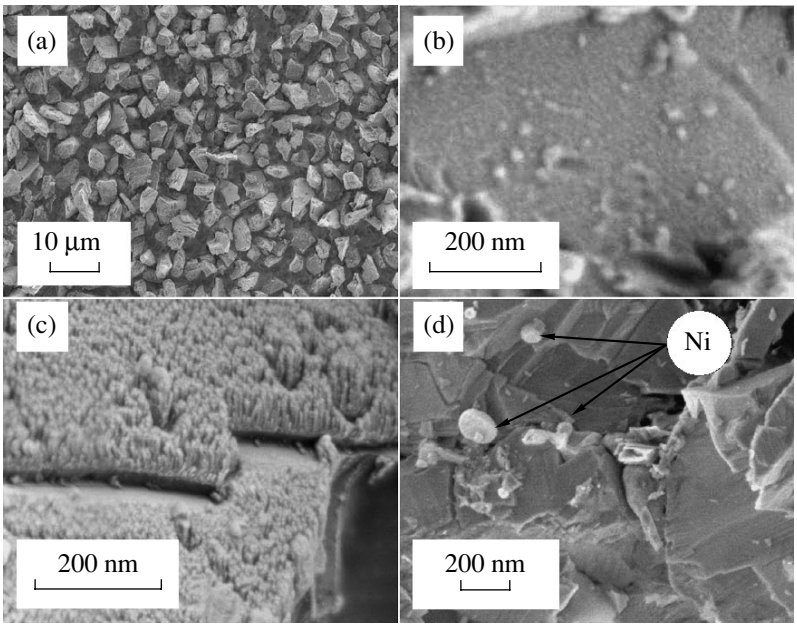

Fig. 1. Microphotographs of samples: (a) nickel-coated diamond particles, (b) 10-nm nickel coating on a diamond particle, (c) 100-nm nickel coating on a diamond surface, and (d) microstructure of the break of the sintered compact material near the grain joint; nickel particles are marked.

pictures. This formation occurs when the pressure of a plasma-forming gas, argon, increases from 0.18 to 0.7 Pa. Owing to a decrease in the thermalization length of the nickel atomic flow, a supersaturated nickel vapor is formed and condensed, and clusters appear. Figure 1 shows the characteristic morphology of the "thin" and "thick" nickel coatings on diamond powders.

The experiments are carried out with powders with thin coating whose thickness is equal to about 10 nm, as determined by transmission electron microscopy. Diamond is sintered in a high-pressure chamber of the toroid type [5] at a pressure of 8–9 GPa. The process of sintering diamond is studied by analyzing the effect of power supplied to a heater (temperature) on the phase content and structure of samples. X-ray analysis is carried out by means of a GADDS (BRUKER AXS) diffractometer. Raman scattering in samples is studied by means of a U-1000 Jobin–Yvon spectrometer. Laser radiation with a wavelength of 488 nm is focused onto a spot with a diameter of about 20 μm.

Figures 2 and 3 show the data of the x-ray phase analysis and Raman spectroscopy of samples of the initial material and sintering-produced compact materials. The sintering duration for samples corresponding to the data presented in the figures was equal to 30 s, with the exception of samples that were sintered at a temperature of 2400°C. At this temperature, samples were sintered for 2–3 and 5–6 s in order to exclude the effect of the transformation of the graphite heater into diamond, which proceeds very intensely for given parameters in the zone of contact between graphite and the container.

Analysis of the above data shows that the initial diamond powder is not graphitized during the deposition of nickel coating; i.e., the transformation of diamond into sp^2 hybridized carbon is not observed. Sintering of diamond at 800–1000°C is accompanied by the forma-

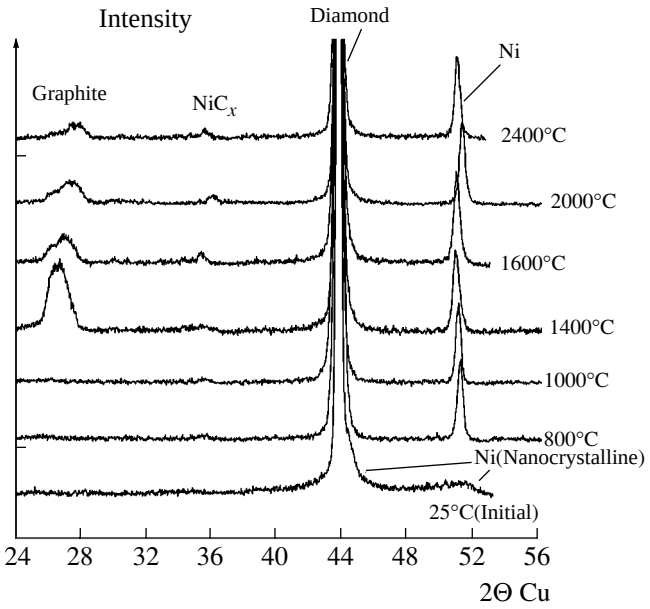

Fig. 2. Results of x-ray phase analysis of samples before and after the sintering process at a pressure of 8–9 GPa.

tion of disordered sp^2 hybridized carbon, whose presence is revealed only in Raman spectra. At a temperature of 1400°C, the formation of graphite-like carbon is observed (Fig. 2), which is revealed in samples by x-ray phase analysis. As is known, the pressure-induced graphitization of diamond proceeds near pores, where the pressure is much lower than the mean value. The temperature of the onset of the formation of graphite-like carbon is close to the temperature of the graphite–nickel eutectic (~1300°C), which indicates the presence of processes of the solution of diamond carbon in a nickel melt and its liberation in the graphite form. We emphasize that the initial stage of diamond graphitization, which is revealed by Raman spectroscopy but not by x-ray phase analysis, is also observed near 800°C in the diamond powder at a pressure of 2 GPa in the absence of additions [6]. One feature of graphite-like carbon that is formed at temperatures above 1400°C is its presence in the form of two phases with various interlayer distances d_{002}. Omitting details, we note that the hypothesis of compressed graphite [7] does not explain the appearance of sp^2 graphite with two dedicated interplanar distances and a regular decrease in the interplanar distances occurring alongside an increase in the treatment temperature. A possible hypothesis is that an intermediate graphite-like carbon structure with sp^2–sp^3 bonds and an interplanar distance smaller than that of graphite is formed in the graphite–diamond transformation process. The fraction of graphite-like carbon in diamond compact materials is more than halved as the sintering temperature increases from 1400 to 2400°C. A decrease in the fraction of nondiamond carbon in compact materials with an increase in temperature can be caused by the inverse catalytic transformation of the graphite-like phase compressed in pores into diamond. We note that samples sintered at 2400°C for 2–3 and 5–6 s have the same ratio of the intensities of x-ray peaks for graphite-like carbon and diamond, which indicates the filling of pores with graphite-like carbon in 2–3 s at 2400°C in the presence of nickel. As temperature in the experiment varies, the position of the diffraction peak near $2\Theta \sim 36°$ varies regularly along with the nickel lines on x-ray patterns with respect to the diamond diffraction lines. Taking into account the observed behavior, we attribute the appearance of this peak ($2\Theta \sim 36°$) to the presence of the metastable phase of the content NiC_x that is formed in the nickel matrix in the form of thin assemblies of (220) planes. The Raman spectra of samples change substantially as the sintering temperature increases. Only lines corresponding to sp^2 carbon are observed in samples for sintering temperatures above 1000°C, and considerable luminescence with a peak near 1300–1400 cm^{-1} is observed in the spectra for sintering temperatures above 1400°C. Such a change in the Raman spectra of sintered diamond samples can be explained by the dominant role of

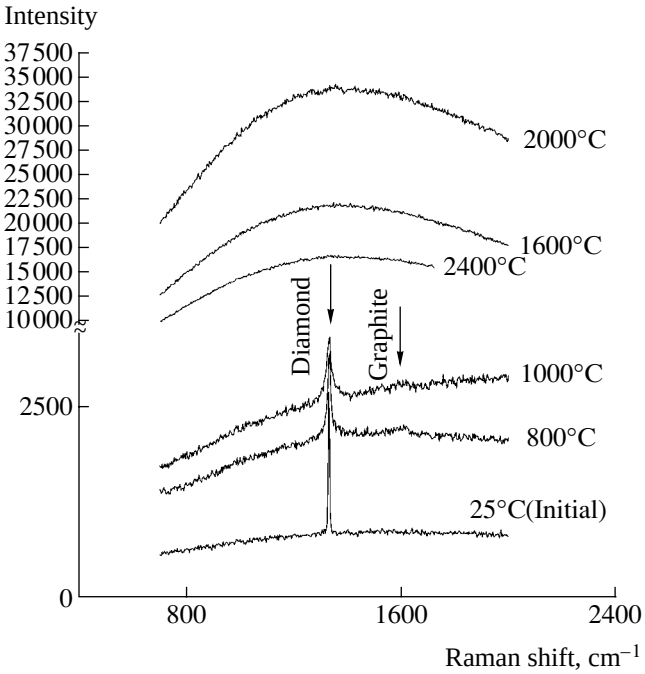

Fig. 3. Evolution of Raman spectra of samples with increasing sintering temperature.

luminescence of a phase that is formed at temperatures above 1400°C on the basis of both sp^2–sp^3 carbon and plastically deformed diamond [8]. As follows from analysis of x-ray patterns (Fig. 2) and electron microscopic studies (Fig. 1d) of samples, nanosize nickel deposited on the surface of diamond particles is recrystallized in the process of thermobaric treatment, resulting in the formation of particles smaller than 200 nm that are uniformly distributed over the volume of the diamond compact material. We attribute the formation of spherical nickel particles to the tendency to the reduction of surface energy that is displayed by the system at all stages in the formation of the microstructure of the compact material.

Thus, 10-nm nickel coating has been deposited on diamond particles without the formation of sp^2 carbon in the final product by means of plasma–dust technology. During the sintering process of the composite powder under pressure, the recrystallization of nickel is observed over the entire temperature range under investigation. The graphitization of diamond in pores of the diamond compact material begins with the formation of disordered sp^2 carbon at temperatures below 800°C, whereas the graphite-like structure of nondiamond carbon is formed at temperatures above 1400°C. It has been found that the fraction of nondiamond carbon in diamond compact materials decreases and the fraction of graphite-like carbon with a low interplanar distance increases correspondingly as the treatment temperature increases to 2400°C.

REFERENCES

1. M. Akaishi, S. Yamaoka, J. Tanaka, *et al.*, J. Am. Ceram. Soc. **70**, 237 (1987).
2. H. Yu, S. Li, and E. Hu, Diamond Relat. Mater. **3**, 222 (1994).
3. A. S. Ivanov, V. S. Mitin, A. F. Pal', *et al.*, Dokl. Akad. Nauk **395** (3), 335 (2004) [Dokl. Phys. **49**, 163 (2004)].
4. *The Special Feature Section of Neutron Scattering Lengths and Cross Sections of the Elements and Their Isotopes*; Neutron News **3** (3), 29 (1992).
5. L. G. Khvostantsev, L. F. Vereshchagin, and A. P. Novikov, High Temp.-High Press. **9**, 637 (1977).
6. J. Qian, C. Pantea, G. Voronin, and T. W. Zerda, J. Appl. Phys. **90**, 1632 (2001).
7. V. D. Andreev, Yu. I. Sozin, and É. S. Simkin, Sverkhtverd. Mater. **2**, 13 (1990).
8. V. A. Karavanskiĭ, N. N. Mel'nik, and T. N. Zavaritskaya, Pis'ma Zh. Éksp. Teor. Fiz. **74**, 204 (2001) [JETP Lett. **74**, 186 (2001)].

Translated by R. Tyapaev

Doklady Physics, Vol. 50, No. 7, 2005, pp. 355–359. Translated from Doklady Akademii Nauk, Vol. 403, No. 2, 2005, pp. 193–197.

TECHNICAL PHYSICS

A Method for Processing Sounding Signals on the Basis of Atomic Functions

V. F. Kravchenko[1], D. V. Smirnov[2], and Corresponding Member of the RAS I. B. Fedorov[2]

Received March 24, 2005

INTRODUCTION

The wide application of digital methods for the formation and processing of radar signals has stimulated the development of problems associated with the synthesis and analysis of discretely coded signals. In order to increase the reliability of extracting weak signals against the background of intense noise, sounding signals of a complicated shape are employed. In this case, to satisfy the requirements of modern radar stations they should possess uncertainty functions of a certain form and provide a low level of side lobes, as well as a high resolution with respect to both the time delay and frequency of signals [1]. To ensure the necessary design requirements for radar stations, the method of weight processing is widely exploited. The theory of atomic functions [2–6], which is applied for the first time in solving the formulated problem, represents one promising method in this direction.

CONSTRUCTING THE UNCERTAINTY FUNCTION

Narrow-band signals conventionally used in radar applications can be represented in the form

$$u(t) = U_{m0}(t)\exp[j(\omega_0 t + j\varphi(t))] = U_m(t)\exp(j\omega_0 t), \quad (1)$$

where $U_m(t) = U_{m0}(t)\exp[j\varphi(t)]$ is the complex-valued modulating function, otherwise known as the complex signal envelope, which is determined by the form and parameters of the modulation, and ω_0 is the mean value of the sounding-signal frequency. For the signal $u(t)$, the two-dimensional correlation function is given by the correlation integral

$$R_m(\tau, \Omega) = \int_{-\infty}^{\infty} U_m(t)U_m^*(t+\tau)\exp(-j\Omega t)dt. \quad (2)$$

The modulus of the normalized two-dimensional correlation function acting as the uncertainty function for a sounding signal is denoted as $\chi(\tau, \Omega) = |\rho(\tau, \Omega)|$, where $\rho(\tau, \Omega)$ is the normalized two-dimensional correlation function. This function is widely used in the analysis of sounding-signal properties. In the case of optimal processing, the relief of the uncertainty function for a sounding signal makes it possible to estimate the features of the signal. For example, the sharpness of the basic maximum testifies to the possibility of the precise measurement of the distance (t_R) and velocity (V_r) or of the resolution in the case of observing closely located goals. The existence of additional relief maxima of the uncertainty function of a sounding signal indicates the possible ambiguity of measurement results or the masking of a weak reflected signal by side lobes of the uncertainty function of an intense signal.

DISCRETELY CODED SIGNALS

Discretely coded signals can be written out in an analytical form as

$$U_{mi} = \begin{cases} \sum_{i=1}^{N} a_i U_{mi}(t)\exp[j((f_0 + f_i)t + \varphi_i)] \\ \text{for } 0 \le t \le T_s, \\ 0 \text{ for other values of } t. \end{cases} \quad (3)$$

Here, a_i, f_i, and φ_i are the code-modulation parameters for the sequence $\{\tau_i\}$ of discrete elements τ_i, which can contain codes $\{a_i, f_i, \varphi_i\}$; $i = 1, 2, \ldots, N$ is the ordering number of a discrete element of the code sequence; N is

[1] *Institute of Radio Engineering and Electronics, Russian Academy of Sciences, ul. Mokhovaya 18, Moscow, 103907 Russia e-mail: kvf@pochta.ru*

[2] *Bauman Moscow State Technical University, Vtoraya Baumanskaya ul. 5, Moscow, 107005 Russia e-mail: smirnov.d@gmail.com*

1028-3358/05/5007-0355$26.00

the number of discrete elements in the signal under consideration; $U_{mi}(t)$ is the standard-amplitude pulse of a duration τ_k (duration of a code element) so that

$$U_{mi}(t) = \begin{cases} U_{mi}[t-(i-1)\tau_k] \text{ for } (i-1)\tau_k \le t \le i\tau_k, \\ 0 \text{ for other values of } t. \end{cases} \quad (4)$$

In this case, the signal duration is $T_s = N\tau_k$. The complex envelope of a complicated signal discretely coded over frequency can be represented in the form

$$U(t) = \begin{cases} \sum_{n=0}^{N-1} A_n \text{rect}(t-nT)\exp[j\times 2\pi f_n(t-nT) + j\varphi_n], \\ 0 \le t \le (N-1)T, \\ 0, \quad t > (N-1)T. \end{cases} \quad (5)$$

Here, A_n is the amplitude of a partial rectangular pulse, φ_n is the signal initial phase, f_n is the frequency-time code given as a numerical sequence N_{f_n} of N nonrecurrent integers, $f_n = N'_{f_n}\Delta f$, $N'_{f_n} = N_{f_n} - 1$, and N is the code dimension. The uncertainty function of a signal is the modulus of its self-correlation integral

$$|\chi(\tau,\Omega)| = \frac{1}{2E}\left|\int_{-\infty}^{\infty} U^*(t)U(t-\tau)\exp(j\times 2\pi\Omega t)dt\right|, \quad (6)$$

where E is the signal total energy. Assuming that the initial phase φ_n is zero, we arrive at the relationship

$$U(t) = \begin{cases} \sum_{n=0}^{N-1} A_n \text{rect}(t-nT)\exp[j\cdot 2\pi f_n(t-nT)], \\ 0 \le t \le (N-1)T, \\ 0, \quad t > (N-1)T. \end{cases} \quad (7)$$

Performing certain mathematical transformations of phase multipliers, we then obtain the complete expression for the uncertainty function of a signal discretely coded over frequency

$$|\chi(\tau,\Omega)| = Z\left|(1-\tau')\sum_{n=0}^{N-k-1}\chi_1(\tau,\Omega) + \tau'\sum_{n=0}^{N-k-2}\chi_2(\tau,\Omega)\right|, \quad (8)$$

where

$$\chi_1(\tau,\Omega) = A_nA_{n+k}\frac{\sin(\pi\alpha(1-\tau'))}{\pi\alpha(1-\tau')} \times \exp\{j\pi[\alpha(2n+2k+1+\tau') - 2N'_{f_n}\tau']\},$$

$$\chi_2(\tau,\Omega) = A_nA_{n+k}\frac{\sin(\pi\beta\tau')}{\pi\beta\tau'} \times \exp\{j\pi[\beta(2n+2k+2+\tau') - 2N'_{f_n}\tau']\},$$

$$\alpha = N'_{f_n} - N'_{f_{n+k}} + \nu, \quad \beta = N'_{f_n} - N'_{f_{n+k+1}} + \nu,$$

$$Z = \left(\sum_{n=0}^{N-1} A_n^2\right)^{-1},$$

$$\tau' = \frac{\delta}{T}, \quad \nu = \frac{\Omega}{\Delta f}, \quad \Delta f T = 1, \quad \tau = kT + \delta,$$

$$0 \le \delta \le T, \quad k = 0, 1, \ldots, N-1.$$

Thus, the features of the uncertainty function of an amplitude-weighted signal discretely coded over frequency are determined by two data bases, namely, those of the frequency-code N_{f_n} and weight A_n. The algorithm for obtaining $[A_n]$ consists in the partitioning of the segment $x = [-1, 1]$ into $N-1$ elementary intervals $\Delta x = x_{i+1} - x_i = \frac{2}{N-1}$. The values of the weight function at the ends of the interval are weights of discrete components $A_n = W(x_n)$ for a signal discretely coded over frequency, where $x_n = -1 + N'_{f_n}\Delta x$. For a periodic phase-manipulated signal $(0, \pi)$, the two-dimensional correlated function at times that are multiples of the elementary-pulse duration is

$$\rho(\tau, f) = \left[\left(\frac{1}{N}\sum_{n=1}^{N}\theta_n\theta_{n+k}\cos(2\pi nf\Delta T)\right)^2 + \left(\frac{1}{N}\sum_{n=1}^{N}\theta_n\theta_{n+k}\sin(2\pi nf\Delta T)\right)^2\right]\frac{\sin^2(M\pi f T_M)}{M^2\sin^2(\pi f T_M)}. \quad (9)$$

Here, τ and f are the deviations of the delay and of the Doppler shift for the reflected signal from the delay and the frequency shift of the reference oscillation, respectively; $\tau = \tau_0 - \tau_i\ (= k\Delta T)$; $f = f_0 - f_k$, θ_n is the elementary pulse with a duration ΔT; T_M is the modulation period; and $M = \frac{\vartheta}{T_M}$ is the number of modulation periods within the range ϑ of the coherent processing. As follows from formula (9), the two-dimensional correlation function for a signal containing M periods is the product of this function $\rho_1(\tau, f)$ for one period of the signal and the periodicity multiplier. The two-dimensional

correlation function for one period of a phase-manipulated signal is of the form

$$\rho_1(k, m) = \left(\frac{1}{N}\sum_{n=1}^{N}\theta_n\theta_{n+k}\cos 2\pi\frac{nm}{NM}\right)^2 + \left(\frac{1}{N}\sum_{n=1}^{N}\theta_n\theta_{n+k}\sin 2\pi\frac{nm}{NM}\right)^2, \quad (10)$$

where $\frac{n}{N}$ is the time-delay detuning expressed in terms of fractions of the period, and $\frac{m}{M}$ is the frequency detuning expressed in fractions of the reciprocal duration of the period.

ANALYSIS OF THE RESULTS OF A NUMERICAL EXPERIMENT

We now consider the application of Kravchenko–Rvachev atomic functions [2–5] as weight functions (windows) in the formation of the vector $[A_n]$. For comparison, we take the cosine function on a pedestal

$$W(x) = p + (1 - p)\cos^n\frac{\pi x}{2}, \quad (11)$$

where the parameter p [6] is chosen to be equal to 0.3, this choice corresponding to the best reduction (–32 dB) of the side-lobe level over time delay. In accordance with [6], the side-lobe level over time delay in the case of the rectangular envelope ($p = 1$) is –14 dB. With the variation of the parameter p from 1 to 0.3, the side-lobe level over frequency increases from –13 to –8 dB. The expansion coefficient $K_p(\tau)$ of the main lobe over time delay is elevated by a factor of 1.9, whereas the expansion coefficient $K_p(\Omega)$ over frequency is constant and equals 1. The dispersion of the signal energy spectrum in the case of a rectangular envelope is $\Delta W^2 = 0$, and the root-mean-square of the signal time duration is $\Delta T^2 = 13.1595$. For the cosine function on a pedestal and $p = 0.3$, the following values were obtained: $\Delta W^2 = 1.8045$ and $\Delta T^2 = 18.3692$.

Example 1. We now analyze the application of the atomic function up(x). The side-lobe levels over time delay and over frequency attain, respectively, –29 dB (which approaches the best result for the cosine function on a pedestal) and –6 dB. The expansion coefficient for the main lobe is $K_p(\tau) = 2.8$, $\Delta W^2 = 4.0892$, and $\Delta T^2 = 2.8936$.

Example 2. Using the atomic function $\mathrm{fup}_n(x)$, we now determine the dependence of the side-lobe level and the expansion coefficient of the main lobe on the parameter n. The best value of the weight function fup(x) for reducing the side-lobe level over the time delay is $n = 10$. The use of the atomic function $\mathrm{fup}_{10}(x)$ to form a weight sequence makes it possible to reduce the side-lobe level to –32 dB. In this case, the first side-lobe level over frequency is elevated by 4 dB and attains –11 dB. At the same time, the resolution of the discretely coded frequency signal over time delay (distance) becomes worse (as compared to an unweighted signal) by a factor of 1.4, whereas it remains invariable over frequency (velocity).

Example 3. We now determine the dependences of the side-lobe level and the expansion coefficient for the main lobe on the parameter a of the atomic function $h_a(x)$. With a rise in the parameter a, the weight function approaches a rectangular function, which allows us to find the optimal relation for the side-lobe level over time delay, frequency, and resolution. For example, employing the function $h_{2.1}(x)$ makes it possible to lower the side-lobe level to –22.5 dB, the side-lobe level over frequency being –9.5 dB, and the resolution over time delay becoming worse by a factor of 1.37.

Example 4. We study here the weight function (window) of the parabolic shape

$$W_1(x) = 1 - (1 - \Delta)2t^2 \quad \text{for} \quad \Delta = 0.5.$$

The side-lobe level over time delay attains –32 dB. This result can be compared with physical parameters of the cosine function on a pedestal and with the atomic function $\mathrm{fup}_{10}(x)$. In the given case, the side-lobe level over frequency is –7.1 dB, and the resolution with respect to time delay for a signal discretely coded over frequency becomes worse by a factor of 2.1. The dispersion of the signal energy spectrum in the case of a rectangular envelope is $\Delta W^2 = 2.5$, and the root-mean-square value for the signal time duration is $\Delta T^2 = 5.6398$. In the figure, the cross sections of the uncertainty function in the case of a signal discretely coded over frequency for optimal weight functions (windows) of the rectangular, cosine, as well as the Kravchenko–Rvachev [$\mathrm{fup}_{10}(x)$ and [$h_{2.1}(x)$] functions, are presented. As follows from Table 1, in the case of the employment of the $\mathrm{fup}_n(x)$ Kravchenko–Rvachev atomic function, the dispersion of the energy spectrum is lower by a factor of approximately 8–9 than the analogous physical characteristics in the case of the cosine function on a pedestal. The root-mean-square of the signal time duration also differs by a factor of 1.9 from the same physical characteristics for the weight functions in the case of the cosine function on a pedestal. The spectral characteristics of the $h_a(x)$ Kravchenko–Rvachev function vary in the following manner: for this atomic function, the dispersion of the energy spectrum is higher by a factor of 2.2. However, for the root-mean-square characteristics of the signal time duration, its value is smaller by a factor of approximately 5.5 than that in the case of the cosine function on a pedestal.

Example 5. We now analyze the processing of a phase-manipulated signal. To this end, we estimate the

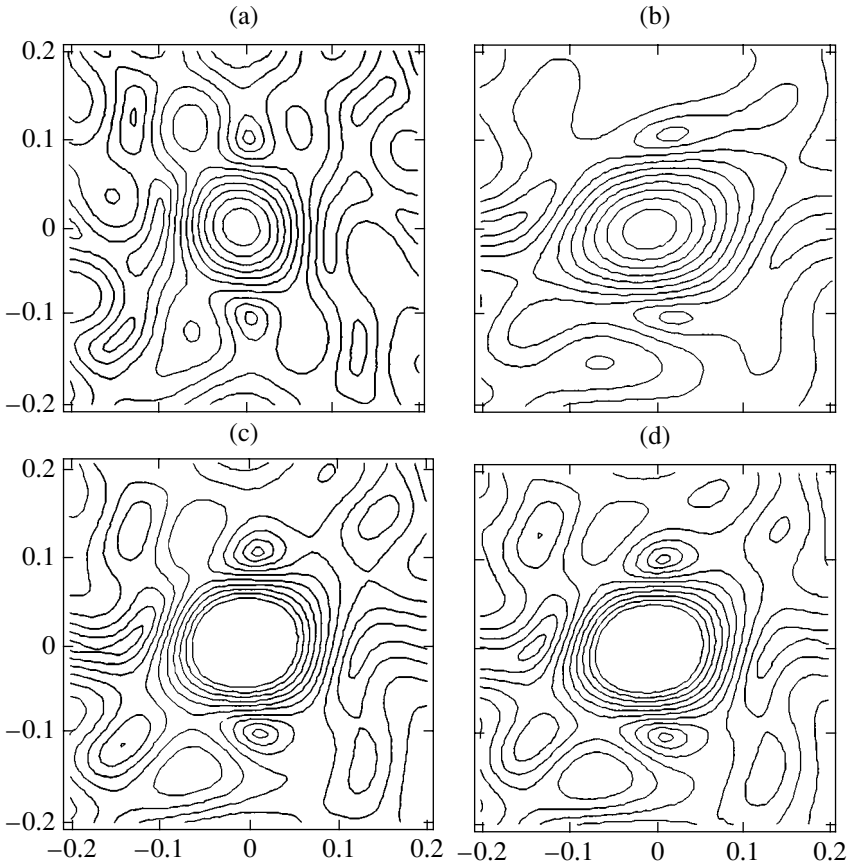

Fig. 1. Cross sections of the uncertainty function in the [τ, Ω] plane for the envelope: (a) of rectangular shape; (b) of cosine shape; (c) in the form of the Kravchenko–Rvachev function $\mathrm{fup}_{10}(x)$; and (d) in the form of the Kravchenko–Rvachev function $h_{2.1}(x)$.

side-lobe level in the case of a nonzero detuning over frequency and among *M*-sequences of the same length $N = 127$. This ensures the necessary bandwidth at a given resolution. The minimum of the sum of side lobes over power can serve as a quality criterion. The values of the sequence terms were calculated according to the recurrence formula

$$q_n = k_1 q_{n-1} + k_2 q_{n-2} + \ldots + k_7 q_{n-7}$$

(summation over modulus 2).

For each sequence, we found the phase-manipulated signal corresponding to one period $\theta_n = (-1)^{q_n}$. We consider the *M* sequence 3 for which the coefficients equal 0, 0, 0, 0, 0, 1, 1. From the standpoint of code formation, this sequence is the simplest (only one summation over modulus 2 is required) but has a high side-lobe level. We study a two-dimensional correlation function of form (9) for a standard phase-manipulated signal. In the basic cross section (for $k = 0$), the function has the

Table 1. Values of the first side-lobe level and of the expansion coefficient $K_p(\tau)$ for the optimal weight functions (windows)

Form of the envelope	Side-lobe level over τ, dB	Side-lobe level over Ω, dB	ΔW^2	ΔT^2	$K_p(\tau)$
$p + (1-p)\cos^n\frac{\pi x}{2}$, $p = 0.3$	–32	–8	1.8045	18.3692	1.9000
$1 - (1-\Delta)2t^2$, $\Delta = 0.5$	–32	–7.1	2.5000	5.6398	2.0710
$\mathrm{up}(x)$	–29	–6	4.0892	2.8936	2.8000
$\mathrm{fup}_n(x)$ for $n = 10$	–32	–10.4	0.2600	9.9839	1.3450
$h_a(x)$ for $a = 2.1$	–22	–9.34	3.9020	3.1509	1.3750

Table 2. Values of the first side-lobe level and of the expansion coefficient $K_p(\tau)$ for the optimal weight functions (windows)

Weight function	Side-lobe level	K_{av}	K_p
–	0.0305	0.0078	1.0000
$H(x)$ for $p = 0.1$	0.0063	0.0042	1.4250
$W_1(x)$ for $\Delta = 0.5$	0.0058	0.0043	1.4417
$\mathrm{fup}_n(x)$ for $n = 3$	0.0052	0.0042	1.3725
$h_a(x)$ for $a = 2.1$	0.0137	0.0063	1.1325

form $\frac{\sin^2 x}{x^2}$. In side lobes (for $k = 0$), this function increases from $\frac{1}{127^2}$ and attains its maximum between $m = 10$ and $m = 20$; it further oscillates about the value of $\frac{1}{127}$. The curves converge to the value of 0.0078 at $m = 20$. Their monotonic increase between $m = 0$ and $m = 10$ is violated only for low lobes. Therefore, the relative lobe size is characterized by the values in one cross section of the time axis, e.g., for $m = 10$. A high value of the side-lobe level, equal to 0.0305, is observed for $k = 7$. For weight functions constructed on the basis of atomic functions the characteristics of a phase-manipulated signal are shown in Table 2. In the case of using the weight function (window) in the form

$$W_1(x) = 1 - (1 - \Delta) \times 2t^2 \, (\Delta = 0.5),$$

we obtain that the maximum value of a side lobe is 0.0058. It is worth comparing this result with the numerical data obtained for the atomic function $\mathrm{fup}_n(x)$ and uncertainty function $H(x)$. The mean value near which all the curves oscillate is also comparable with the above-listed functions. However, an expansion of the main lobe by a factor of 1.4417 takes place.

CONCLUSIONS

The calculation results obtained for the uncertainty function of discretely coded signals at zero Doppler shift of the frequency and zero time-delay in the case of different physical parameters of Kravchenko–Rvachev weight functions were analyzed. The analysis has shown that a significant decrease occurs in the side-lobe level for the uncertainty function at a high resolution over both time delay and frequency. This approach makes it possible to elevate the reliability of detecting weak signals against the background of intense noise and demonstrates the efficiency of the novel-class weight functions in problems associated with the processing of sounding signals.

REFERENCES

1. V. K. Sloka, *Problems of Radar-Signal Processing* (Sovetskoe Radio, Moscow, 1970) [in Russian].
2. V. F. Kravchenko, *Lectures on Theory of Atomic Functions and Their Certain Applications* (Radiotekhnika, Moscow, 2003) [in Russian].
3. V. F. Kravchenko and M. A. Basarab, *Boolean Algebra and Approximation Methods in Boundary Value Problems of Electrodynamics* (Fizmatlit, Moscow, 2004) [in Russian].
4. Yu. V. Gulyaev, V. F. Kravchenko, and D. V. Smirnov, Usp. Sovrem. Radio Élektron., No. 8, 3 (2003).
5. V. F. Kravchenko and V. I. Pustovoĭt, Dokl. Akad. Nauk **386**, 38 (2002) [Dokl. Phys. **47**, 672 (2002)].
6. V. Ya. Plenkin and Tkhan Khyng Nguen, Izv. Vyssh. Uchebn. Zaved., Ser. Radio Élektron. **47** (1), 3 (2004).

Translated by G. Merzon

Doklady Physics, Vol. 50, No. 7, 2005, pp. 360–365. Translated from Doklady Akademii Nauk, Vol. 403, No. 3, 2005, pp. 328–333.

TECHNICAL PHYSICS

Mesosubstructure in Surface Layers of Cyclically Loaded Polycrystals and Its Role in Fatigue Failure

Academician V. E. Panin, T. F. Elsukova*, A. V. Panin, and O. Yu. Kuzina

Received March 14, 2005

1. According to the main concept of physical mesomechanics, a deformable solid is a multilevel system in which a plastic flow is self-consistently developed at the micro-, meso-, and macro-levels [1]. Its surface layer is an autonomous mesoscopic level of structural deformation, where mesoscopic mechanisms of the plastic flow develop much more freely than in the material bulk [2]. The motion of dislocations at the microlevel plays a decisive role in the active loading of polycrystals at room temperature. All processes at mesoscopic structural levels are developed self-consistently with the dislocation deformation at the microlevel. This circumstance hinders the development and manifestation of these mechanisms at mesolevels.

The intense development of mesoscopic deformation mechanisms in the surface layers can be expected in cyclically loaded polycrystals below the macroscopic yield point. The specificity of the crystal structure of a weakened surface layer [2, 3] is responsible for the plastic flow in this layer when the material bulk is loaded yet below the yield point [4]. The surface–bulk matching causes the surface corrugation effect, resulting in the appearance of stress concentrators in the regions of the local curvature of the corrugation [5]. The relaxation of these stress concentrators through the generation of dislocations in an elastically deformed substrate is hindered. For this reason, an increase in the number N of loading cycles necessarily leads to the continuous growth of the stress concentrators in the surface layer. As a consequence, the excess of deformation defects in surface layers increases continuously, exceeding their density in the material bulk by one or two orders of magnitude [6, 7]. Owing to this behavior, deformation mesolevels are involved in the plastic flow.

The character and kinetics of the development of mesoscopic levels of structural deformation necessarily depend on the structure-phase state of the surface layer, the degree of grain-boundary sliding in this layer, and the shear stability level of its crystal lattice and of the whole internal structure. In this work, the role of mesoscopic mechanisms of cyclic deformation in the surface layers of polycrystals with the strongly varied parameters listed above in presence of fatigue failure is analyzed.

2. We have studied polycrystals of titanium, aluminum, and lead and its alloys. They have strongly different homological temperatures. Aluminum and lead are monomorphic metals with the same (fcc) crystal lattice. A fundamental difference between these polycrystals is that of the shear-stability degrees of their internal structures. The shear stability of the internal structure of a polycrystal is qualitatively expressed in values of its shear modulus G, stacking fault energy γ [8, 9] (see table), and grain-boundary sliding degree.

Lead has comparatively low G and γ values, while grain boundary sliding is easily developed in this polycrystal at 20°C [10]. These properties indicate that the shear stability of the internal structure of lead is low. Aluminum has high shear stability, which is manifested in high G and γ values (see table) and in the absence of grain boundary sliding at 20°C [11]. Titanium has a very high melting temperature and very low stacking fault energy. It qualitatively differs from lead and aluminum in the crystal lattice type (α-Ti has a hexagonal close packed lattice) and by its manifestation of polymorphism.

Flat samples have the shape of a dumbbell with a $40 \times 8 \times 1$ mm working part. Since loading is performed by alternating bending, only the surface layers of a sample are primarily deformed. Tests are carried out in the multicycle fatigue regime. Fatigue is quantitatively characterized by the number of cycles to failure N_f. Extended patterns of the deformation of the surface layer at the mesolevel are obtained by scanning the optical images of the deformed-sample surface.

3. Based on the theory of a vortex mechanical field in a deformed solid [13], in [12] a synergetic criterion of plasticity was formulated as the equality of the curls

Institute of Strength Physics and Materials Science, Siberian Division, Russian Academy of Sciences, Akademicheskiĭ pr. 2/1, Tomsk, 634021 Russia

** e-mail: kolgay@yandex.ru*

1028-3358/05/5007-0360$26.00

The composition and parameters of the materials under investigation: the homological test temperature T_{test}/T_{melt}, the shear modulus G, the stacking fault energy γ, the bending amplitude A, the number N_f of the loading cycles to failure, and the mean diameter d of the elements of the mesosubstructure II

Composition, wt %	T_{test}/T_{melt}, K	G, GPa	γ, mJ/m^2	A, mm	$N_f \times 10^{-6}$	d, mm
Pb	0.5	5.6	50	0.5	0.15	0.5
Pb–1.9 Sn	0.5	–	–	0.5	0.07	1.0
Pb–0.03 Te	0.5	–	–	0.5	0.75	0.38
Al A6	0.3	24.5	200–280	1.0	7.6	0.2
Ti BT1-0	0.2	39.4	10	2.5	does not break at $N = 16.7 \times 10^6$	0.05

of the primary sliding and accommodation secondary flows of all types of deformation defects:

$$\operatorname{curl} S^{\alpha\mu} = V(\operatorname{curl} R^{\alpha})^{\mu}, \quad (1)$$

where $V = \dfrac{d\varepsilon}{dt}$ is the complete deformation rate. Equation (1) physically means that, in a material under deformation, there is a volume at which the total curl of the flows of deformation defects is equal to zero:

$$\sum_{k=1}^{N} \operatorname{curl} J_k = 0, \quad (2)$$

where J_k is the deformation defect flow at the kth structural level. The linear size l of this volume characterizes the upper structural deformation level that must be included in the description of the solid under deformation in the multilevel formulation. In order to satisfy condition (2), a mesosubstructure whose scale is determined by the parameter l must be formed in the deformed material. The self-consistent deformation of a mesovolume at scale l is accommodated by its fragmentation at lower mesolevels.

Structural investigations have completely corroborated this statement. It has been shown that a disoriented mesosubstructure II (according to the classification given in [1]), where the parameter l may vary between the mean size of grains and the sample width, is formed on the sample surface in dependence on the shear stability of the internal structure of the polycrystal subjected to alternating bending. The character and scale of the mesosubstructure II determines the fatigue failure of the polycrystal. Let us discuss the results for the materials under consideration.

Lead and its alloys. The development of deformation at the mesolevel is most pronounced in pure lead, because the shear stability of its internal structure is low and the homological temperature of the test is high. This development is manifested in the formation of the large-block mesosubstructure II (see Fig. 1a). The mechanism of its formation is based on a single sliding in grains that is accompanied by their material rotation as a whole. This rotation initiates intense grain boundary sliding at the grain boundary. In Fig. 1a, such grain boundary sliding is clearly seen at the *AB* boundary of grains *1* and *2* by the break of special marks at the place of their intersection with the boundary. The constrained character of grain boundary sliding is responsible for the appearance of a stress mesoconcentrator at the point of bending of the boundary (point *C*). As the number of loading cycles increases, a disclination is formed at this region of the local bending of the grain boundary; this disclination initiates the propagation of localized translational–rotational deformation in grain *1* in the direction of maximum tangential stresses (τ_{max}) of the mesoband *CDE*. As the number of loading cycles increases, the length of the mesoband increases proportionally to the sliding degree along the boundary *AB*. This behavior indicates that the source *C* of localized deformation is continuously fed by grain-boundary flows of deformation defects and, hence, by the primary sliding flows. In other words, intragrain translational flows generate particular disclinations as accommodation rotational deformation modes.

For lead as a shear-unstable material, the development of numerous localized-deformation mesobands is typical, which propagate in the conjugate directions τ_{max} through many grains. The self-organization of these bands leads to the formation of the block mesosubstructure II, each element of which includes several initial grains of the polycrystal. When this process ends over the entire width of the sample, accommodation processes are further developed via an increase in the rotations of the material inside the mesobands under consideration. This development gradually leads to the nucleation and propagation of fatigue cracks in these mesobands, and this process ends with the failure of the sample over the boundaries of blocks at a comparatively small number of loading cycles (see table).

Special doping of lead with tellurium, which forms a chemical compound with the former, results in an increase in the shear stability and suppression of grain boundary sliding. As a result, instead of the block mesosubstructure II, a similar substructure is formed in

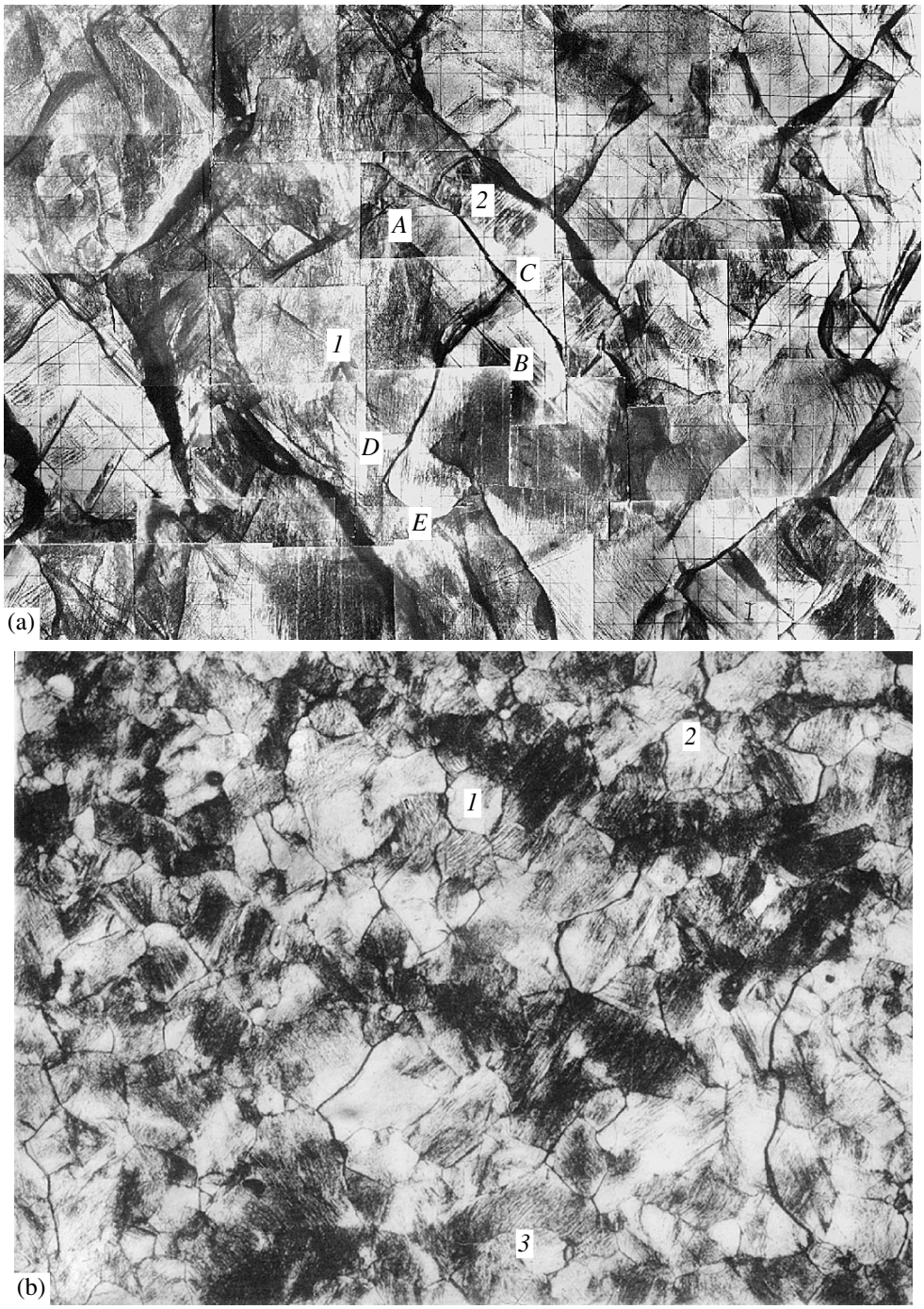

Fig. 1. (a) Surface mesosubstructure II: blocks in lead for $N = 7.5 \times 10^4$ cycles as shown with a magnification of 30× and (b) loop conglomerates in Pb–Te alloy for $N = 6.5 \times 10^4$ cycles as shown with a magnification of 100x; the digits indicate the central parts of the conglomerates.

the Pb–Te alloy in the form of loops of self-consistently deformed grains (see Fig. 1b). Such a doping of lead results in a several-fold increase in the number of cycles to failure (see table). In contrast, the doping of lead with a eutectic tin addition, which decreases the atomic bonding forces in the crystal, reduces the shear stability of the internal structure of the polycrystal. This reduction is accompanied by a significant decrease in the number of cycles to failure.

The size distribution of cracks at various fatigue stages is analyzed for lead and its alloys. Change in the strength σ_b is investigated as a function of the number of cycles N of the preliminary alternating bending. As is seen in Fig. 2, the first stage of the cyclic loading is

accompanied by a monotonic decrease in σ_b, which ends with a sharp drop in the material strength at $N \sim 90\% N_f$. The instant of the transition to the sharp drop of σ_b is associated with the completion of the formation of the mesosubstructure II over the entire width of the sample. This experimental observation conclusively indicates that the character and rate of the development of the mesosubstructure II in the surface layer of the cyclically loaded polycrystal are important criteria for estimating its fatigue strength and number of cycles to failure.

Aluminum. The high shear stability of the internal structure of aluminum is characterized by high stability under cyclic loading: for doubled bending amplitude, it is by one and a half orders of magnitude higher than the value for lead (see table). Intragrain deformation in aluminum also occurs via a single sliding, which is accompanied by the material rotation of grains. As a result of the matching of adjacent strongly deformed grains, long-range stress mesoconcentrators arise at their boundaries. The interaction between these mesoconcentrators in the complete absence of grain boundary sliding leads to the step-by-step self-consistent arrangement of active adjacent grains to deformation loop conglomerates that form the mesosubstructure II. In terms of the character and sizes of elements of this substructure, aluminum is similar to the Pb–Te alloy. However, their formation in aluminum requires many more loading cycles.

A typical example of such a substructure at the late fatigue stage is shown in Fig. 3. In this figure, the very strong localization that is a feature of the cyclic deformation is manifested. Some strongly deformed adjacent grains are arranged step-by-step in closed loop conglomerates according to Eq. (2). Their central parts are slightly deformed grains marked by digits.

As conglomerates of self-consistently deformed grains are formed, the role of the structural deformation element gradually passes from the initial grains of the polycrystal to large-scale elements of the mesosubstructure II. A sharp increase in the size of the structural deformation elements is naturally accompanied by a considerable increase in the stress-mesoconcentrator level at their boundaries. The relaxation of these stresses first occurs due to the fragmentation of the material inside the deformation conglomerates of grains. When the possibility of fragmentation as a rotation-type accommodation process is exhausted, the rotational relaxation mechanism of crack formation is manifested. This mechanism ends with the fatigue failure of aluminum at a comparatively large number of loading cycles.

Commercial titanium. Analysis of the titanium surface mesosubstructure that is formed during alternating bending reveals the anomalously low shear stability of the internal structure of its surface layer. This low stability is manifested in the formation of a multi-

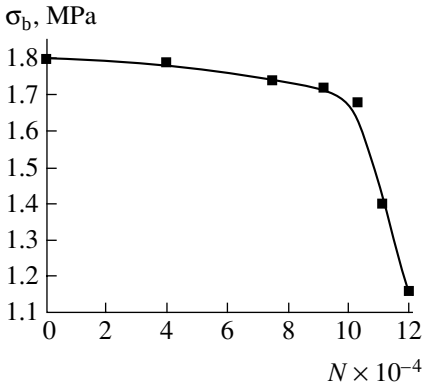

Fig. 2. Breaking stress σ_b of lead vs. the number N of cycles of preliminary alternating bending.

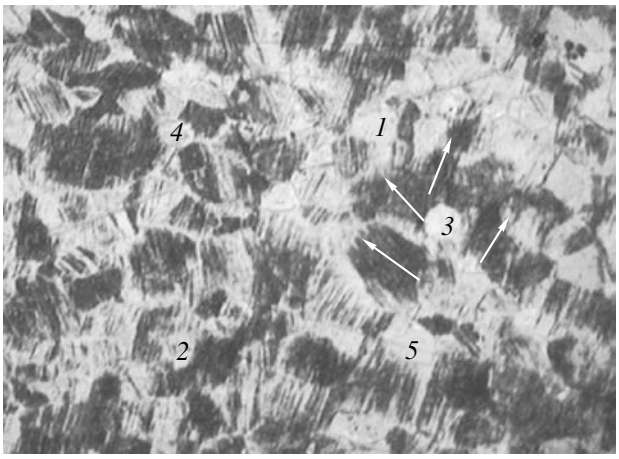

Fig. 3. Mesosubstructure II on the aluminum surface for $N = 5 \times 10^6$ cycles as shown with a magnification of 100×. The digits indicate the centers of the conglomerates of self-consistently deformed grains. The arrows show the shear direction in conglomerate grains.

level mesosubstructure on the surface of recrystallized titanium: the formation of a surface corrugation, motion of grains as a whole system with anomalously developed grain boundary sliding at room temperature, the self-organization of extruded grains in loop conglomerates at the centers of which the intrusion of grains is developed (see Fig. 4). The size of such loops is 40–60 μm, which is equal to 1/4 and 1/10 of their diameter in aluminum and Pb–Te alloy, respectively. The shear moduli of these materials are in the same inverse relation. This correlation is not surprising, because the formation of the mesosubstructure in the form of loops is associated with the matching of plastically deformed surface grains with the elastically loaded substrate. This matching determines the satisfaction of condition (2).

The deformation profile determined by a nanoprofilometer for the titanium sample surface after

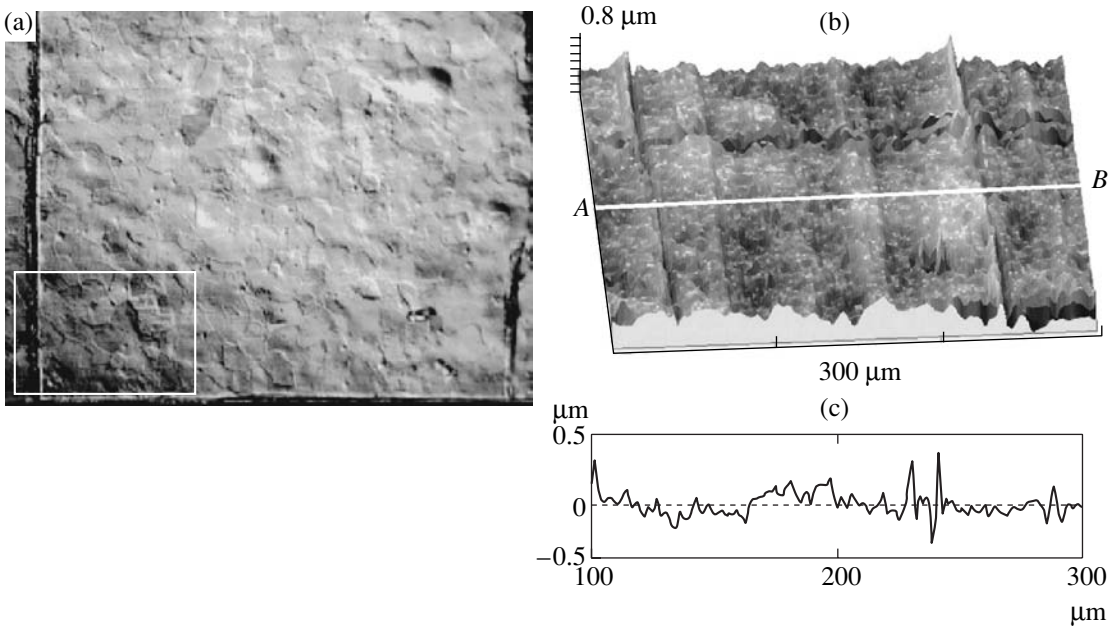

Fig. 4. (a) Surface mesosubstructure II: commercial titanium for $N = 15 \times 10^6$ cycles as shown with a magnification of 350×, (b) surface morphology, and (c) surface profile pattern in the *AB* section.

15×10^6 loading cycles is a corrugation with a wavelength of about 150 μm and a height of 0.4 μm. The surface corrugation effect ensures the high degree of the reversible inelastic deformation of the sample subjected to alternating bending. All these properties provide for a very large number of cycles to failure for titanium. This number for titanium subjected to bending with even much larger amplitude is several times larger than that for aluminum (see table). This property is also ensured by the strong bonding forces in the crystal lattice of titanium.

4. The formation of the mesosubstructure in the surface layers of polycrystals has the above properties exclusively because the "surface layer–substrate" system is multilevel. When these polycrystals are subjected to alternating bending below the yield point, considerable residual strain is accumulated in the surface layer. The matching of the plastically deformed surface layer with the elastically stressed substrate naturally leads to the appearance of a residual surface corrugation. Thus, when a polycrystal is subjected to alternating bending below its macroscopic yield point, the virtual "plastically deformed surface layer–elastically deformed substrate" boundary should be brought into consideration.

A complete and adequate theory of such multilevel processes in the surface layers of deformable solids does not exist as of yet. However, the individual mesolevel mechanisms considered above were satisfactorily described in [14].

Rotational deformation modes associated with deformation along a closed contour in the loops of the surface mesosubstructure give rise to the nucleation of fatigue cracks in the inner loop volumes. These modes are also associated with the incompatibility between the turn of the loop of plastically deformed surface grains and the elastically deformed substrate. In view of this circumstance, we note that a close correlation is observed between the size of blocks or loops in the mesosubstructure of the surface layer and the shear modulus of the substrate material. By changing the state of the surface layer, one can significantly vary the scale of the surface mesosubstructure and thereby the number of cycles to failure of the material.

ACKNOWLEDGMENTS

This work was supported by the Russian Foundation for Basic Research (project no. 02-01-01195a) and by the Council of the President of the Russian Federation for Support of Young Russian Scientists and Leading Scientific Schools (project no. NSh-2324.2003.1).

REFERENCES

1. *Physical Mesomechanics and Computer-Aided Design of Materials*, Ed. by V. E. Panin (Nauka, Novosibirsk, 1995), Vol. 1 [in Russian].
2. V. E. Panin, Fiz. Mezomekh. **4** (3), 5 (2001).
3. A. Zangwill, *Physics at Surfaces* (Cambridge Univ. Press, Cambridge, 1988; Mir, Moscow, 1990).
4. V. P. Alekhin, *Physics of Strength and Plasticity of Surface Layers of Materials* (Nauka, Moscow, 1983) [in Russian].

5. V. E. Panin and L. E. Panin, Fiz. Mezomekh. **7** (4), 5 (2004).
6. V. S. Ivanova and V. F. Terent'ev, *Nature of Metal Fatigue* (Metallurgiya, Moscow, 1975) [in Russian].
7. V. F. Terent'ev, *Fatigue of Metallic Materials* (Nauka, Moscow, 2003) [in Russian].
8. *Properties of Metals: A Handbook*, Ed. by G. V. Samsonov (Metallurgiya, Moscow, 1976) [in Russian].
9. *Tables of Physical Data: Reference Book*, Ed. by I. K. Kikoin (Atomizdat, Moscow, 1976) [in Russian].
10. T. F. Elsukova and V. E. Panin, Izv. Akad. Nauk, Metally, No. 2, 73 (1992).
11. V. E. Panin, T. F. Elsukova, and G. V. Angelova, Fiz. Mezomekh. **3** (4), 79 (2000).
12. V. E. Panin, Izv. Vyssh. Uchebn. Zaved. Fiz., No. 2, 4 (1990).
13. V. E. Panin, Yu. V. Grinyaev, V. E. Egorushkin, and I. L. Bukhbinder, Izv. Vyssh. Uchebn. Zaved. Fiz., No. 1, 34 (1987).
14. V. E. Egorushkin, Izv. Vyssh. Uchebn. Zaved. Fiz. **35** (4), 19 (1992).

Translated by R. Tyapaev

Doklady Physics, Vol. 50, No. 7, 2005, pp. 366–370. Translated from Doklady Akademii Nauk, Vol. 403, No. 3, 2005, pp. 334–338.

TECHNICAL PHYSICS

Study of Shock-Wave Scattering by Microscopic Inhomogeneities of a Medium by Example of a Two-Phase Steel Structure

A. É. Kheifets[1], V. I. Zel'dovich[1], N. Yu. Frolova[1], N. P. Purygin[2], and Academician B. V. Litvinov[2]

Received January 18, 2005

The goal of this paper is to study microscopic-scale (0.1–1 μm) features of shock-wave propagation through various materials that are inhomogeneous in their initial state. Modern methods that have been developed for the continuous measurement of both the mechanical stresses and velocity of a substance in shock-wave experiments provide for spatial resolution at a level of 10 μm [1]. In the present study, we propose a new approach to the investigation of microscopic features in the action of shock waves. The essence of this approach consists in the analysis of electron-microscopy patterns for a deformed microstructure of inhomogeneous materials loaded with shock waves. In this case, inhomogeneities existing in the material are used as a natural reference grid, which makes it possible to investigate microscopic features of strain localization with the subsequent reconstruction of shock-wave motion at the microscopic level. The approach used ensures a spatial resolution higher by two orders of magnitude than that attained in applying methods of the direct experimental observation of shock-wave processes.

As an initial material, we employed 40Kh steel consisting of 0.4% carbon and 1.1% chromium in the initial ferrite–perlite state. The perlite components of steel are colonies of alternating parallel plates of ferrite and cementite, which are variously oriented in space. The thicknesses of cementite and ferrite plates were, on average, approximately 20 nm and 130 nm, respectively. The perlite structure entirely corresponded to the goal formulated in the study. Cementite is a brittle and hard perlite component, whereas ferrite is a soft component. Correspondingly, the ferrite strain in shock waves occurs owing to plastic flow, whereas the cementite strain is predominantly realized through brittle fragmentation. The combination of the physical properties and features of the microstructure for the given material makes it possible to use it as a model material, which is promising from the standpoint of the possible generalization of the results obtained to the entire class of solid media with ordered microscopic inhomogeneities.

A 40Kh-steel solid ball-shaped sample 40 mm in diameter was subjected to the action of a quasi-spherical shock wave, with the pressure rise near the focusing center exceeding 200GPa [2–4]. The sample was covered by a 20-mm explosive layer and was placed into a massive metallic case that prevented the fracture of the ball [5]. At the charge surface, there were detonators that made it possible to simultaneously blast the explosive at several initiation points. A converging quasi-spherical shock wave was excited in the sample material, the pressure being increased as the ball center was approached. The outer part of the ball, having preserved the ferrite-perlite structure, was then investigated by the transmission electron-microscopy method. At the microscopic level, the curvature of the shock-wave front, which had been associated with the loading geometry, was insignificant, because the front curvature radius had exceeded by four orders of magnitude the characteristic sizes of the sample domains under study. In these conditions, the wave should be considered as a plane one. At the same time, the loading scheme used has allowed us to obtain a wide-range spatial pressure scan within the same sample. Thus, we have managed to study the domains that are most convenient for the attainment of our goals within the framework of a single experiment.

Figure 1 exhibits a series of electron-microscopy patterns (panorama) of perlite colonies in a 40-Kh-steel sample subjected to shock-wave loading. Changes in the material microstructure (initial stages of spheroidizing cementite and recrystallization processes in ferrite in

[1] *Institute of Metal Physics, Ural Division, Russian Academy of Sciences, ul. S. Kovalevskoĭ 18,Yekaterinburg, GSP-170, 620219 Russia*

e-mail: alex.home@r66.ru; kheifetz@imp.uran.ru

[2] *Russian Federal Nuclear Center VNIITF, Snezhinsk, Chelyabinskaya oblast, 454070 Russia*

1028-3358/05/5007-0366$26.00

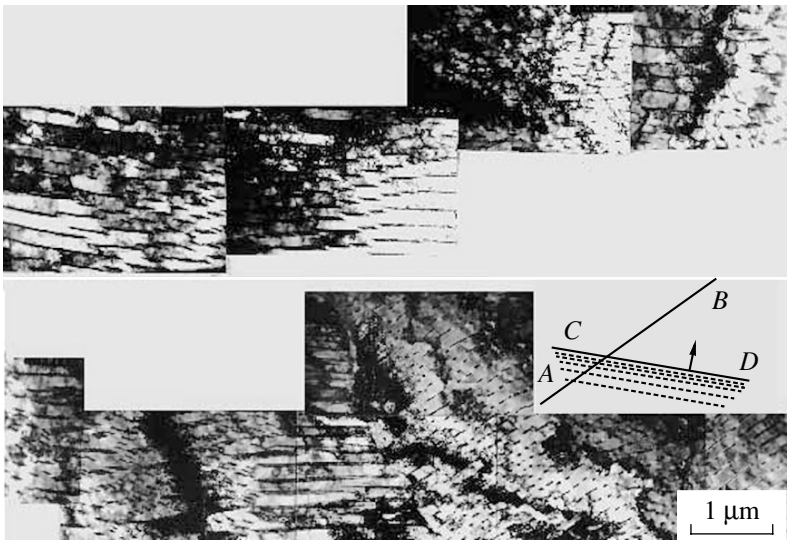

Fig. 1. Microstructure of perlite component in 40Kh steel after shock-wave loading. Line *AB* corresponds to the calculated direction of maximum tangential stresses. Line *CD* denotes the position of the shock-wave front. Traces of spheroidization are observed in cementite plates oriented along the maximum tangential stresses.

the presence of traces of plastic strain) testify to the fact that the residual temperature attained 500–700°C [6]. Correspondingly, the pressure in the shock wave was about 75 GPa [2–4]. The average distance between cementite plates (structure period) in the perlite colonies was ~150 nm.

As is seen from Fig. 1, the cementite plates are shattered. In this case, the displacement directions for separate fragments are easily traced, and initial plate contours can be reconstructed. This makes it possible to consider the initial perlite component of steel as a natural reference grid whose distortions allow us to study the microscopic features of material strain.

For investigating microscopic-strain fluctuations, a computer program package was developed that is capable of digitizing electron-microscopy perlite images with the subsequent statistical and mathematical processing data obtained. An example of a digitized image for a segment of a perlite colony is presented in Fig. 2. The straight segments indicate displacements of cementite plates. The statistical analysis performed for the panorama (Fig. 1) has led to the following results. In the Cartesian coordinate system associated with the microstructure (Fig. 1), the vector $\langle \Delta \boldsymbol{\varepsilon} \rangle$ of the fragment mean displacement is

$$\langle \Delta \boldsymbol{\varepsilon} \rangle = (44 \pm 6, 36 \pm 3) \text{ nm}.$$

In Fig. 1, the direction corresponding to this vector is marked by line *AB*. The standard deviation of the displacements from the mean value is

$$\mathbf{S} = (65, 30) \text{ nm},$$

i.e., the strain essentially fluctuates.[1]

The direction of vector $\langle \Delta \boldsymbol{\varepsilon} \rangle$ coincides with that of the material-shear strain, which corresponds to the maximum tangential stresses in the shock wave. Correspondingly, the shock-wave front is inclined at an angle of 45° to vector $\langle \Delta \boldsymbol{\varepsilon} \rangle$ (Fig. 1). This result is ambiguous insofar as there exist two equivalent positions of the shock wave with respect to vector $\langle \Delta \boldsymbol{\varepsilon} \rangle$. However, the values of strain fluctuations in various directions must be different because the loading is anisotropic: there exists a preferred direction along which the shock wave propagates. Therefore, the orientation of the front with respect to the deformed microstructure (Fig. 1) can be determined by the other independent method based on the differences (associated with the anisotropy of the loading) in the projections of the displacement vector onto various directions. This allows us, first of all, to find which of the two equivalent positions of the shock-wave front with respect to vector $\langle \Delta \boldsymbol{\varepsilon} \rangle$ is realized. Second, it is necessary to verify the accuracy of the proposed method for analysis of the deformed microstructure. The coincidence of the results obtained by the two independent methods confirms the accuracy of the results.

The displacements of cementite-plate fragments describe the strain corresponding to the inhomogeneity of the mass velocity in the shock wave. Along the direction perpendicular to the shock-wave front, the mass-

[1] Nevertheless, the error $\boldsymbol{\delta}_{\langle \Delta \boldsymbol{\varepsilon} \rangle}$ in the determination of the quantity $\langle \Delta \boldsymbol{\varepsilon} \rangle$ is small. For the given number $N = 500$ of measurements (number of digitized fragment-displacement vectors) and the corresponding Student's coefficient $t \approx 2$, we have

$$\boldsymbol{\delta}_{\langle \Delta \boldsymbol{\varepsilon} \rangle} = t\sqrt{\frac{1}{N}}\mathbf{S} \approx (6, 3) \text{ nm}.$$

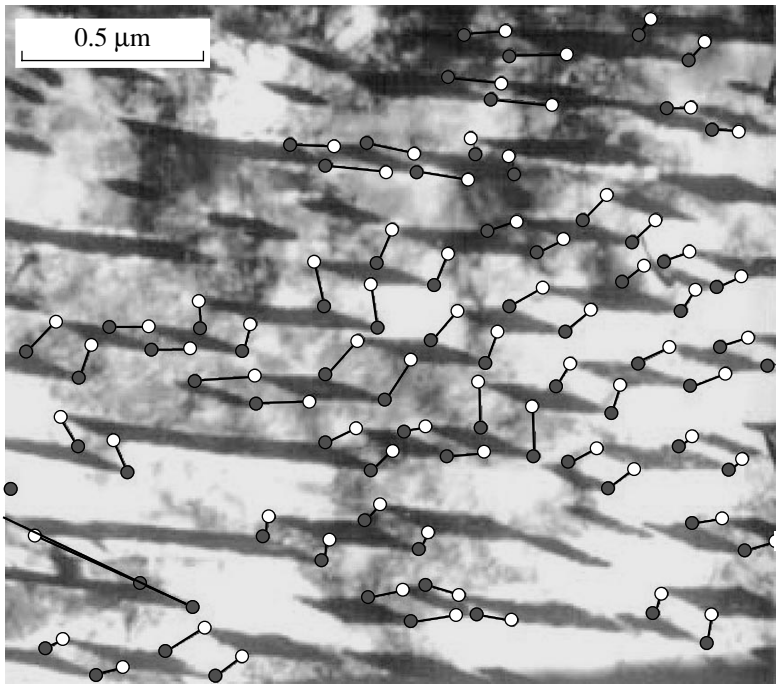

Fig. 2. A part of the perlite-structure image subjected to computer digitization with subsequent statistical treatment. Displacements of cementite-plate fragments are marked by short segments.

velocity gradient must be low and, correspondingly, strain fluctuations must be at their lowest. Otherwise, this could lead to the presence in the sample of domains of local compression and rarefaction of the material, the appearance of which is accompanied by significant energy expenditures. Insofar as the strain causes a significant variation in the specific volume, this strain cannot be elastically fixed in residual microstructure changes. Thus, the displacements of cementite-plate fragments along the direction perpendicular to the shock-wave front are minimal.

The mass velocity may significantly vary along the direction parallel to the shock-wave front. In this case, the material strain is attained by shear and is accompanied by lower energy expenditures. This strain is fixed in the sample microstructure, and the corresponding displacements of cementite-plate fragments are maximal.

We now construct the angular dependence $f(\alpha)$ for the rms projection of strain fluctuations onto the given direction $\mathbf{l}_\alpha = (\cos\alpha, \sin\alpha)$, where α is the polar angle that we (for the sake of obviousness) count off counterclockwise from the direction of the maximum tangent-stress vector $\langle\Delta\boldsymbol{\varepsilon}\rangle$. Let $\Delta\boldsymbol{\varepsilon}(\mathbf{R}_i)$ be the displacement vector located at the point $\mathbf{R}_i$ of the microstructure presented in Figs. 1 and 2. In this case,

$$f(\alpha) = \sqrt{\frac{1}{N}\sum_{i=1}^{N}(\Delta\boldsymbol{\varepsilon}(\mathbf{R}_i), \mathbf{l}_\alpha)^2}.$$

The shape of the dependence $f(\alpha)$ is shown in Fig. 3. For $\alpha \approx 45°$ and $\alpha \approx 135°$, the function $f(\alpha)$ has its minimum and maximum, respectively. This implies that the direction perpendicular to the shock-wave front corresponds to $\alpha \approx 45°$, and the front position is the same as is shown in Fig. 1.

It is worth mentioning that, by virtue of the local character of the transmission electron-microscopy method, the position of the shock-wave front with

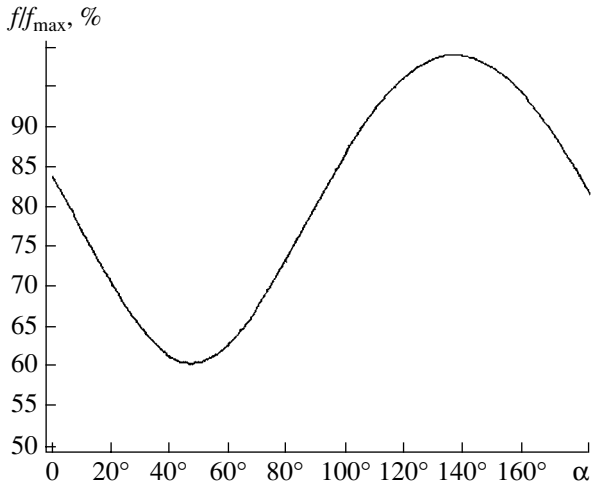

Fig. 3. Angular dependence $f(\alpha)$ of rms strain fluctuations. For $\alpha \approx 45°$ and 135°, the minimum and maximum of the function $f(\alpha)$ are observed. These extrema correspond to the shock-wave front position shown in Fig. 1.

respect to the microstructure shown in Fig. 1 was not known *a priori*. It was only known that the microstructure panorama had been obtained in the plane perpendicular to the surface of the shock-wave front. Thus, the statistical analysis of strain microscopic fluctuations made it possible to associate the local microstructure with the geometry of the shock-wave experiment.

As is seen from Fig. 1, the partial spheroidization of cementite has occurred in perlite colonies located in parallel to the vector $\langle \Delta\boldsymbol{\varepsilon} \rangle$. Fragments of the plates oriented in a proper way are of a rounded shape, whereas the plates aligned along other directions exhibit only brittle fracture. This implies that the dissipation of shock-wave energy proceeds in a different manner depending on the orientation of cementite plates with respect to the shock-wave front. The cementite plates located along the direction of the maximal tangential stresses (at an angle of 45° to the shock-wave front) are heated and coagulate; in other cases, cementite is destroyed by brittle fracture.

Analysis of the origin of the observed microscopic perlite-strain fluctuations in shock waves naturally raises the following question: Is the existence of such fluctuations a manifestation of the poorly investigated fine structure of the shock-wave front, or does the medium itself (to be more precise, its inhomogeneity) lead to the appearance of the corresponding fine structure of the shock-wave flow? In order to answer this question, we should determine the characteristic size of domains in which the displacements of cementite-plate fragments are correlated and then compare the value obtained with the characteristic size of material inhomogeneities (the plate-structure period). A closeness of the indicated values will testify to the interrelation of the fine structure of the front with initial inhomogeneities of the medium.

We will describe the correlations between displacements of the cementite-plate fragments according to the following method. As previously, let the quantity $\Delta\boldsymbol{\varepsilon}(\mathbf{R}_i)$ be the displacement vector located at the point $\mathbf{R}_i$ of the microstructure presented in Figs. 1 and 2. Let also $\{\Delta\boldsymbol{\varepsilon}(\mathbf{R}_k)\}$, $(k = 1, 2, \ldots, n_i)$ be a set of displacement vectors located at a distance of r to $r + \Delta r$ from the point $\mathbf{R}_i$, i.e.,

$$r < |\mathbf{R}_i - \mathbf{R}_k| < r + \Delta r,$$

where n_i is the number of these vectors.

The deviation from zero of the sum of scalar products

$$\varphi_i(r) = \frac{1}{n_i}\sum_{k=1}^{n_i} (\Delta\boldsymbol{\varepsilon}(\mathbf{R}_i), \Delta\boldsymbol{\varepsilon}(\mathbf{R}_k)),$$
$$r < |\mathbf{R}_i - \mathbf{R}_k| < r + \Delta r$$

implies that the displacements by the distance r from the point $\mathbf{R}_i$ are correlated with the displacement at the point $\mathbf{R}_i$. The summation of the functions $\varphi_i(r)$ over all

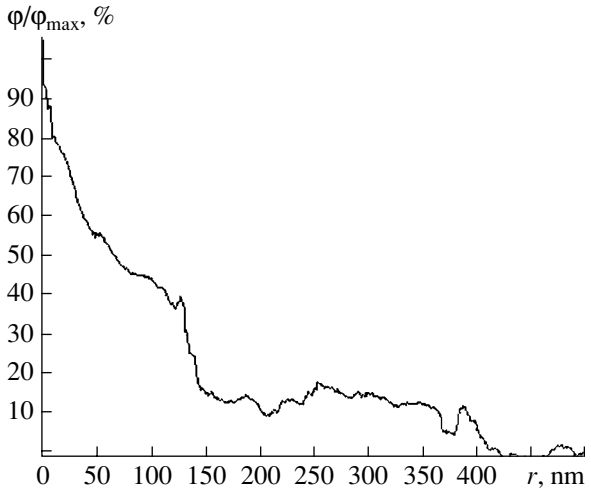

Fig. 4. Dependence of the correlation of displacements for cementite-plate fragments on the distance. The abrupt fall almost to zero of the function $\varphi(r)$ near the point $r = 140$ nm implies the disappearance of correlations.

N digitized vectors and the corresponding normalization allow us to find the function $\varphi(r)$, i.e., the dependence of the displacement correlation on the distance, namely,

$$\varphi(r) = \frac{1}{N}\sum_{i=1}^{N}\left\{\frac{1}{n_i}\sum_{k=1}^{n_i} (\Delta\boldsymbol{\varepsilon}(\mathbf{R}_i), \Delta\boldsymbol{\varepsilon}(\mathbf{R}_k)),\right.$$
$$\left. r < |\mathbf{R}_i - \mathbf{R}_k| < r + \Delta r \right\}.$$

The form of the dependence $\varphi(r)$ is shown in Fig. 4, whence it follows that the correlations disappear at distances of about 140 nm. At this point, an abrupt fall of the function $\varphi(r)$ almost to zero value is observed.

The characteristic size of the correlated-displacement domain is consistent with that of the initial inhomogeneity of the perlite structure (~150 nm). This fact indicates that the physical nature of the observed perlite-strain microscopic inhomogeneities is caused by that of the initial structure and, in other words, is associated with shock waves being scattered due to inhomogeneities of the medium.

Thus, the investigation of perlite-strain microscopic inhomogeneities in shock waves has produced the following conclusions.

1. Statistical analysis of the microscopic displacements of cementite-plate fragments in perlite colonies makes it possible to reveal the direction of the maximum tangential stresses and to determine the orientation of the shock-wave front with respect to the microstructure obtained by the method of local analysis.

2. It is established that the absorption of shock-wave energy by a medium occurs in a different manner

depending on the orientation of the perlite colony with respect to the shock-wave front. In the case that cementite plates are aligned parallel to the direction of the maximum tangent-stress vector, the energy being spent for heating and spheroidizing cementite. Otherwise, the brittle fracture of plates occurs.

3. We have shown that the cause of perlite-strain microscopic fluctuations is the scattering of shock waves due to the initial microscopic inhomogeneities of the medium. These inhomogeneities lead to the formation of the fine structure of the action of shock waves, which is imprinted into the loaded substance and manifests itself in the form of microscopically localized strain.

ACKNOWLEDGMENTS

This work was supported by the Presidium of the Russian Academy of Sciences (Program "Thermal Physics and Mechanics of Intense Energy Actions") and by the Council of the President of the Russian Federation for Support of Young Russian Scientists and Leading Scientific Schools (project no. NSh-778.2003.3).

REFERENCES

1. G. I. Kanel' and S. V. Razorenov, Fiz. Mezomekh. **2**, 13 (1999).
2. V. I. Zel'dovich, B. V. Litvinov, N. P. Purygin, *et al.*, Dokl. Akad. Nauk **343**, 621 (1995) [Phys.–Dokl. **40**, 401 (1995)].
3. A. É. Kheĭfets, V. I. Zel'dovich, N. P. Purygin, *et al.*, Izv. Akad. Nauk **62** (7), 1303 (1998).
4. A. E. Kheifets, V. I. Zel'dovich, B. V. Litvinov, *et al.*, Phys. Met. Metallogr. **90** (Suppl. 1), 108 (2000).
5. V. I. Buzanov and N. P. Purygin, in *Detonation: Proceedings of X Symposium on Burning and Explosion* (Chernogolovka, 1992), pp. 131–132 [in Russian].
6. V. K. Babich, Yu. P. Gul', and I. E. Dolzhenkov, *Strain Ageing of Steel* (Metallurgiya, Moscow, 1972) [in Russian].

Translated by G. Merzon

Doklady Physics, Vol. 50, No. 7, 2005, pp. 371–376. Translated from Doklady Akademii Nauk, Vol. 403, No. 3, 2005, pp. 339–344.

TECHNICAL PHYSICS

Analytical Inversion of a Hypersingular Operator and Its Application to Diffraction Theory

S. I. Éminov

Presented by Academician A.F. Andreev January 28, 2005

Received November 17, 2004

The inversion formulas for a Cauchy-type integral [1, p. 444] and for an integral operator with a logarithmic kernel [1, p. 585] are well known. In this work, we derive an inversion formula for a hypersingular operator and construct effective numerical–analytical methods for solving the hypersingular integral equations of diffraction theory and antenna theory.

An equation of the form

$$(Au)(\tau) + (Nu)(\tau) = v(\tau), \quad -1 \le \tau \le 1, \qquad (1)$$

where

$$(Au)(\tau) = \frac{1}{\pi}\frac{\partial}{\partial\tau}\int_{-1}^{1} u(t)\frac{\partial}{\partial t}\ln\frac{1}{|t-\tau|}dt, \qquad (2)$$

$$(Nu)(\tau) = \int_{-1}^{1} u(t)N(t,\tau)dt \qquad (3)$$

is referred to as a hypersingular equation. Equation (1) arises when solving problems of diffraction (Appendix 1), elasticity, and antennas (Appendix 2). This equation, as well as an integral equation with a logarithmic kernel, attracted great interest in the latter half of the last century (see [2–4] and references therein).

In the 1960s and 1970s, Eq. (1) was usually solved by integrating it by parts and then reducing it to a singular equation for the derivative of an unknown function [2, 3]. Some direct numerical methods for solving hypersingular equations were developed later. The collocation method, which was based on a piecewise constant basis, and the Galerkin method, were proposed in [4] and [5], respectively. Chebyshev polynomials of the second kind multiplied by a weight function were used in the latter paper as the basis functions.

However, in many applied problems, in particular, in antenna theory, direct numerical methods become ineffective owing to the behavior of the right-hand side of Eq. (1), i.e., the function $v(\tau)$. This function can have a pronounced extremum, and, therefore, its expansion into a series can be slowly convergent. For this reason, direct numerical methods are ineffective in these cases.

In this paper, with the object of solving this problem, we propose a new method based on an analytical inversion of the hypersingular operator. We construct the numerical–analytical schemes based on the Galerkin and collocation methods.

ANALYTICAL INVERSION OF THE HYPERSINGULAR OPERATOR

The hypersingular operator was studied, in particular, in [5], where it was written in the form

$$(Au)(\tau) = \int_{-\infty}^{+\infty}|x|\int_{-1}^{1} u(t)\exp(ix(t-\tau))dt\,dx. \qquad (4)$$

The operator A is unbounded in the space $L_2[-1, 1]$; therefore, the equality of operators defined by Eqs. (2) and (4) signifies an equality on a dense set. This statement is proven directly using the well-known relation

$$\ln\frac{1}{|\tau-t|} = C + \int_0^1 \frac{\cos(\tau-t)x - 1}{x}dx + \int_1^{+\infty}\frac{\cos(\tau-t)x}{x}dx,$$

where C is the Euler constant.

As was proven in [5], the domain of definition of the operator A is dense in $L_2[-1, 1]$ and the operator is symmetric and positive definite. These properties allow us to introduce the energy space H_A of the operator A, as well as an analytical orthonormal basis of the energy space H_A, in the form

$$\varphi_n(\tau) = \sqrt{\frac{2}{\pi n}}\sin[n\arccos\tau] = \sqrt{\frac{2}{\pi n}}\sqrt{1-\tau^2}U_n(\tau), \qquad (5)$$

$$n = 1, 2, \ldots,$$

$$(A\varphi_n, \varphi_m) = \begin{cases} 1, & m = n, \\ 0, & m \ne n. \end{cases} \qquad (6)$$

Novgorod State University,
ul. Bol'shaya S.-Peterburgskaya 41, Novgorod, 173003 Russia
e-mail: theorphy@novsu.ac.ru

1028-3358/05/5007-0371$26.00

Here, $(\cdot, \cdot)$ stands for the scalar product in $L_2[-1, 1]$, and $U(\tau)$ are Chebyshev polynomials of the second kind: $U_1(\tau) = 1$, $U_2(\tau) = 2\tau$, $U_3(\tau) = 4\tau^2 - 1$, etc.

In view of its great importance, we now prove relation (6). We use the known relation for Chebyshev polynomials of the first kind [3]

$$\frac{1}{\pi}\int_{-1}^{1}\frac{\cos(n\arccos t)}{\sqrt{1-t^2}}\ln\frac{1}{|t-\tau|}dt = \frac{1}{n}\cos(n\arccos\tau), \quad n \geq 1. \tag{7}$$

We perform the integration by parts in the expression $A\varphi_m$, find the integral using Eq. (7), and then perform the differentiation. As a result,

$$A\varphi_m = \sqrt{\frac{2}{\pi m}}\frac{\partial}{\partial\tau}\left(\frac{1}{\pi}\int_{-1}^{1}\sin(m\arccos t)\frac{\partial}{\partial t}\ln\frac{1}{|t-\tau|}dt\right)$$

$$= \sqrt{\frac{2}{\pi m}}\frac{\partial}{\partial\tau}\left(\frac{1}{\pi}m\int_{-1}^{1}\frac{\cos(m\arccos t)}{\sqrt{1-t^2}}\ln\frac{1}{|\tau-t|}dt\right) \tag{8}$$

$$= \sqrt{\frac{2}{\pi m}}\frac{\partial}{\partial\tau}\cos(m\arccos\tau) = \sqrt{\frac{2}{\pi m}}\frac{\sin(m\arccos\tau)}{\sqrt{1-\tau^2}}m.$$

Hence,

$$(A\varphi_m, \varphi_m) = \sqrt{\frac{2}{\pi m}}m\sqrt{\frac{2}{\pi n}}$$

$$\times\int_{-1}^{1}\frac{\sin(m\arccos\tau)\sin(n\arccos\tau)}{\sqrt{1-\tau^2}}d\tau$$

$$= \sqrt{\frac{2}{\pi m}}m\sqrt{\frac{2}{\pi n}}\int_{0}^{\pi}\sin(m\varphi)\sin(n\varphi)d\varphi = \begin{cases}1, & m = n,\\ 0, & m \neq n.\end{cases}$$

Thus, relation (6) is proved.

Let us now consider the equation with the hypersingular operator

$$(Au)(\tau) = \frac{1}{\pi}\frac{\partial}{\partial\tau}\int_{-1}^{1}u(t)\frac{\partial}{\partial t}\ln\frac{1}{|t-\tau|}dt = v(\tau), \quad -1 \leq \tau \leq 1. \tag{9}$$

We seek a solution of this equation in the form of a series in the basis functions

$$u(t) = \sum_{n=1}^{+\infty}c_n\varphi_n(t). \tag{10}$$

We then substitute Eq. (10) into Eq. (9) and multiply both sides of the equation by φ_m in $L_2[-1, 1]$. With regard to Eq. (6),

$$c_n = (v, \varphi_n).$$

Therefore, the solution of Eq. (9) has the form

$$u(t) = \sum_{n=1}^{+\infty}(v, \varphi_m)\varphi_n(t). \tag{11}$$

With regard to definition (5) of the basis functions $\varphi_n(t)$, this series can be written as

$$u(\tau) = \frac{2}{\pi}\int_{-1}^{1}v(t)\left(\sum_{n=1}^{+\infty}\frac{1}{n}\sin(n\arccos t)\sin(n\arccos\tau)\right)dt. \tag{12}$$

Finally, using the known sum of the series,

$$\sum_{n=1}^{+\infty}\frac{1}{n}\sin x\sin x' = \frac{\ln 2}{2} + \ln\left|\sin\frac{x+x'}{2}\right| - \frac{1}{2}\ln|\cos x - \cos x'|, \tag{13}$$

we represent the solution of Eq. (9) in the form

$$u(\tau) = \frac{2}{\pi}\int_{-1}^{1}v(t)\left(\frac{\ln 2}{2} + \ln\sin\frac{\theta(t)+\theta(\tau)}{2} - \frac{1}{2}\ln|\tau-t|\right)dt, \tag{14}$$

where $\theta(t) = \arccos t$.

Thus, the solution of Eq. (4) has been found in an analytical form, i.e., an analytical inversion of the hypersingular operator has been found.

As far as we know, formula (14) has been derived for the first time.

REDUCTION OF THE HYPERSINGULAR EQUATION TO AN INFINITE FREDHOLM SYSTEM OF THE SECOND KIND: A NUMERICAL–ANALYTICAL METHOD

Let us consider the initial hypersingular equation

$$\frac{1}{\pi}\frac{\partial}{\partial\tau}\int_{-1}^{1}u(t)\frac{\partial}{\partial t}\ln\frac{1}{|t-\tau|}dt + \int_{-1}^{+1}u(t)N(t,\tau)dt = v(\tau), \quad -1 \leq \tau \leq 1. \tag{15}$$

To solve this equation, we expand the desired function in the basis

$$u(t) = \sum_{n=1}^{+\infty} c_n \varphi_n(t) \tag{16}$$

and reduce Eq. (15) in H_A space to the equivalent infinite system in the space l_2 of sequences

$$c_n + \sum_{m=1}^{+\infty} c_m N_{mn} = \nu_n, \quad 1 \le n \le +\infty, \tag{17}$$

where

$$N_{mn} = \int_{-1}^{+1}\int_{-1}^{+1} N(t,\tau)\varphi_m(t)\varphi_n(\tau)dt\,d\tau,$$

$$\nu_n = \int_{-1}^{+1} \nu(\tau)\varphi_n(\tau)d\tau.$$

If the operator $A^{-1}N$ is completely continuous in H_A space, Eq. (17) is a Fredholm equation of the second kind in the space l_2 of sequences, i.e., the matrix elements N_{mn} define a completely continuous operator. One of the complete continuity criteria for the operator $A^{-1}N$ in H_A space was given in [5].

We now attempt to solve infinite system (17). In many problems of mathematical physics, such infinite systems are effectively solved by the truncation method. We find an approximate solution from the truncated system

$$\tilde{c}_n + \sum_{m=1}^{M} \tilde{c}_m N_{mn} = \nu_n, \quad 1 \le n \le M, \tag{18}$$

and an approximate solution of the hypersingular equation is sought in the form

$$u(t) = \sum_{n=1}^{M} \tilde{c}_n \varphi_n(t).$$

The convergence rate of the truncation method also depends on the decrease rate of the right-hand side of system (17). Since many applied problems are described by systems with slowly decreasing right-hand sides, the truncation method becomes ineffective in these cases. In order to solve this problem, we propose here a new numerical–analytical method. We seek a solution of infinite system (17) in the form

$$c_n = \nu_n + \dot{c_n}. \tag{19}$$

Substituting Eq. (19) into Eq. (17), we obtain

$$\dot{c_n} + \sum_{m=1}^{+\infty} \dot{c_n} N_{mn} = -\sum_{m=1}^{+\infty} \nu_m N_{mn}. \tag{20}$$

The right-hand side of this system decreases rapidly, because the matrix elements N_{mn} determine a completely continuous operator. Solving system (20) by the truncation method and taking Eq. (19) into account, we find the solution of hypersingular equation (15) in the form

$$u(t) = \sum_{n=1}^{+\infty} \nu_n \varphi_n(t) + \sum_{n=1}^{M} \tilde{\dot{c}}_n \varphi_n. \tag{21}$$

Here, $\tilde{\dot{c}}_n$ is the solution of the truncated system corresponding to Eq. (20).

One remark is advisable at this point. The solution of the hypersingular equation is expanded, along with the right-hand side of the equation, into a slowly convergent series. Using formula (14) for the analytical inversion of the hypersingular operator, we write solution (21) in the form

$$u(\tau) = \frac{2}{\pi}\int_{-1}^{1} \nu(t)\left(\frac{\ln 2}{2} + \ln\sin\frac{\theta(t)+\theta(\tau)}{2} - \frac{1}{2}\ln|\tau - t|\right)dt + \sum_{n=1}^{M} \tilde{\dot{c}}_n \varphi_n. \tag{22}$$

NUMERICAL–ANALYTICAL METHOD FOR SOLVING THE HYPERSINGULAR EQUATION IN AN ARBITRARY BASIS

The numerical–analytical method constructed in the preceding section was based on particular basis (5). We now construct such a method with the use of an arbitrary basis. Let us consider the initial equation

$$(Au)(\tau) + (Nu)(\tau) = \nu(\tau), \quad -1 \le \tau \le 1. \tag{23}$$

We write a solution of Eq. (23) in the form

$$u = \nu + w, \tag{24}$$

where the function ν is a solution of the equation

$$(A\nu)(\tau) = \nu(\tau), \quad -1 \le \tau \le 1, \tag{25}$$

and is given by formula (14). Then, the second term in Eq. (24) satisfies the equation

$$(Aw)(\tau) + (Nw)(\tau) = -(N\nu)(\tau), \quad -1 \le \tau \le 1, \tag{26}$$

which follows from Eq. (23).

Table 1

N	$(kl) = \frac{\pi}{2}, \frac{1}{a} = 50, \frac{T}{l} = 1$		$(kl) = \frac{\pi}{4}, \frac{1}{a} = 50, \frac{T}{l} = 1$	
	ReZ	InZ	ReZ	InZ
2	119.88	82.413	33.498	–626.82
3	120.43	83.018	33.982	–634.16
4	120.22	82.893	33.898	–632.54
5	120.23	82.900	33.904	–632.64
10	120.25	82.918	33.910	–632.73
20	120.25	82.915	33.909	–632.708

Table 2

N	$(kl) = \frac{\pi}{2}, \frac{1}{a} = 50, \frac{T}{l} = 1$		$(kl) = \frac{\pi}{4}, \frac{1}{a} = 50, \frac{T}{l} = 1$	
	ReZ	InZ	ReZ	InZ
10	125.99	140.23	36.086	–487.95
20	122.93	92.440	34.822	–598.166
40	121.44	84.672	34.309	–621.04
60	121.01	84.883	34.170	–623.20
80	120.81	84.772	34.105	–624.20
100	120.69	84.600	34.065	–624.19
200	120.46	83.939	33.987	–629.15
300	120.39	83.383	33.960	–630.51

The right-hand side of this equation, in contrast with that of Eq. (23), is expanded into a rapidly convergent series. This statement, which is valid because the operator $A^{-1}N$ is completely continuous in H_A space, can be rigorously proven. Hence, Eq. (26) can be solved by various numerical methods. In this paper, the collocation method in a piecewise constant basis will be used.

NUMERICAL SOLUTION OF THE HYPERSINGULAR EQUATION FOR DIPOLE ANTENNAS

As an example, we now consider the hypersingular equation for the surface current $I(\tau)$ of a dipole antenna (Appendix 2).

In the theory of dipole antennas, as in mathematical physics as a whole, the delta-function model is commonly used. In this model, the initial field is presented in the form

$$E^0(\tau) = U_0\delta(\tau), \tag{27}$$

where $\delta(\tau)$ is the Dirac delta function and U_0 is the constant voltage amplitude.

However, such a model cannot be used to determine the input resistance. As follows from the formulas for analytical inversion, the corresponding solution of Eq. (23) becomes infinite, which scenario yields no physical meaning. Moreover, the delta-function model is applicable to the determination of fields in the far wave zone.

For this reason, we consider the model

$$E^0(\tau) = \frac{U_0}{2T}\begin{cases}1, & |\tau| \le T,\\ 0, & |\tau| > T.\end{cases} \tag{28}$$

Function (28) tends to delta function (27) in an integral sense as the parameter T tends to zero.

In this case, integral (14) can be found in the explicit form

$$\frac{2}{\pi}\int_{-1}^{1} E^0(t)\left(\frac{\ln 2}{2} + \ln\sin\frac{\theta(t)+\theta(\tau)}{2} - \frac{1}{2}\ln|\tau - t|\right)dt = U_0\frac{f(T,\tau) - f(-T,\tau)}{\pi T}, \tag{29}$$

where

$$f(t,\tau) = \frac{\ln 2}{2}t + \frac{1}{2}\ln\frac{1 - t\tau + \sqrt{1-t^2}\sqrt{1-\tau^2}}{2}(t-\tau) - \frac{\theta(t)\sqrt{1-\tau^2}}{2} - \frac{(t-\tau)\ln|t-\tau|}{2}.$$

Two properties follow from the analysis of Eq. (29). If $T = 1$, the right-hand side of Eq. (29) satisfies the Meiksner condition at the edge. If $\tau = 0$, the right-hand side of Eq. (29) diverges logarithmically as $T \longrightarrow 0$; therefore, model (27) is inapplicable in this case.

In conclusion, we present some solutions of hypersingular equation (23). We solved the equation by the following four methods: the Galerkin method with basis (5), the collocation method with a piecewise constant basis, the numerical–analytical method with basis (5), and the numerical-analytical method with a piecewise constant basis.

The calculation results for the input resistance that is determined by the formula

$$Z = \frac{U_0}{I(0)}$$

are listed in the tables for various numbers N of the basis functions. The tables demonstrate the convergence of all the methods; i.e., the results are stabilized as the number of basis functions increases.

Table 3

N	$(kl)=\frac{\pi}{2}, \frac{1}{a}=50, \frac{T}{l}=0.05$		$(kl)=\frac{\pi}{4}, \frac{1}{a}=50, \frac{T}{l}=0.02$	
	ReZ	InZ	ReZ	InZ
2	84.550	53.826	84.496	53.781
3	89.194	52.625	89.164	52.568
4	90.482	51.542	90.474	51.468
5	91.579	50.893	91.599	50.800
10	94.105	49.270	94.310	49.042
20	95.573	48.212	96.326	47.558

Table 4

N	$(kl)=\frac{\pi}{2}, \frac{1}{a}=50, \frac{T}{l}=0.05$		$(kl)=\frac{\pi}{4}, \frac{1}{a}=50, \frac{T}{l}=0.02$	
	ReZ	InZ	ReZ	InZ
20	50.052	28.946		
40	98.086	49.799		
60	148.02	73.302	59.210	29.321
80	97.144	49.663	79.341	38.438
100	80.283	41.624	99.584	47.352
120	96.719	49.362	119.92	56.115
140	84.157	43.372	140.352	64.762

Table 5

N	$(kl)=\frac{\pi}{2}, \frac{1}{a}=50, \frac{T}{l}=0.05$		$(kl)=\frac{\pi}{4}, \frac{1}{a}=50, \frac{T}{l}=0.02$	
	ReZ	InZ	ReZ	InZ
2	90.729	50.481	93.443	48.607
3	94.286	49.471	97.058	47.350
4	94.664	48.821	97.415	46.648
5	95.090	48.534	97.845	46.319
10	95.656	48.158	98.435	45.872
20	95.670	48.140	98.440	45.858

Table 6

N	$(kl)=\frac{\pi}{2}, \frac{1}{a}=50, \frac{T}{l}=0.05$		$(kl)=\frac{\pi}{4}, \frac{1}{a}=50, \frac{T}{l}=0.02$	
	ReZ	InZ	ReZ	InZ
11	124.04	85.381	124.39	77.049
21	103.98	54.980	104.45	50.738
41	98.724	49.780	101.35	47.418
61	98.006	49.861	100.93	47.692
81	97.465	49.682	100.48	47.556
101	97.181	49.537	99.931	47.278

The results obtained by the Galerkin and collocation methods are presented in Tables 1 and 2, respectively, for the case $\frac{T}{l}=1$, i.e., for the uniform initial field distribution over the dipole length. These tables show that the methods are rapidly convergent and are in strong agreement with each other, in spite of their different natures.

Similar results obtained by the Galerkin and collocation methods for the case of the variable parameter $\frac{T}{l}$ are listed in Tables 3 and 4, respectively. In this case, the convergence rate of the numerical methods decreases with the parameter $\frac{T}{l}$. The slow convergence of numerical methods in antenna theory turns out to be primarily attributable to the behavior of the right-hand side of the corresponding integral equations. In antenna feed problems, initial fields are localized in regions that are much smaller than the antenna length.

The numerical–analytical methods proposed above completely solve the problem of the evaluation of input resistances.

As is seen in Tables 5 and 6, the numerical–analytical methods with basis (5) and the piecewise constant basis, respectively, are rapidly convergent.

Thus, the numerical–analytical methods that have been developed in this paper completely solve the problem of the calculation of dipole and many other types of antennas, as well as diffraction problems for the case in which initial-field sources are located close to the diffraction surface.

APPENDIX 1

INTEGRO-DIFFERENTIAL EQUATION DESCRIBING THE DIFFRACTION OF *H* WAVES BY A STRIP

The integro-differential equation describing the diffraction of *H* waves by a strip (both the electric field and surface currents are perpendicular to the strip) has the form [6]

$$\frac{1}{4kd}\sqrt{\frac{\mu}{\varepsilon}}\frac{\partial}{\partial t}\int_{-1}^{1} j(t)\frac{\partial}{\partial \tau}H_0^{(2)}(kd|\tau-t|)dt$$

$$-\frac{kd}{4}\sqrt{\frac{\mu}{\varepsilon}}\int_{-1}^{1} j(t)H_0^{(2)}(kd|\tau-t|)dt = -E(\tau), \quad -1\le\tau\le 1.$$

Here, j is the desired function of the surface current density; E^0 is the initial electric field; ε and μ are the electric permittivity and magnetic permeability, respectively; k is the wavenumber; $2d$ is the width of the strip; and $H_0^{(2)}$ is the Hankel function. Isolating the singularity of the Hankel function, we arrive at the hypersingular equation

$$\frac{\beta}{\pi}\frac{\partial}{\partial\tau}\int_{-1}^{1} j(t)\frac{\partial}{\partial t}\ln\frac{1}{|t-\tau|}dt + \int_{-1}^{1} j(t)N(\tau,t)dt = -E(\tau), \quad -1 \le \tau \le 1, \tag{30}$$

where

$$\beta = \frac{i}{2ka}\sqrt{\frac{\mu}{\varepsilon}},$$

$$N(\tau,t) = \frac{1}{4ka}\sqrt{\frac{\mu}{\varepsilon}}\frac{\partial}{\partial\tau}\frac{\partial}{\partial t}\left[H_0^{(2)}(ka|\tau-t|) - \frac{2i}{\pi}\ln\frac{1}{|\tau-t|}\right] - \frac{ka}{4}\sqrt{\frac{\mu}{\varepsilon}}H_0^{(2)}(ka|\tau-t|).$$

APPENDIX 2

INTEGRO-DIFFERENTIAL EQUATION FOR DIPOLE ANTENNAS

Let an arbitrary electromagnetic wave ($\mathbf{E}^0$, $\mathbf{H}^0$) fall on a dipole antenna. The wave field induces electric currents with density $\mathbf{j}$ on the surface S of the antenna. These currents satisfy the equation [5]

$$\left(\frac{d^2}{dz^2} + k^2\right)\iint_S j_z(z')\frac{e^{-ikR}}{4\pi R}dS' = -i\omega\varepsilon E_z^0(z). \tag{31}$$

Here, $R = \sqrt{(z-z')^2 + 2\alpha^2(1-\cos(\varphi-\varphi'))}$, where a is the radius of the dipole.

Since integral equation (31) is two-dimensional and the current depends on only one variable, the kernel can be integrated with respect to one variable. Introducing the current

$$j_z(z)2\pi a = I(z),$$

we arrive at the integro-differential equation

$$-\left(\frac{d^2}{(kl)d\tau^2} + (kl)\right)\int_{-1}^{1} I(t)B(\tau,t)dt = i\sqrt{\frac{\mu}{\varepsilon}}\frac{1}{k}E(\tau), \quad -1 \le \tau \le 1, \tag{32}$$

where

$$B(\tau,t) = \frac{1}{4\pi^2}\int_0^{2\pi}\frac{\exp(-iR)}{R}d\varphi,$$

$$R = \sqrt{(kl)^2(\tau-t)^2 + 4(ka)^2\sin^2\frac{\varphi}{2}},$$

and $2l$ is the length of the dipole. Isolating the logarithmic singularity of the kernel

$$B(\tau,t) = \frac{1}{4\pi^2}\int_0^{2\pi}\left[\frac{\exp(-iR)}{R} - \frac{1}{\sqrt{(kl)^2(\tau-t)^2 + (ka)^2\varphi^2}}\right]d\varphi + \frac{1}{4\pi^2(ka)}\ln\left[\frac{\pi a}{l} + \sqrt{\left(\frac{\pi a}{l}\right)^2 + (\tau-t)^2}\right] - \frac{1}{4\pi^2(ka)}\ln|\tau-t| \equiv B_1(\tau-t) + \frac{1}{4\pi^2(ka)}\ln\frac{1}{|\tau-t|},$$

we arrive at the hypersingular equation

$$\frac{\beta}{\pi}\frac{\partial}{\partial\tau}\int_{-1}^{1} I(t)\frac{\partial}{\partial t}\ln\frac{1}{|t-\tau|}dt + \int_{-1}^{1} I(t)N(\tau,t)dt = i\sqrt{\frac{\mu}{\varepsilon}}\frac{1}{k}E(\tau), \quad -1 \le \tau \le 1, \tag{33}$$

where

$$\beta = \frac{1}{4\pi(kl)(ka)},$$

$$N(\tau,t) = -(kl)B(\tau,t) - \frac{d^2}{(kl)d\tau^2}B_1(\tau,t).$$

REFERENCES

1. F. D. Gakhov, *Boundary Value Problems*, 3rd ed. (Nauka, Moscow, 1977; Addison-Wesley, Reading, Mass., 1966).
2. A. I. Kalandiya, *Mathematical Methods of Two-Dimensional Elasticity* (Nauka, Moscow, 1973; Mir, Moscow, 1978).
3. V. V. Panasyuk, M. P. Savruk, and Z. T. Nazarchuk, *Method of Singular Integral Equations in Two-Dimensional Diffraction Problems* (Naukova Dumka, Kiev, 1984) [in Russian].
4. I. K. Lifanov, *Method of Singular Integral Equations and Numerical Experiment* (Yanus, Moscow, 1995) [in Russian].
5. S. I. Éminov, Radiotekh. Elektron. (Moscow) **38** (12), 2160 (1993).
6. E. V. Zakharov and Yu. V. Pimenov, *Numerical Analysis of Radio-Wave Diffraction* (Radio i Svyaz', Moscow, 1982) [in Russian].

Translated by V. Chechin

Doklady Physics, Vol. 50, No. 7, 2005, pp. 377–379. Translated from Doklady Akademii Nauk, Vol. 403, No. 1, 2005, pp. 37–39.

MECHANICS

Longitudinal Structures in Plane Jets

A. V. Boĭko[1], H. H. Chun[2], M. V. Litvinenko[3], V. V. Kozlov[1], E. E. Cherednichenko[1], and I. Lee[2]

Presented by Academician V.E. Nakoryakov December 22, 2004

Received January 11, 2005

The physics of mixing in jets is of considerable interest from the standpoint of both fundamental science and practical application. The intensity and homogeneity of mixing significantly affect the combustion efficiency, heat transfer coefficient, formation of waste, and jet noise (see, e.g., [1]).

Laminar jets have inflectional mean velocity profiles. This property leads to the formation of Kelvin–Helmholtz vortices, which represent the main instability of such shear layers. The initial stage in the development of these vortices is usually well described by linear stability theory (see, e.g., review [2]). The next, nonlinear stage is characterized by amplitude saturation and vortex pairing due to the resonance of disturbances with subharmonics and superharmonics. Further development of nonlinear structures is often accompanied by the occurrence of longitudinal, or streamwise, vortical structures. Their formation is usually attributed to the so-called secondary three-dimensional instability of the Kelvin–Helmholtz vortices [3, 4]. Experiments show that the dynamics of these structures play an important role in the mixing process in the far wake of a jet [5].

Other longitudinal disturbances that can often be developed in shear layers are formed downstream of nozzle surface irregularities [6]. These are regions of quasi-stationary three-dimensional deformations, mainly of the longitudinal velocity in the shear flow, and have a characteristic form of "streaks" in the visualization pictures [7]. Their occurrence is not due to the secondary instability of the Kelvin–Helmholtz vortices. These structures arise as a result of stabilization effects upon the development of compact three-dimensional disturbances of the normal velocity component even with small amplitude [7]. These longitudinal structures intensely interact with other flow disturbances, e.g., instability waves. This interaction usually accelerates flow turbulization [8]. This feature of the streaky structures makes them a promising means for improving the mixing and control over the flow in jets.

There is an extensive literature on the investigation of longitudinal structures in wall flows (see, e.g., the overview in [7]). However, investigations into the physics of similar structures in jets began only recently. Successful excitation and observation of natural longitudinal structures and their interaction with Kelvin–Helmholtz vortices in circular jets [9] offer the possibility of studying controlled longitudinal structures in plane jets. To this end, a simple but efficient smoke visualization technique using a pulsed laser sheet synchronized with the Kelvin–Helmholtz vortex shedding was applied in this study.

The plane jet generator and visualization schematics are presented in Fig. 1. The flow was produced by a DISA wind tunnel that is designed for the calibration of sensors of a hot-wire anemometer and ensures a stable air flow rate. Smoke was supplied to the test section through a tube connected to a smoke generator. The

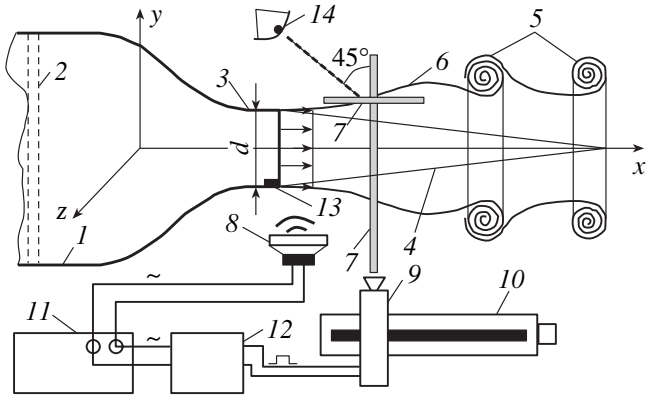

Fig. 1. Experimental setup and jet stream: (*1*) plenum chamber, (*2*) deturbulizing grids, (*3*) nozzle, (*4*) potential jet core, (*5*) Kelvin–Helmholtz vortices, (*6*) shear layer, (*7*) laser sheet, (*8*) loudspeaker, (*9*) laser, (*10*) coordinate device, (*11*) generator, (*12*) phase variator, (*13*) roughness elements, and (*14*) video camera.

[1] *Institute of Theoretical and Applied Mechanics, Siberian Division, Russian Academy of Sciences, ul. Institutskaya 4/1, Novosibirsk, 630090 Russia*
e-mail: boiko@itam.nsc.ru

[2] *Advanced Ship Engineering Research Center, Pusan National University, Pusan, 609-735 Korea*

[3] *Chalmers University of Technology, Gothenburg, Sweden*

1028-3358/05/5007-0377$26.00

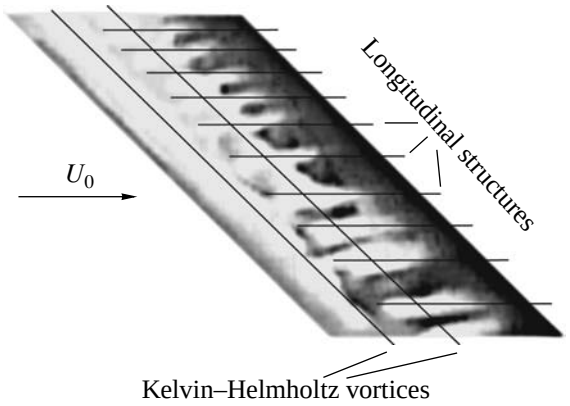

Fig. 2. Visualization of a longitudinal section of the jet in the shear layer at $U_0 = 3$ m/s.

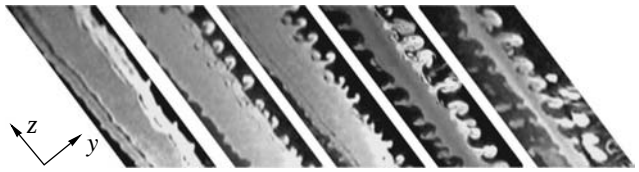

Fig. 3. Visualization of cross sections of the jet with streaky structures at distances of (from left to right) 5, 25, 45, 65, and 85 mm from the nozzle.

tunnel diffuser was connected to the plenum chamber of the setup. A separating plate was placed in the plenum chamber for producing a uniform jet stream. Low turbulence level was ensured by a punched screen, honeycombs, and two grids, as well as by a 10 : 1 contraction. A rectangular nozzle at the plenum chamber exit had a height of $h = 10$ mm and a width of $l = 200$ mm. The jet was visualized in its cross sections at distances of 5 to 85 mm from the nozzle exit and in the longitudinal sections in the shear layer region using a laser sheet about 0.3-mm thick. The accuracy of positioning the coordinate device was 0.1 mm.

In standard experiments, continuous light restricts the use of the laser sheet to quasi-stationary phenomena. For this reason, it is difficult to study periodic flow disturbances. In order to overcome this limitation, we used a pulsed semiconductor laser with a wavelength of 650 nm and a pulse power of 150 mW, which allowed for the synchronization of the laser pulse starting from the front of an external rectangular signal. In these experiments, the laser pulse duration was 255 μs. Stroboscopic images of the flow sections were shot at a speed of 25 fps by a stationary video camera placed at an angle of 45° to the plane of the section at a distance of 0.5 m from the jet axis. Then, the record was processed using a personal computer.

The natural shedding frequency of Kelvin–Helmholtz vortices was slightly time-dependent. This dependence was minimized by generating controlled vortical disturbances in the flow by means of 140-Hz sound, which were emitted by a loudspeaker normal to the jet at a distance of 200 mm from the nozzle. The acoustic level measured at the center of the nozzle exit by a microphone oriented normal to the loudspeaker plane was 90 dB. Rectangular signals were supplied to the laser at the sound frequency. Using a phase variator, it was possible to change the duration of these signals and, therefore, the localization of signal fronts, relative to the period of the vortical disturbances generated. This procedure enabled us to stroboscopically "freeze" most interesting stages of the periodic phenomena in a visualized section.

Longitudinal structures were controllably generated downstream of roughness elements—0.2-mm high, 20-mm long, and 5-mm wide—that were placed near one of the bases of the nozzle exit along its span, at a distance of 10 mm from each other. This distance was chosen so that the transverse dimension of the structures was equal to several characteristic thicknesses of the jet shear layer, in accordance with the parameters of streaky structures naturally developed in wall boundary layers [10].

The jet outflow velocity U_0 ranged from 2 to 12.2 m/s, which corresponded to the Reynolds number $\mathrm{Re} \approx \dfrac{hU_0}{\nu}$, where h is the height, from 1.3×10^3 to 8×10^3. The rms disturbance intensity measured by the hot-wire anemometer on the jet axis and in the shear layer near the nozzle exit did not exceed 0.4 and 1.5% of U_0.

It is seen that the two-dimensional Kelvin–Helmholtz vortices oriented across the flow and the longitudinal structures (streamwise "rays") coexist in the shear layer (see Fig. 2). Their interaction results in a complicated periodic disturbance pattern that is periodic both in time and space.

Several snapshots of the visualization of jet cross sections are presented in Fig. 3. They show the result of the interaction between the longitudinal structures and Kelvin–Helmholtz vortices, namely, the downstream development of a periodic system of mushroom-shaped structures that "escape" from the shear layer into the ambient space. This process is obviously similar to the development of lambda structures in boundary layers, whose "hats" are carried away into the external flow [7]. Though the irregularities were located on only one side of the nozzle, the mushroom structures developed in both shear layers; their dimensions were greater, though, in the layer modulated by the roughness elements. Vortical motion within the mushroom structures is also visible in the video record; that is, this rotation is not synchronized with the acoustic excitation and vortex period. Flow visualization in different longitudinal and transverse sections indicates that the Kelvin–Helmholtz vortices do not penetrate into this region, and the process of mixing with the ambient air is determined by the behavior of these structures. We also

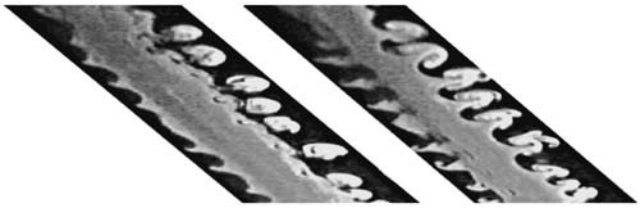

Fig. 4. Visualization of a cross section of the jet in the shear layer at $U_0 = 2$ and 4 m/s.

emphasize the continuous downstream narrowing of the potential jet core due to the growth of the shear layer thicknesses.

Figure 4 shows two visualizations of the same jet cross section at flow velocities $U_0 = 2$ and 4 m/s. Obviously, the fluctuation amplitude increases with the velocity of the outflow from the nozzle, but this increase does not lead to any qualitative changes in the features of the mixing in the flow under consideration. Similar results were also obtained for other velocities in the range under consideration.

Thus, it has been shown that longitudinal structures in a jet can be generated by surface irregularities located at the nozzle exit. The interaction between Kelvin–Helmholtz vortices and these structures leads to the formation of a periodic three-dimensional flow pattern. This interaction gives rise to the appearance of vortical structures that are carried away into the ambient space and have the form of rays and mushroom structures in longitudinal and cross sections, respectively. In the region of their development, the jet and ambient air are intensely mixed. It has been found that a sixfold increase in the jet Reynolds number from 1.3×10^3 to 8×10^3 enhances the mixing process without qualitative changes occurring in the observable processes.

ACKNOWLEDGMENTS

This work was supported by the Council of the President of the Russian Federation for Support of Young Russian Scientists and Leading Scientific Schools (project no. NSh-964.2003.01), as well as by the Siberian Division of the RAS and the Advanced Ship Engineering Research Center of the Korea Science and Engineering Foundation (integration project no. 25).

REFERENCES

1. H. Hu, T. Saga, T. Kobayashi, and N. Taniguchi, Phys. Fluids **13**, 3425 (2001).
2. C.-M. Ho and P. Huerre, Annu. Rev. Fluid Mech. **16**, 365 (1984).
3. D. Liepmann and M. Gharib, J. Fluid Mech. **245**, 643 (1992).
4. P. Brancher, J. M. Chomaz, and P. Huerre, Phys. Fluids **6**, 1768 (1994).
5. J. H. Citrinity and W. K. George, J. Fluid Mech. **418**, 137 (2000).
6. A. A. Bakchinov, H. R. Grek, B. G. B. Klingmann, and V. V. Kozlov, Phys. Fluids **7**, 820 (1995).
7. A. V. Boiko, A. V. Dovgal, G. R. Grek, and V. V. Kozlov, *The Origin of Turbulence in Near-Wall Flows* (Springer-Verlag, Berlin, 2002).
8. A. V. Boiko, K. J. A. Westlin, B. G. B. Klingmann, *et al.*, J. Fluid Mech. **281**, 219 (1994).
9. M. V. Litvinenko, V. V. Kozlov, G. V. Kozlov, and G. R. Grek, Prikl. Mekh. Tekh. Fiz. **45** (3), 50 (2004).
10. K. J. A. Westlin, A. V. Boiko, B. G. B. Klingmann, *et al.*, J. Fluid Mech. **281**, 193 (1994).

Translated by M. Lebedev

Doklady Physics, Vol. 50, No. 7, 2005, pp. 380–384. Translated from Doklady Akademii Nauk, Vol. 403, No. 1, 2005, pp. 40–44.

MECHANICS

Asymptotic Laws of Wetting Hydrodynamics

O. V. Voinov

Presented by Academician G.G. Chernyĭ December 29, 2004

Received December 30, 2004

Slow flows of a viscous liquid on a solid surface in the presence of a free boundary and a moving contact line of three phases are considered. A second-order asymptotic theory is developed for describing the laws of varying the free boundary at a finite dynamic contact angle.

The approximate dependences of the contact angle on the dimensionless velocity $\alpha_0 \sim \mathrm{Ca}^{1/3}$ for the wetting of a surface, as well as on the dimensionless time for the spreading of a drop on a wall, are known [1–3], having been treated by De Gennes [4] as similarity laws in wetting dynamics. However, due to the effect of the scaling factor [1, 2], such a treatment is possible only in a narrow approximate sense.

The dynamic (apparent) contact angle α_0 exists because a flow described by the general asymptotic law [1] is characterized by several scales. The width of the range of scales in the logarithmic scale is a large parameter of the theory. A second-order theory describes the scaling effect of wetting dynamics in terms of the large parameter or corresponding inverse small parameter ε. Second-order asymptotic solutions of wetting dynamic problems are known for small contact angles [2]. The flows with dynamic contact angles for the wetting of a tube and the spontaneous spreading of a drop on a wall that are considered in this work share a common property in the quasi-equilibrium of free boundaries at the large scale.

RELATIONS ON A MOVING CONTACT LINE OF THREE PHASES

The dynamics of the wetting of a solid includes mechanisms that are realized at the microscopic scale beyond the scope of hydrodynamics. They correspond to the common equation of energy at a moving contact line of three phases [1]:

$$\cos\alpha_m = \sigma_2 - \sigma_1 - \frac{G\,\mathrm{sgn}\,v}{\sigma}, \qquad E_m = |v|G(v) \geq 0. \tag{1}$$

Here, σ_1 and σ_2 are the surface free energy densities at the solid–liquid and solid–gas interfaces, respectively; σ is the surface tension of the liquid; v is the wetting rate; $E_m(v)$ is the energy dissipation in unit time per unit length of the contact line; and $\alpha_m(v)$ is the microscopic contact wetting angle. For $E_m = 0$, α_m is equal to the static contact angle α_s according to the Young equation. Relation (1) is important for the formulation of the problem.

(i) For constant $G > 0$, it describes two effects [1]: first, the dependence of the contact angle on the sign of low velocity v, i.e., static angle hysteresis, and, second, the limiting contact angle for high velocities, i.e., the Ablett effect [5]. The latter effect was observed in experiments for low Reynolds numbers, but it is manifested in some systems with low-viscosity liquids. The Ablett effect is used in computer simulations of the flows with high Reynolds numbers that arise when a drop collides with a solid wall [6, 7].

Equation (1) with the variable G for the case in which $\Delta\sigma = \sigma_2 - \sigma_1 - \sigma < 0$ describes Ablett experiments at velocities less than the limiting value.

(ii) Equation (1) determines the energy balance in the precursor-film flow [1, 2] for the case of complete wetting ($\Delta\sigma > 0$): $G = \Delta\sigma$ and $\alpha_m = 0$.

(iii) The case of $\Delta\sigma > 0$ and $G - \Delta\sigma > 0$ considered in [1] corresponds to $\alpha_m > 0$, i.e., the appearance of the contact angle in complete wetting due to the microdissipation of energy E_m. This contact angle can be realized in experiments with low-viscosity liquids [8].

For a high-viscosity liquid, the apparent contact angle α_0 can differ from the microangle α_m, because the flow near the contact line is multiscale.

Institute of Theoretical and Applied Mechanics (Tyumen Branch), Siberian Division, Russian Academy of Sciences, ul. Taĭmyrskaya 74, Tyumen, 625000 Russia

1028-3358/05/5007-0380$26.00

A SECOND-ORDER ASYMPTOTIC THEORY OF WETTING DYNAMICS

We consider the dynamics of a nonvolatile liquid in zero gravity for low Reynolds numbers and capillary number $\mathrm{Ca} = \frac{\mu v}{\sigma}$ (μ is the dynamic viscosity). For a large scale, the liquid flow is described by Stokes equations. The velocity on the solid is zero: $\mathbf{u} = 0$. At the free boundary S, the tangent stress is $P_\tau = 0$; the mean curvature H satisfies the Laplace condition $2\sigma H = P_n + p_0$, where P_n is the normal stress in the liquid and p_0 is the pressure in the gas; and the normal component of the velocities of the liquid and solid are equal to each other: $(\mathbf{un}) = w$.

For small distances near the moving contact line, the following general asymptotic relation is valid for the tangent angle α to the free surface [1–3]:

$$\frac{1}{2}\int_{\alpha_m}^{\alpha}\left(\frac{\alpha}{\sin\alpha} - \cos\alpha\right)d\alpha + \mathrm{Ca}\ln\frac{\sin\alpha}{\sin\alpha_*} = \mathrm{Ca}\ln\frac{h}{h_m}, \quad (2)$$
$$h \gg h_m,$$

where h_m is the microscopic scale, microangle α_m corresponds to Eq. (1), and $\alpha_* = \alpha_m$ for $\alpha_m \geq |9\mathrm{Ca}|^{1/3}$ and $\alpha_* = (9\mathrm{Ca})^{1/3}$ otherwise. With these parameters, Eq. (2) is known to be in agreement [3] with the small-angle asymptotic relation for $\alpha_m = 0$ [2]. In the flow with a nonzero Reynolds number, the condition $\frac{hv}{\nu} \ll 1$ of the smallness of the local number is necessary (ν is the kinematic viscosity). In an unsteady flow with the characteristic time τ, the condition $\frac{h}{v} \ll \tau$ is necessary. Asymptotic relation (2) is valid for $h_m \ll h \ll h_0$, where the maximum distance h_0 is found from the asymptotic matching condition. According to Eq. (2), the free boundary is close to tangent; i.e., the angle α varies slowly along the boundary: $\frac{d\ln\alpha}{d\ln h} \ll 1$ [1]. This condition is satisfied, because $\ln\frac{h_0}{h_m} \gg 1$. We now introduce the parameter

$$\varepsilon = \left(\ln\frac{h_0}{h_m}\right)^{-1}. \quad (3)$$

Condition $h_0 \gg h_m$ is written in an explicit form in the problem of meniscus motion [2]. For the case of the presence of a precursor film [2] moving under the action of van der Waals forces, the microscale h_m is equal to the maximum thickness of the film. The film can appear for small contact angles α_0, and h_m for finite α_0 values can be on the order of the size of a liquid molecule [1, 2, 4]. If the surface is preliminarily covered with a film of thickness h_∞, the microscale is $h_m = 1.84h_\infty$ [2].

The distance to the contact line $r = h/\sin\alpha$ and $r_m = h_m/\sin\alpha_*$ can be used instead of h and h_m, respectively, in asymptotic relation (2). For the film-covered surface, r_m depends strongly on the velocity, whereas the microscale h_m is independent of the velocity. For this reason, we use the variable h rather than the variable r.

The free boundary S is sought by the method of perturbations in Ca. In the leading approximation, the quasistatic surface S is obtained in the large-scale region, because the angle α varies slowly with distance near the contact line according to asymptotic relation (2) and the wetting rate is low, $v \sim \varepsilon$, for a fixed angle α_0. On the surface S and on the static surface S_1 (spherical segment) close to S, the normal stresses $P_n(\theta) - P_n(0)$ (θ is the polar angle on the sphere) are close to each other. They are found by solving the problem of the flow of the viscous liquid with S_1, and the small perturbation of the surface S_1 is determined from the Laplace boundary condition [1]. From the matching condition for asymptotic expansions of the boundary slope angle α, we derive the formulas for the contact angle α_0 for the surface S_1 in terms of the parameter h_0 in the form of a functional of the stress P_n. The parametric dependence for the maximum scale $h_0 = h_0(\alpha_0)$, which determines the contact angle from asymptotic relation (2) in the form $\alpha_0 = \alpha_{as}(\ln h_0)$, is determined numerically.

ASYMPTOTIC NUMERICAL SOLUTION

Let us give two definitions of the spherical segment S_1 passing through the contact line: (a) the curvature of the sphere is equal to the curvature of the surface S on the axis: $R^{-1} = H(0)$; and (b) the sphere touches the surface S at the point with the coordinate x_2 on the symmetry axis and the segment height is $a_0 = x_2$ ($x_2 = 0$ on the contact line); $a_0 = h(0)$ for the case of a drop.

Calculating perturbation of the surface S_1, we find perturbation of the surface slope angle α_1 near its edge ($\theta \longrightarrow \theta_0$):

$$\alpha - \alpha_1 = \int_0^\theta \frac{P_n(\alpha) - P_n(0)}{\sigma}\Lambda(\theta_0, \theta')R_0 d\theta' + \ldots. \quad (4)$$

Here, $\alpha_1 \approx \alpha_0$, $R_0 = |R|$, $\theta = \left|\frac{1}{2}\pi - \alpha\right|$ for the flow in a tube and $\theta = \alpha$ for the drop, Λ in (4) for cases (a) and

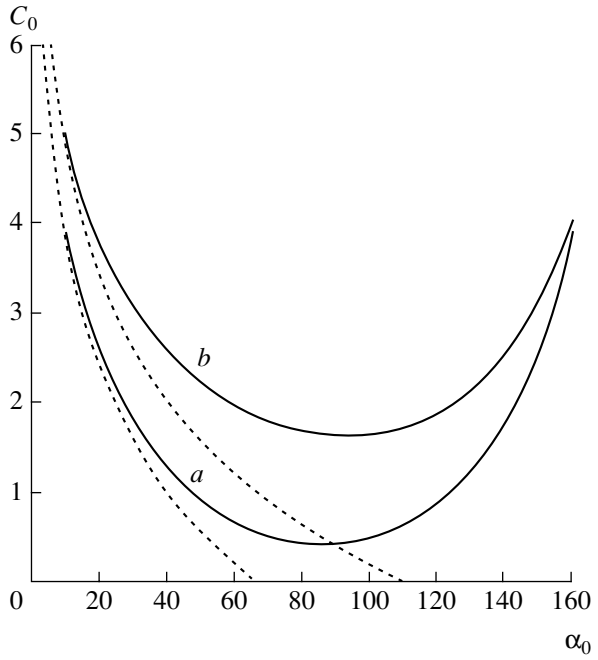

Fig. 1.

(b) has the form

$$\Lambda_a(\theta_0, \theta) = -\frac{\sin 2\theta}{\sin 2\theta_0}, \tag{5}$$

$$\Lambda_b(\theta_0, \theta) = \left[\cos\theta - (1 + \cos\theta_0)\right.$$
$$\left.\times\left(1 + \cos\theta \ln\left(\cot\frac{\theta_0}{2}\tan\frac{\theta}{2}\right)\right)\right]\frac{\sin\theta}{\sin\theta_0}, \tag{6}$$

respectively, and the stress on S_1 is expressed as

$$P_n - P_n(0) = 2\mu v Q \sin\alpha_0 G h^{-1},$$
$$Q = \sin\alpha_0(\alpha_0 - \sin\alpha_0\cos\alpha_0)^{-1}. \tag{7}$$

In the limit $h \longrightarrow 0$, $G \longrightarrow 1$ according to the solution of the problem for the flow in a corner.

Asymptotic matching with the accuracy $O(\varepsilon^2)$ is known for small angles [2]. We use the Taylor expansion of asymptotic relation (2) $[\alpha_{as}(z), z = \ln h]$ at the point $z_0 = \ln h_0$ for $h \ll h_0$:

$$\alpha - \alpha_0 = \varphi(\alpha_0)(z - z_0) + \ldots,$$
$$\alpha_0 = \alpha_{as}(z_0), \quad \varphi = 2Q\mathrm{Ca}. \tag{8}$$

This expansion is justified because $\ln\dfrac{h_0}{h_m} \gg 1$. Formula (8) does not change when h changes to the distance r from the contact line.

Matching expansions (4) and (8) for the flow in the tube with the radius h_k for $h \ll h_0$ ($\theta \longrightarrow \theta_0$), we arrive at the expressions

$$\alpha_0 = \alpha_{as}(\ln h_0), \quad h_0 = h_k \exp(-C_0(\alpha_0)), \tag{9}$$

$$C_{0a} = 1 - \int_0^{h_k}\left(1 - \frac{h}{h_k}\right)\frac{G-1}{h}dh, \tag{10}$$

$$C_{0b} = \cot\theta_0 \int_0^{\theta_0}\left\{\Lambda_b(\theta_0, \theta)G(\theta) + \frac{\cos\theta}{\cos\theta_0}\right\}\frac{h_k}{h}d\theta. \tag{11}$$

The stress P_n on the spherical segment S is calculated for the Stokes flow in the tube. At a large distance H from the contact line, the velocity profile for the Poiseuille flow is specified. Calculations are performed for $\alpha_0 \le 160°$, because the problem of the flow in the corner is degenerate ($Q = 0$) for $\alpha_0 = \pi$.

The numerical solution of the Stokes equations has been obtained using the method of the boundary integral equation [9]. The velocity of the axisymmetric flow is expressed in terms of two harmonic functions by Oberbeck's formula. To determine these functions, a modified integral equation is used, where the harmonic function $\Phi(\mathbf{x})$ in the integrand is changed so that the double-layer density vanishes at $\mathbf{x} = \mathbf{x}'$ [9]:

$$4\pi K\Phi(\mathbf{x}') = \int\int_{S_L}\left\{\frac{1}{r}\frac{\partial\Phi}{\partial n}(\mathbf{x}) - (\Phi(\mathbf{x}) - \Phi(\mathbf{x}'))\frac{\partial}{\partial n}\frac{1}{r}\right\}dS,$$

where S_L is the boundary of the liquid, $\mathbf{x}, \mathbf{x}' \in S_L$, $r = |\mathbf{x} - \mathbf{x}'|$, and the coefficient K is determined by the geometry of the problem. For the unbounded region beyond S_L, $K = 1$ independently of the connectivity of S_L [9]. For the problem inside the closed boundary S_L, $K = 0$. The modification of the integral equation increases the accuracy of its finite difference approximation. To ensure high accuracy, a special quadrature formula is used [9]. Numerical solutions of the dynamic problems for an ideal liquid with free boundaries [9, 10] demonstrate the efficiency of this approach.

The asymptotic formula for stresses near the contact line at the large scale [11], which contains a term with logarithmic singularity in addition to a singular term, is used as a test when numerically solving the problem of the viscous-liquid flow. The calculation results for the parameter $C_0 = C_0(\alpha_0)$ in Eq. (9) for α_0 are shown in Fig. 1. Solid lines *a* and *b* correspond to calculations, and the dotted lines are plotted using the following formulas of analytical theory for small angles [2, 12]:

$$C_0 = 1 - \ln(2\alpha_0^2); \tag{12a}$$

$$C_0 = 2 - \ln(2\alpha_0^2), \tag{12b}$$

where Eq. (12a) corresponds to the explicit solution [2]. The dotted lines in Fig. 1 are close to the calculations in the region of small α_0 values. The plot $C_0(\alpha_0)$ along with asymptotic relation (2) provides the dependence $\alpha_0(\mathrm{Ca})$ of the dynamic contact angle on the velocity in the parametric form. The value $C_{0b}\left(\frac{\pi}{2}\right) = 1.64$ is in agreement with a similar constant $c_1 = 1.83$ [1] for finite contact angles. We emphasize the known agreement [1, 3] of theory [1] with experiments.

DYNAMICS OF THE DROP FOR FINITE CONTACT ANGLES

For the liquid drop that axisymmetrically flows on a flat surface, the surface of the drop at the large scale is close to the spherical segment with the radius $R_0(t)$ and the contact angle $\alpha_0(t)$, according to the quasi-equilibrium model with the parameters h_m and α_m [1, 2]. Let the subscript c refer to the spherical segment whose volume is equal to the drop volume V. The contact angle α_c is related to the radius x_0 of the drop base and equivalent radius $R_\mathrm{e} = \left(\frac{3V}{4\pi}\right)^{1/3}$, and the function Λ in Eq. (4) for the angle perturbation has the form

$$\Lambda_c(\theta_0, \theta) = \left(1 - 2\frac{h}{a_0}\right)\frac{\sin\theta}{\sin\theta_0}, \quad h = R_0(\cos\theta - \cos\theta_0). \tag{13}$$

The substitution of a_0 for h_k in Eq. (9) and matching of expansions (4) and (8) yields

$$C_{0b} = \int_0^{\theta_0} \{\sin\theta + \sin\theta_0 \Lambda_b(\theta_0, \theta) G(\theta)\} \frac{R_0}{h} d\theta; \tag{14}$$

$$C_{0c} = 2 + \int_0^{a_0} \left(2\frac{h}{a_0} - 1\right)\frac{G-1}{h} dh. \tag{15}$$

The normal stress P_n on S and dependences $C_0(\alpha_0)$ for various spheres (Fig. 2) are found from the numerical solution of the problem of the flow inside the liquid spherical segment. For small α_0 values, $C_{0b} \approx 1.64$ and $C_{0c} \approx 2$, as in agreement with the analytical theory [13–15]. The constant $C_{0c}\left(\frac{\pi}{2}\right) = 1.23$ is close to a similar constant [1] that is equal to unity. The contact angle parameter α_b makes it possible to take into account the small difference between the drop height $h(0)$ and the height a_0 of the spherical segment c.

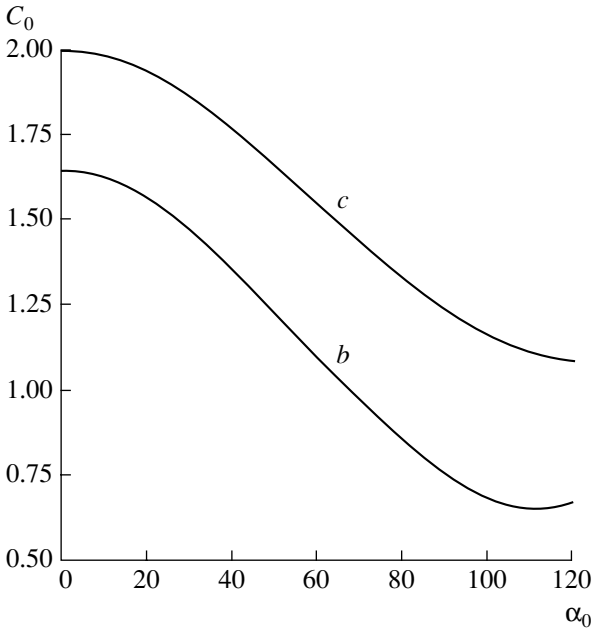

Fig. 2.

The equation for the contact angle of the drop follows from the relation $\dot{x}_0 = V$ for the spherical segment [1]:

$$\frac{d\alpha_0}{dt} = -\frac{V}{R_\mathrm{e}}\left[(2 + \cos\alpha_0)\sin\frac{\alpha_0}{2}\right]^{4/3}, \tag{16}$$

$$V = \frac{\sigma}{\mu}\left\{\ln\frac{h_0}{h_\mathrm{m}} - \ln\frac{\sin\alpha_0}{\sin\alpha_*}\right\}^{-1} \frac{1}{2}\int_{\alpha_\mathrm{m}}^{\alpha_0}\left(\frac{\alpha}{\sin\alpha} - \cos\alpha\right)d\alpha, \quad \alpha_0 = \alpha_c, \quad h = a_0\exp(-C_0(\alpha_0)), \tag{17}$$

where a_0 and x_0 are simple functions of α_0. The plot of $C_{0c}(\alpha_0)$ is given in Fig. 2. Complementing Eqs. (16) and (17) by expressions for the microparameters h_m and α_m (for one of the particular cases), we obtain a closed model for the dynamics of the drop on the wall. This model provides for a description of the flow in the drop with an accuracy of $O(\varepsilon^2)$. The parameters h_m and α_m, which are common for hydrodynamic problems at the large scale, are applicable to drops of arbitrary volume. The details of the boundary conditions of the problem are insignificant at large times.

The ordinary differential equation of the model is readily integrated analytically if the microangle α_m is independent of the velocity V ($\alpha_\mathrm{m} = \alpha_S$). Indeed, the expression that appears in braces in Eq. (17) and that includes the large parameter is a slow varying function of time. It should be treated as a constant in the leading approximation and its slow variation should be taken into account in the resulting formula. The correction is found by the iteration method. Using such a method, from Eqs. (16) and (17) for small α_0 values and com-

plete wetting, we obtain the approximate solution, $\alpha_0 \sim t^{-3/10}$ and $x_0 \sim t^{1/10}$, which is valid [1, 2] for various expressions for the microscale h_m (including that for the precursor-film flow). This validity has been corroborated by many experiments, some of which were presented by De Gennes in review [4].

In conclusion, we emphasize that, for Reynolds numbers near unity, wetting theory based on Stokes equations is applicable with an accuracy of $O(\varepsilon)$.

ACKNOWLEDGMENTS

This work was supported by the Council of the President of the Russian Federation for Support of Young Russian Scientists and Leading Scientific Schools (project no. NSh-2059.2003.1).

REFERENCES

1. O. V. Voinov, Izv. Akad. Nauk SSSR, Mekh. Zhidk. Gaza, No. 5, 76 (1976).
2. O. V. Voinov, Prikl. Mekh. Tekh. Fiz., No. 2, 92 (1977).
3. O. V. Voinov, Dokl. Akad. Nauk SSSR **243** (6), 1422 (1978).
4. P. G. De Gennes, Rev. Mod. Phys. **57**, 827 (1985).
5. R. Ablett, Philos. Mag. **46**, 6 (1923).
6. J. Fukai, Y. Shiba, Y. Yamamoto, *et al.*, Phys. Fluids **7** (2), 236 (1995).
7. M. Pasandideh-Fard, Y. M. Chao, S. Chandra, and J. Mostaghimi, Phys. Fluids **8** (3), 650 (1996).
8. A. Siebold, M. Nardin, J. Schultz, *et al.*, Colloid Surf. A **161**, 81 (2000).
9. O. V. Voinov and V. V. Voinov, Dokl. Akad. Nauk SSSR **221** (3), 559 (1975) [Sov. Phys. Dokl. **20**, 179 (1975)].
10. O. V. Voinov, Prikl. Mekh. Tekh. Fiz., No. 3, 94 (1979).
11. O. V. Voinov, Dokl. Akad. Nauk **394** (2), 473 (2004) [Dokl. Phys. **49**, 95 (2004)].
12. O. V. Voinov, Int. J. Multiphase Flow **21**, 801 (1995).
13. O. V. Voinov, Available from VINITI, No. 2114-V94 (1994).

Translated by R. Tyapaev

Doklady Physics, Vol. 50, No. 7, 2005, pp. 385–387. Translated from Doklady Akademii Nauk, Vol. 403, No. 2, 2005, pp. 198–200.

MECHANICS

Simulation of the Creep of Materials with Different Strengths

V. M. Yarushina

Presented by Academician N.F. Morozov January 13, 2005

Received February 10, 2005

It is well known that certain materials, such as cast iron, titanium and aluminum–magnesium alloys, beryllium copper, carbon plastic, granite, sandstone, coal, etc., behave in different ways under compressive and tensile loads [1–3]. This difference is due to various internal microprocesses, such as the generation and growth of microcracks and microvoids, disclination distribution, sliding of grain boundaries, etc. This phenomenon is observed in both reversible [4–6] and irreversible [7–10] deformation processes and affects the entire spectrum of the mechanical and physical properties of materials. In this study, a creep model for materials with different moduli is constructed using piecewise-linear deformation potentials, and a technique for determining the material constants responsible for its mechanical properties is discussed.

The creep model with piecewise-linear potentials for materials with different moduli is constructed on the basis of the assumption that, in the initial creep stage, the total strains of a material remain small, and the stresses are moderate and do not lead to plastic flow. Therefore, the total strain tensor e_{ij} is the sum of the elastic strain tensor e_{ij}^e and the creep strain tensor e_{ij}^v:

$$e_{ij} = e_{ij}^e + e_{ij}^v. \tag{1}$$

We assume that the elastic strains of the medium and the creep strain rates are determined solely in terms of the stresses σ_{ij} in the medium through the potential dependences

$$e_{ij}^e = \frac{\partial U(\sigma_{ij})}{\partial \sigma_{ij}}, \quad \dot{e}_{ij}^v = \frac{\partial V(\sigma_{ij})}{\partial \sigma_{ij}},$$
$$U(\sigma_{ij}) = U_1(\sigma) + U_2(\Sigma), \quad V(\sigma_{ij}) = V(\Sigma), \tag{2}$$

where σ and Σ are certain invariants of the stress tensor. We choose the mean stress $\sigma = \frac{\sigma_{kk}}{3}$ as the first invariant in Eq. (2) and specify the second invariant in the form of a linear homogeneous function of the principal stresses σ_i

$$\Sigma = \begin{cases} \max(S_i - \beta S_j) + q_1\sigma & \text{for } \sigma > 0, \\ \max(S_i - \beta S_j) - q_2\sigma & \text{for } \sigma < 0, \end{cases} \tag{3}$$

where $S_i = \sigma_i - \sigma$ are the principal values of the stress deviator. For $\beta = 1$ and $q_1 = q_2 = 0$, expression (3) is the Tresca flow function $\Sigma = \max(S_i - S_j)$, which is widely used in plasticity theory as a yield criterion for media having the same properties under tension and compression. The same function was used in [11, 12] for constructing a creep model for normally isotropic materials. In the general case, $0.5 \le \beta \le 2$ and $q_i > 0$. Here, the parameter β is directly responsible for the existence of different moduli of the medium, while the parameters q_1 and q_2 are responsible for its capacity for compaction and thinning, respectively. The isovalue surfaces of Eq. (3) represent two hexahedral pyramids whose bases meet in the deviator plane (Fig. 1a). The cone vertices lie on the hydrostatic axis at the points $\sigma = \frac{\Sigma}{q_1}$ and $\sigma = -\frac{\Sigma}{q_2}$. The cones vary with time and from one point of the material space to another, and their vertices slide along the hydrostatic axis. The vertex angle depends only on the mechanical properties of the medium and remains unchanged. Figure 1b shows the sections of surface (3) by the deviator plane $\sigma = 0$ for different values of β. Here, the outer and inner triangles are associated with $\beta = 0.5$ and 2, respectively, and the hexagon corresponds to any intermediate value $0.5 < \beta < 2$.

Under the assumption that the material exhibits linear elastic properties and obeys a power law of creep throughout the entire space of principal stresses, except

Institute of Automation and Control Processes, Far East Division, Russian Academy of Sciences, ul. Radio 5, Vladivostok, 690041 Russia
e-mail: v.yarushina@mail.ru

1028-3358/05/5007-0385$26.00

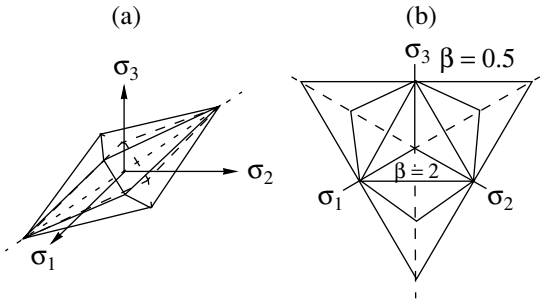

Fig. 1. (a) Surfaces Σ = const for materials with different moduli and (b) their sections by the deviator plane.

for the vicinity of zero, the potentials can be taken in the form

$$U_1(\sigma) = \frac{a}{2}\sigma^2, \quad U_2(\Sigma) = \frac{b}{2}\Sigma^2,$$
$$V(\Sigma) = \frac{B}{n+1}\Sigma^{n+1}. \tag{4}$$

Since function (3) is piecewise smooth and relations (2) imply its differentiation, we assume, according to [11, 12], the following relation at the points of loss of smoothness:

$$\frac{\partial\Sigma}{\partial\sigma_i} = \alpha\frac{\partial\Sigma^{(1)}}{\partial\sigma_i} + (1-\alpha)\frac{\partial\Sigma^{(2)}}{\partial\sigma_i}, \quad 0 \le \alpha \le 1, \tag{5}$$

where $\Sigma^{(1)}$ = const and $\Sigma^{(2)}$ = const are edge-forming surfaces, and α is the new unknown function determining the direction of the normal vector at the corner point. The system of equations at the edge of the piecewise-linear surface Σ = const includes, along with α, the equality

$$\Sigma^{(1)} = \Sigma^{(2)}, \tag{6}$$

which relates the static unknowns. In most cases, this equality makes it possible to considerably simplify the process of solving boundary value problems. The system of Eqs. (1)–(6) is closed when it is complemented with the equilibrium equations, the strain compatibility equations, and the relations between the stress tensor and its principal values.

It should be noted that, on the one hand, the creep model thus constructed is so simple that new analytical solutions of non-one-dimensional boundary value problems on the creep and strain relaxation in normally isotropic materials were derived within the framework of the model [11, 12]. Moreover, the idea of this construction is to obtain creep relations that are consistent with the foundations of ideal plastic flow theory [13], so that the well-developed mathematical apparatus of that theory can be applied to the creep problem. On the other hand, the model presented above possesses a very broad potential for describing certain features of the creep process for various materials whose mechanical properties are described by three potential functions, $U_1(\sigma)$, $U_2(\Sigma)$, and $V(\Sigma)$, and the form of the equivalent stress Σ.

In order to complete the description of the proposed model of a medium with different moduli, it is necessary to indicate the manner in which the material constants β, q_1, q_2, a, b, B, and n can be determined using experimental data. Uniaxial tensile–compression tests may be regarded as baseline experiments.

In uniaxial tensile tests, the load is applied to a sample in such a way that $\sigma_1 = \sigma_+$ = const and $\sigma_2 = \sigma_3 = 0$. The stresses correspond to the edge $\Sigma^{(1)} = \Sigma^{(2)}$, where $\Sigma^{(1)} = S_1 - \beta S_2 + q_1\sigma$ and $\Sigma^{(2)} = S_1 - \beta S_3 + q_1\sigma$. From the model relations, it follows that

$$e^e_{1+} = (a + b(2 + \beta + q_1)^2)\frac{\sigma_+}{9},$$
$$\dot{e}^v_{1+} = B(2 + \beta + q_1)^{n+1}\frac{\sigma_+^n}{3^{n+1}},$$
$$e^e_{2+} = e^e_{3+} = \left(a + (2 + \beta + q_1)(2q_1 - 2 - \beta)\frac{b}{2}\right)\frac{\sigma_+}{9},$$
$$\dot{e}^v_{2+} = \dot{e}^v_{3+} = \frac{B}{2}(2 + \beta + q_1)^n(2q_1 - 2 - \beta)\frac{\sigma_+^n}{3^{n+1}}.$$

Uniaxial compression is realized at $\sigma_1 = \sigma_-$ = const and $\sigma_2 = \sigma_3 = 0$ and corresponds to the edge $\Sigma^{(1)} = \Sigma^{(2)}$, where $\Sigma^{(1)} = S_2 - \beta S_1 - q_2\sigma$ and $\Sigma^{(2)} = S_3 - \beta S_1 - q_2\sigma$. From the model relations, it follows that

$$e^e_{1-} = (a + b(1 + 2\beta + q_2)^2)\frac{\sigma_-}{9},$$
$$\dot{e}^v_{1-} = -B(1 + 2\beta + q_2)^{n+1}\frac{|\sigma_-|^n}{3^{n+1}},$$
$$e^e_{2-} = e^e_{3-} = \left((1 + 2\beta + q_2)(1 + 2\beta - 2q_2)\frac{b}{2} - a\right)\frac{|\sigma_-|}{9},$$
$$\dot{e}^v_{2-} = \dot{e}^v_{3-} = \frac{B}{2}(1 + 2\beta + q_2)^n(1 + 2\beta - 2q_2)\frac{|\sigma_-|^n}{3^{n+1}}.$$

By plotting the stresses and the strain rates $\dot{e}_1$ and $\dot{e}_2$ in the logarithmic scale, we determine the creep

exponent n and the quantities

$$B\frac{(2+\beta+q_1)^{n+1}}{3^{n+1}} = \xi_+^{n+1},$$

$$B\frac{(2+\beta+q_1)^n}{3^n}\frac{2q_1-2-\beta}{6} = \eta_+,$$

$$B\frac{(1+2\beta+q_2)^{n+1}}{3^{n+1}} = \xi_-^{n+1},$$

$$B\frac{(1+2\beta+q_2)^n}{3^n}\frac{1+2\beta-2q_2}{6} = \eta_-,$$

whence it follows that

$$\beta = \frac{2\xi_+^n(\xi_-^{n+1}+\eta_-)-\xi_-^n(\xi_+^{n+1}-\eta_+)}{2\xi_-^n(\xi_+^{n+1}-\eta_+)-\xi_+^n(\xi_-^{n+1}+\eta_-)},$$

$$B = \left(\frac{2}{3}\right)^{n+1}\left(\frac{2(\xi_+^{n+1}-\eta_+)}{\xi_+^n}-\frac{\xi_-^{n+1}+\eta_-}{\xi_-^n}\right)^{n+1},$$

$$q_1 = 3\xi_+B^{-1/(n+1)}-2-\beta,$$

$$q_2 = 3\xi_-B^{-1/(n+1)}-1-2\beta,$$

$$b = \frac{B^{2/(n+1)}}{\xi_+^2-\xi_-^2}\left(\frac{e_{1+}^e}{\sigma_+}-\frac{e_{1-}^e}{\sigma_-}\right),$$

$$a = 9\frac{e_{1-}^e}{\sigma_-}\frac{\xi_+^2}{\xi_+^2-\xi_-^2}-9\frac{e_{1+}^e}{\sigma_+}\frac{\xi_-^2}{\xi_+^2-\xi_-^2},$$

where e_{1+}^e and e_{1-}^e are the measured values of the instantaneous strain arising immediately after the load has been applied. Thus, two tensile–compression experiments are sufficient to determine the relevant parameters of the model.

REFERENCES

1. Yu. N. Rabotnov, *Creep of Structural Elements* (Nauka, Moscow, 1966) [in Russian].
2. A. F. Nikitenko, *Creep and Long-Term Strength of Metals* (Novosibirskiĭ Gos. Arkhit. Stroit. Univ., Novosibirsk, 1997) [in Russian].
3. L. S. Burshteĭn, *Static and Dynamic Tests of Rocks* (Nedra, Moscow, 1970) [in Russian].
4. S. A. Ambartsumyan, *Multimodulus Theory of Elasticity* (Nauka, Moscow, 1982) [in Russian].
5. V. P. Myasnikov and A. I. Oleĭnikov, Dokl. Akad. Nauk SSSR **322** (1), 57 (1992) [Sov. Phys. Dokl. **37** (1), 41 (1992)].
6. V. S. Nikishin and G. S. Shapiro, *Problems of the Theory of Elasticity for Multilayered Medium* (Nauka, Moscow, 1973) [in Russian].
7. B. V. Gorev, V. V. Rubanov, and O. V. Sosnin, Probl. Prochn., No. 7, 62 (1979).
8. G. I. Bykovtsev and T. B. Lavrova, Izv. Akad. Nauk SSSR, Mekh. Tverd. Tela, No. 2, 146 (1989).
9. G. Z. Voyiadjis and A. A. Zolochevsky, Int. J. Solids Struct. **37**, 3281 (2000).
10. I. Yu. Tsvelodub, Izv. Akad. Nauk SSSR, Mekh. Tverd. Tela, No. 2, 70 (1982).
11. G. I. Bykovtsev and V. M. Yarushina, *Problems of the Mechanics of Continua and Structural Elements* (Dal'nauka, Vladivostok, 1998) [in Russian].
12. A. A. Burenin and V. M. Yarushina, Dal'nevost. Mat. Zh. **3** (1), 64 (2002).
13. G. I. Bykovtsev and D. D. Ivlev, *Theory of Plasticity* (Dal'nauka, Vladivostok, 1998) [in Russian].

Translated by M. Lebedev